Development of Multistate Density Functional Theory for Photochemistry and Vibrational Dynamics using Quantum Vibration Perturbation Theory

A Dissertation
SUBMITTED TO THE FACULTY OF
UNIVERSITY OF MINNESOTA
BY

Adam Grofe

IN PARTIAL FULFILLMENT OF THE REQUIREMENTS
FOR THE DEGREE OF
DOCTOR OF PHILOSOPHY

Prof. Jiali Gao, Advisor

January, 2018

Acknowledgements

If you understand the way broadly, you will see it all things
-Miyamoto Mushashi, the Book of Five Rings

I would like to begin by thanking the two people who have started me off on research, Alessandro Cembran and Pilailuk Kabbalee, who provided me the first Charmm scripts from which to learn from. I also wish to express my gratitude to all of the Gao group members with whom I have had many meaningful discussion with: Michael Mazack, Yingjie Wang, Haisheng Ren, Pavel Rehak, Carlos Ramirez-Mondragon and Katie Youmans. I would also like to thank all of the visiting professors from China Quan Luo, Jilong Zhang, Yongshan Zhao and Yanliang Ren. And all of the wonderful students at Jilin University who were very patient with me on my first foray into international travel, especially Meiyi Liu, Jingting, Xinwei Guo, Shaoyuan Zhou, and Haifeng. I would like to thank my fellow collaborators Zexing Qu, Hui Li, Aaron Massari, Ruijie Xue, Yin He, Chen Xin, Ivan C. Spector and Courtney M. Olson for many fascinating and meaningful discussions. Most of all, I would like to thank my advisor, Jiali Gao, for being very patient and understanding with me during my growth as a young scientist, and from whom I have learned more from than I can possibly recall.

Dedication

To my family, who have supported me greatly on my journey to pursue science

Abstract

This dissertation is contains two separates areas of research. The first three Chapters focus on the development and several proof-of-concepts for multistate density functional theory (MSDFT) regarding excited state chemistry. When performing configuration interaction (CI) on density functional theory (DFT), there is a danger of double-counting with regard to correlation. It is shown that it is possible to remove double counting in a systematic way by combining wave function theory with DFT, and that MSDFT has the correct topology with regard to conical intersection because it fundamentally includes coupling between the excited state densities and the ground state density, which is not true for time-dependent DFT. This was revealed for the dissociation of ammonia, and Jahn-Teller conical intersections. Block localized DFT was used to assemble diabatic states that can be optimized separately and permits the use of chemical intuition by defining the states in a relatively straightforward manner. Finally, the MSDFT formalism was used to optimize spin-multiplet states with the correct degeneracy, which can be difficult in DFT due to the nonlinearity of the current exchange-correlation functionals.

The second section of this dissertation regard vibrational dynamics. There is a multitude of methods for computing the vibrational frequency, but very few that simultaneously model anharmonicity and nuclear quantum effects in a manner that is efficient enough for computing frequency trajectories. Quantum vibration perturbation

(QVP) theory satisfies all three of these criteria. This is accomplished by utilizing two approximations: (1) A discrete variable representation of the nuclear wave function is used that only requires single point energy calculations to optimize the wave function, (2) Perturbation theory is used to update the wave function across a set of configurations, which circumvents the need to solve the Schrödinger equation. The first application of this model is on hydrochloric acid in minimal solvation shells (water), and acetone bulk solvation dynamics. An implementation strategy is presented that allows for a reference normal mode to be applied across a trajectory. Then QVP is used to probe the condensed phase solvation dynamics of a carbonyl stretch and two silane stretches.

Table of Contents

Acknowledgements ..... **i**

Dedication ..... **ii**

Abstract ..... **iii**

Table of Contents ..... **v**

List of Tables ..... **viii**

List of Figures ..... **xi**

List of Acronyms/Initialisms ..... **xvi**

Electronic Structure Theory xvi
Simulation and Spectroscopy xix
Molecules xix

Chapter 1. Beyond Kohn-Sham Approximation: Hybrid Multistate Wave Function and Density Functional Theory **1**

1.1. Introduction 1
1.2. The Dynamic-Then-Static Ansatz 3
1.3. Multistate Density Functional Theory 5
1.4. Results and Discussion 12
1.5. Conclusions 18

Chapter 2. Diabatic-At-Construction (DAC) Method for Diabatic and Adiabatic Ground and Excited States Based on Multistate Density Functional Theory **20**

2.1. Introduction 20
2.1.1. Adiabatic-To-Diabatic via similarity transformation: 22
2.1.2. Diabatic-At-Construction by experimental validation 23
2.2. Methods 25
2.2.1. Step 1(a): Block-localized Kohn-Sham Density Functional Theory 27
2.2.2. Step 1(b): Construction of CSFs. 27

2.2.3. Step 1(c): Configuration interaction. 29
2.2.4. Step 2: Multistate Density Functional Theory: 31
2.3. Computational Details 34
2.4. Results and Discussion 36
2.4.1. Adiabatic Potential Energy Surfaces 38
2.4.2. Valence-Bond Diabatic States 42
2.4.3. Orthogonal Diabatic States 44
2.4.4. Diabatic Coupling 49
2.5. Conclusions 51

Chapter 3. Spin-Multiplet Components and Energy Splittings by Multistate Density Functional Theory 54

3.1. Introduction 54
3.2. Multistate Density Functional Theory 56
3.3. Transition Density Functional Design for Spin Components 60
3.4. Results and Discussion 66
3.5. Conclusions 76

Chapter 4. Perturbation Approach for Computing Infrared Spectra of the Local Mode of Probe Molecules 78

4.1. Introduction 78
4.2. Methods 82
4.3. Computational Details 87
4.4. Results and Discussion 89
4.4.1. HCl-Water Clusters 89
4.4.2. Acetone in Aqueous Solution 98
4.5. Conclusions 100

Chapter 5. Implementation of Quantum Vibration Perturbation Theory: Application to Acetophenone Solvatochromic Shifts and Hydrogen Bond Exchange Dynamics of Acetophenone in Methanol and Other Solvents 104

5.1. Introduction 104
5.2. Theoretical Methods 108
5.2.1 QVP Implementation 109
5.2.2 Transformation Matrix for the Normal Mode 114
5.3 Computational Details 122
5.3.1. QM/MM potential for the carbonyl stretch vibration and hydrogen bonding interactions of acetophenone 122

5.3.2. Carbonyl Stretch Vibrational Frequency and Electric Field Calculations.... 127
5.4 Experimental Details..... 129
5.5. Results and Discussion 132
5.6. Concluding Remarks..... 140

Chapter 6. Enhanced Vibrational Solvatochromism and Spectral Diffusion by Electron Rich Substituents on Small Molecule Silanes 142

6.1. Introduction..... 142
6.2. Experimental Methods..... 144
6.3. Results and Discussion 148
6.4. Conclusions..... 165

Bibliography 167

List of Tables

Table 2.1. Bond energies (D_e) and adiabatic excitation energies (T_e) in eV, and geometries in Å for the ground (*X*) and the first three excited states (denoted as *A*, *C*, and *D*) of LiH. The aug-cc-pVTZ basis set is used in all calculations using the multistate density functional theory (MSDFT) and complete-active-space second-order perturbation theory (MS-CASPT2). The PBE0 density functional is used in MSDFT; the (2,9) active space is employed for MS-CASPT2. 41

Table 3.1. Experimental and computed atomic excitation energies (eV) of beryllium, boron, carbon, nitrogen, and oxygen using multistate density functional theory (MSDFT) and mixed molecular orbital-valence bond theory (MOVB). The pure spin state is indicated by $|S, M_S>$. The hybrid functional PBE0 and PBEC with 25% and 100% Hartree-Fock exchange as well as M06-HF, also containing 100% Hartree-Fock exchange are used. The aug-cc-pVQZ basis is used in all computations. MUD: mean unsigned deviations from experiment. 68

Table 3.2. Computed adiabatic excitation energies (eV) of CH_2, NH_2^+, SiH_2, and PH_2^+ molecules. Spin-flip (SF) results are taken from reference 137 for comparison. The PBE0 exchange-correlation functional is used both in SF and in multistate (MS) DFT, and the aug-cc-pVQZ basis set is used in all calculations.[a] 72

Table 3.3. Computed singlet-triplet energy gaps (eV) for α-2, α-3, and α-2-didehydrotoluene (DHT) using multistate density functional theory (MSDFT) and mixed molecular orbital and valence bond (MOVB) method along with results from spin flip (SF) approaches. PBE0 is used in DFT methods and cc-pVTZ basis is used in all calculations.[a] 75

Table 4.1. Computed HCl stretching vibrational frequency ω_{Cl-H} and the shift $\Delta\omega_{Cl-H}$ of the $HCl(H_2O)$ complex using harmonic normal mode analysis (NMA), Fourier transform of the dipole autocorrelation function (DAF) and the spectral expansion (equation 4.3.3) of the frequency-frequency time correlation function from the QVP1 method, along with the experimental value. Vibrational frequencies are given in cm^{-1}... 94

Table 4.2. Computed H-Cl stretching vibrational frequencies (cm^{-1}) for (HCl)2(H2O) by solving two independent one-dimensional (E_{1D}) Schrodinger equation and a two-dimensional (E_{2D}) vibrational Schrodinger equation. The potential energy surfaces were determined using M06-2X/cc-pVTZ. Q_1 and Q_2 represent, respectively, the H-Cl stretch

associated with the HCl molecule directly hydrogen-bonded to water and hydrogen-bonded to the probe HCl molecule (Figure 4.4). 96

Table 5.1. First and second transition energies calculated using different number of basis functions and grid spacing values using the discrete variable representation (DVR) approach described by Colbert-Miller, and the potential optimized DVR (PO-DVR) method for the same configuration of acetophenone in water. For convenience, bold texts are used to highlight digits that match the exact values (from the largest grid calculations). 111

Table 5.2. Fitted parameters for equation 5.3.1 125

Table 5.3. Fitted parameters for equation 5.3.3 127

Table 5.4. Computed peak positions from PM3/OPLS-AA simulations, and solvatochromic shifts of acetophenone in various solvents, compared to experimentally measured solvatochromic shifts. Hexane was used as the reference for all of the solvatochromic shifts. 133

Table 5.5. Isotropic polarizability computed using the Lorentz-Lorenz equation $\left(\alpha = \frac{3}{4\pi N}\left(\frac{n^2-1}{n^2+2}\right)\right)$, where n is the refractive index and N is the number density of the solvent. The values used in the equation were taken from reference 313. The polarity of each is given using the normalized ET(30) scale.[307] 134

Table 6.1. Normal mode vibrational frequencies for the Si-H stretch (cm^{-1}) of trimethoxysilane (TriMOS) and triphenylsilane (TriPS) in the gas phase and in pentane, chloroform and isopropanol solution using M06-2X/6-31+G(d,p) with the Minnesota solvation model (SMD), and the polarizable continuum model (PCM). And gas phase CHELP partial atomic charges (a.u.) 150

Table 6.2. Computed Si-H stretch vibrational frequencies (cm-1) and full width at half max (FWHM) peak widths (cm^{-1}) of trimethoxysilane (TriMOS) and triphenylsilane (TriPS) in the gas phase and in pentane, chloroform and isopropanol solution using quantum vibrational perturbation theory in combined QM/MM molecular dynamics simulations. The solute is treated by the AM1 Hamiltonian and the solvents are represented by the CHARMM force field. The experimental data are also listed for convenience of comparison..... 156

Table 6.3. FFCF parameters for TriPS and TriMOS in isopropanol, chloroform, and pentane. 160

Table 6.4. Computed FFCF parameters for TriPS and TriMOS in the three solvents… 162

Table 6.5. Hydrogen bond lifetimes (τ_{HB}) in isopropanol simulations. 163

Table 6.6. Fitted parameters to the computed molecular dipole autocorrelation functions for TriMOS and TriPS in chloroform and isopropanol solutions. 165

List of Figures

Figure 1.1. Computed potential energy surfaces for the ground and the first excited state for cyclopropenyl radical (a) and benzene cation radical (b) along the gradient difference (g) and derivative coupling (h) vector directions (see text). 13

Scheme 1.1. Schematic representation of the valence bond configurations used in MSDFT for benzene cation radical. Deformation from the D_{6h} Jahn-Teller geometry in the center along the gradient difference vector (red) leads to the quinoid configuration on the right, and the antiquinoid structure on the left. There are three equivalent pairs forming the moat around the conical intersection. 15

Figure 1.2. Potential energy curves of the ground and nσ* excited states of planar NH3 along a stretched N-H bond at the C_{2v} symmetry using MSDFT and mixed molecular orbital and valence bond (MOVB) calculations. The two horizontal bars are the MSDFT and MOVB (WFT without dynamic correlation) energies at the optimized geometry of ammonia at the C_{3v} symmetry. The insert depicts the double cone topology of the potential energy surfaces in the branching space as the dissociating hydrogen moving away from the planar geometry and the improper dihedral angle moves away from planarity. The PBE0 density functional and aug-cc-pVTZ basis set are used in MSDFT calculations. 18

Figure 2.1. Adiabatic potential energy curves for the four lowest $^1\Sigma^+$ states of LiH as functions of interatomic distance from MSDFT (dashed curves) using the PBE0 density functional and from MS-CASPT2//SA(4)-CASSCF(2,9) calculations (solid curves). The aug-cc-pVTZ basis set with the diffuse *s*-function replaced by that of the Dunning-Hay basis (simply denoted by aug-cc-pVTZ throughout) is used in all MSDFT computations, whereas the standard aug-cc-pVTZ basis is used in wave function methods. 37

Figure 2.2. Adiabatic potential energy curves for the four lowest $^3\Sigma^+$ triplet states of LiH (**a**, **c**, **d**, and **e** in order of increasing energy) as functions of interatomic distance from MSDFT (solid curves) using the PBE0 density functional, and from MS-CASPT2/SA(4)-CASSCF (dashed curves). The aug-cc-pVTZ basis set is used in all computations (see caption of Figure 2.1). 38

Figure 2.3. (**a**) Valence-bond diabatic (solid curves) and adiabatic (dashed curves) potential energy curves of LiH as a function of interatomic separation optimized by multistate density functional theory (MSDFT). The PBE0 density functional along with the aug-cc-pVTZ basis set (see Figure 2.1) are used in all calculations. (**b**) Diabatic

potential energy curves obtained by the Three-Fold-Way diabatization approach. Adapted from Figure 2.5 of reference 75 with permission by the American Institute of Physics. 44

Figure 2.4. Orthogonalized diabatic (dashed curves) potential energy curves of LiH as a function of interatomic separation, transformed from the non-orthogonal VB-diabatic states in Figure 2.3(a) by (**a**) direct Gram-Schmidt (GS) orthogonalization, (**b**) GS-projection of mixed of 2*s* and 2*p* covalent states, (**c**) 2*s*-2*p* mixing scaled by the overlap integral, and (**d**) as in (c) along with a small amount of 25% 2*s* state added to the ionic state. The adiabatic potential energy curves are shown as solid curves. 48

Figure 2.5. Squared diabatic couplings between selected pairs of orthogonal diabatic states of LiH shown in Figure 2.4(d) as a function of interatomic separation. All results are determined by MSDFT with the aug-cc-pVTZ basis set (see Figure 2.1). 50

Figure 2.6. Compued derivative coupling values, $< \Psi_I(\mathbf{r};\mathbf{R}) | \nabla_R | \Psi_J(\mathbf{r};\mathbf{R}) >$ for various states indicated as a function of interatomic separation. All results are determined by MSDFT with the aug-cc-pVTZ basis set (see Figure 2.1). 51

Figure 3.1. Interaction diagram illustrating electronic coupling among the three determinant configurations for the excited $2s^1 2p^2$ configuration of boron atom. 65

Figure 3.2. Computed adiabatic and vertical excitation energies of CH_2 at the four adiabatic geometries. The PBE0 exchange-correlation functional is used in multistate density functional theory along with the aug-cc-pVQZ basis set. Geometries were optimized using FCI/TZ2P from reference 47. 73

Scheme 3.1. Structures of α-2, α-3, and α-4-didehydrotoluene (DHT). 74

Figure 4.1. Computed vibrational wave functions of the ground, and the first and second excited states of the HCl stretch mode in the optimized HCl(H_2O) structure. Discrete variable representation (DVR) at the eight optimized grid points are indicated. 83

Figure 4.2. Correlation of the exact and the QVP vibrational frequencies for HCl in 40 complex structures from an ab initio molecular dynamics trajectory of the H_2O…HCl cluster using CCSD(T)-F12b/cc-pVTZ-F12. The exact results are obtained by solving the vibrational Schrödinger equation (abscissa) for each complex structure, whereas up to the fourth-order perturbation is used in the quantum vibrational perturbation (QVP) approach (ordinate). The black dashed line represents a perfect match. 87

Figure 4.3. Normalized IR line shapes from experiment (black) and computations for the HCl stretching vibrational mode in the HCl(H_2O) complex. (a) The spectrum obtained by Fourier transform of DAF (equation 4.3.1) is given in blue, and that from instantaneous QVP1 frequencies (equation 4.3.2) is displayed in green, both at the M06-2X/cc-pVTZ level. (b) Spectral line shapes determined by the second-cumulant expression based on the frequency-frequency time correlation function (equation 4.3.3) are shown at the CCSD(T)-F12b (red) and M06-2X (green) levels along with the composite of CCSD(T)-F12b frequency for the reference state and M06-2X frequency shifts (blue). The distribution of computed H-Cl stretching frequency (blue) at the CCSD(T)-F12b level is illustrated in (c) along with the corresponding spectral line shape function (red) and the experimental spectrum (black). 93

Figure 4.4. The 2D pump-probe spectra of the HCl stretching vibration in the HCl(H_2O) complex are given at the evolution time t_2 equaling to 0 fs, 302 fs, 504 fs and 705 fs respectively. See text for specific details. 95

Figure 4.5. The experimental spectra and the overall computed HCl stretching vibrational spectra for a mixture of (HCl)(H_2O), $(HCl)_2(H_2O)$ and (HCl)$(H_2O)_2$ clusters with weighting factors of 1, 0.41 and 0.46 for the relative intensities based on the experimental intensities. The blue and red arrows specify the HCl stretching mode in the $(HCl)_2(H_2O)$, (HCl)$(H_2O)_2$ clusters, respectively, and the strongest peaks correspond to that in the HCl(H_2O) complex. The latter was sampled by M06-2X/cc-pVTZ, whereas the remaining systems were sampled using BLYP-D Born-Oppenheimer molecular dynamics simulations. 97

Figure 4.6. Experimental (black) and computed vibrational spectra of the carbonyl stretching region of acetone in water. The spectrum from the first-order quantum vibration perturbation (QVP1) calculation employing a composite of the CCSD(T) reference frequency and a QM(AM1)/MM perturbation potential is shown in red, and that from the Fourier transform of the molecular dipole autocorrelation function determined using AM1 directly in QM/MM simulations is given in blue. 100

Figure 5.1. Two sets of three coplanar position vectors in the C2v point group. The index of each vector is given at the tip of each vector. The only difference between the two sets is reflection through the mirror plane. 117

Figure 5.2. Frequency trajectories computed using the Arun et al. algorithm for the rotation matrix and the normal mode displacement (NMD) weighted algorithm presented in equation 5.2.11. 119

Figure 5.3. (a) and (b). Computed vibrational frequencies using second order quantum vibrational perturbation (QVP2) method against the exact results calculated with 50 discrete points at a grid interval of 0.01 Å (Reference) with (a) and without (b) alignment of the potential energy minimum along the mode coordinate. **(c) and (d)** show the potential energies along the mode coordinate for one randomly selected structure without (c) and with (c) the minimum matched against the reference state. The shaded region represents the magnitude of the perturbation operator in QVP. 121

Figure 5.4. a). Potential energy scans of the normal mode of the carbonyl stretch of acetophenone at the level of MP2/aug-cc-pVDZ, PM3, and the difference between both levels of theory and result of fitting equation 5.3.1. **b).** The error of the fit as a function of the normal mode. 125

Figure 5.5. Computed interaction energies between acetophenone and methanol as a function of the distance between donor and acceptor oxygen atoms using the MP2/aug-cc-pVDZ (purple), the standard PM3/OPLS potential, the PM3+ΔU model for the QM part, and the final PM3v/OPLS model..... 127

Figure 5.6. a). Calculated infrared spectra of the carbonyl stretch vibration of acetophenone in n-hexane, tetrachloromethane, diethyl ether, N,N-dimethylacetamide, trichloromethane, acetonitrile, methanol, and water. **(b).** Correlation between the computed carbonyl vibrational frequency and the electric field on the carbonyl group. . All results were obtained from molecular dynamics simulations employing the combined PM3/OPLS-AA potential. The PM3 frequencies have been shifted by 240 cm-1 to match the experimental value in the gas phase. A linear regression fit in (b) resulted in 133

Figure 5.7. Simulated and experimental FTIR spectra for acetophenone in methanol. The vertical lines are the ensemble averaged frequencies for the 0 and 1 hydrogen bonding states, and heights of the lines indicate the relative proportion in the trajectory. The full simulated line was from the trajectory with a temperature of 298 K, and the dashes lines were from a simulation at 250 K. 137

Figure 5.8. 2DIR of acetophenone carbonyl stretch in methanol. The first column is the experimental 2DIR (at 298 K) and the second and third columns are from the simulations at 298 K and 250 K respectively. The rows are for waiting times of 0.2 and 3.0 ps..... 139

Figure 6.1. a). Solvent subtracted, baselined, and normalized FTIR spectra of the Si-H vibration for TriPS (left) and TriMOS (right) in isopropanol (black), chloroform (red), pentane (blue), and gas phase (orange). This coloring convention is used throughout. **b).** Computed linear spectra in the Si-H stretch vibrational frequency region for TriPS (left) and TriMOS (right). 151

Figure 6.2. Radial distribution functions (TriMOS:purple, TriPS:blue) and integrated radial distribution function computed from the AM1/CHARMM MD simulations. (TriMOS:green, TriPS:yellow). **a).** Between silane hydrogen and chlorine atoms of chloroform. **b).** Between the hydrogen bond acceptor in TriMOS and the hydrogen donor in isopropanol. **c).** Between silane hydrogen and the central carbon of isopropanol. ... 154

Figure 6.3. 2D-IR spectra collected at T_w = 0.3 (left column) and 3 ps (right column) for the $\nu_{Si\text{-}H}$ mode on TriMOS in isopropanol (a,c) and pentane (b,d). 157

Figure 6.4. CLS decays as a function of T_w for TriMOS (solid markers) and TriPS (open markers) in isopropanol (black), chloroform (red), and pentane (blue). Overlaid are solid curves (TriMOS) and dotted curves (TriPS) to show multiexponential fits to the data described in the text. The markers are the average CLS values and the error bars are the standard deviations..... 159

Figure 6.5. Normalized dipole autocorrelation function (DAF) for individual solvent molecules in isopropanol (black), chloroform (red), and pentane (blue). 164

List of Acronyms/Initialisms

Electronic Structure Theory

AM1	Austin Model 1
ATD	Adiabatic-to-Diabatic
BLKS	Block Localized Kohn-Sham
BLYP	Becke Exchange and Lee Yang Parr correlation functional
CASPT2	Complete Active Space Self-Consistent Field with second order perturbation
CASSCF	Complete Active Space Self-Consistent Field
CCSD	Coupled-Cluster Singles and Doubles
CCSD(T)	Coupled-Cluster Singles and Doubles with Perturbative Triples
CI	Configuration Interaction
CSF	Configuration State Function
DAC	Diabatic-at-Construction
DC	Derivative Coupling
DFT	Density Functional Theory
DTS	Dynamic then Static
FCI	Full Configuration Interaction

GD	Gradient Difference
GGA	Generalized Gradient Approximation
HF	Hartree-Fock
KS-DFT	Kohn-Sham Density Functional Theory
LDA	Local Density Approximation
M06-2x	Minnesota Density Functional 2006 with 54 % HF exchange
M06-HF	Minnesota Density Functional 2006 with 100% HF exchange
MCSCF	Multiconfiguration Self-Consistent Field
MS-CASPT2	Multistate Complete Active Space Self-Consistent Field with second order Perturbation Theory
MM	Molecular Mechanics
MO	Molecular Orbital
MOVB	Molecular Orbital Valence Bond Theory
MP2	Second order Møller-Plesset Perturbation Theory
MRCI	Multireference Configuration Interaction
MRPT	Multireference Perturbation Theory
MSDFT	Multistate Density Functional Theory
MUD	Mean Unsigned Deviation
MUE	Mean Unsigned Error
NC-SF-TDDFT	Noncollinear Spin Flip Time Dependent Density Functional Theory

PBE	Perdew, Burke and Ernzerhof exchange and correlation functional
PBE0	Hybrid Perdew, Burke and Ernzerhof functional
PBEC	Perdew, Burke and Ernzerhof correlation functional
PES	Potential Energy Surface
PM3	Parameterized Model 3
QM	Quantum Mechanics
QM/MM	Combined Quantum Mechanics and Molecular Mechanics
RO-KS	Restricted Open Shell Kohn-Sham
SA-TDDFT	State average Time Dependent Density Functional Theory
SCVB	Spin Coupled Valence Bond Theory
SF-TDDFT	Spin Flip Time Dependent Density Functional Theory
TDDFT	Time Dependent Density Functional Theory
TDF	Transition Density Functional
VB	Valence Bond Theory
WFT	Wave Function Theory
XMC-QDPT	Extended Multiconfigurational Quasi-degenerate Perturbation Theory

Simulation and Spectroscopy

2DIR	Two-Dimensional Infrared spectroscopy
ABNR	Adopted Basis Newton-Raphson energy minimization
CLS	Center Line Slope
DAF	Dipole Autocorrelation Function
DVR	Discrete Variable Representation
FFCF	Frequency-Frequency Time Correlation Function
FTIR	Fourier Transform Infrared spectroscopy
FWHM	Full Width at Half Maximum
NPT	Isobaric Isothermal Ensemble
PO-DVR	Potential Optimized Discrete Variable Representation
QVPn	n^{th} order Quantum Vibration Perturbation Theory
VCI	Vibrational Configuration Interaction

Molecules

CCL4	Carbon tetrachloride
CHCL3	Chloroform
DEET	Diethyl ether
DHT	didehydrotoluene

DMA	N,N-dimethyl acetamide
HCl	Hydrogen chloride
LiH	Lithium hydride
MeCN	Acetonitrile
MeOH	Methanol
TriMOS	Trimethoxy silane
TriPS	Triphenyl silane

Chapter 1. Beyond Kohn-Sham Approximation: Hybrid Multistate Wave Function and Density Functional Theory

This work was performed in collaboration with Jiali Gao, Haisheng Ren and Peng Bao.

1.1. Introduction

Kohn-Sham density functional theory (KSDFT) and linear-response time-dependent density functional theory (TDDFT) have become indispensable tools for studying ground state and excited states of atoms and molecules as well as condensed-phase materials thanks to their balance of accuracy and efficiency.[1] Despite the remarkable success, they are typically not adequate to treat strongly correlated systems with characteristic features of multiple unpaired electrons and degenerate or nearly degenerate electronic states.[2-5] A particular example is illustrated by conical intersections at geometries where two or more electronic states are degenerate; here, TDDFT fails completely although it often performs very well in vertical excitation energies for many molecules with errors of less than ~0.3 eV.[6] The role of conical intersections in photochemistry to allow efficient non-radiative transitions has been well-established, and they are also essential in many nonadiabatic processes.[7, 8] The standard approaches to probe conical intersections are based on multireference (MR) wave function methods at much greater computational costs, such as the complete active space self-consistent field (CASSCF) and the multireference configuration interaction (MRCI) models.[9-11] The

failure of TDDFT to describe conical intersections is also well-known;[2] there is a lack of interaction between the ground (reference) state and the excited (response) states. Consequently, the branching space, defined by the gradient difference and derivative coupling vectors, has only one degree of freedom, and this greatly impedes their applications to photochemistry.

Several methods have already been developed to introduce coupling between the ground state and excited states in DFT. A natural modification of the original formalism is the spin-flip (SF) TDDFT,[12] which starts from a variationally optimized high-spin state (*e.g.*, the triplet state) to generate the lower spin ground and excited states (S_0, S_1, etc.) by single-electron transitions along with an $\alpha \rightarrow \beta$ spin inversion. Hence, the singlet ground and excited states are treated in the same footing to correctly recover the dimensionality of the intersection space. The SF-TDDFT method has been applied to a variety of systems and used in geometry optimization to conical intersections.[4, 13] Working in the framework of TDDFT, Li et al. replaced the matrix elements of the Tamm-Dancoff approximation by the wave function results to introduce coupling between the reference ground state and excited state.[14] Yang et al., on the other hand, started from a two-electron deficient (N-2) reference to target the neutral (N) ground state and excited states by adding two electrons, thereby, both the ground and excited states are modeled in the same way to break the unphysical degeneracy.[3] An alternative approach is based on ensemble DFT,[15, 16] which has been extended to include state interaction (SI) along with state-average (SA) optimizations.[17] Along a similar line, configuration interaction using

constrained or block-localized DFT have been used to describe ground and excited states and the conical intersections.[18, 19]

In this chapter, we present a multistate density functional theory (MSDFT) to determine conical intersections and to model systems intrinsically characterized by degenerate states. Furthermore, MSDFT provides a "dynamic-then-static" framework to treat electron correlation by including dynamic correlation in the active configurations first, followed by diagonalization of the Hamiltonian in the dynamically correlated states to incorporate static correlation. MSDFT builds up on and makes use of the vast resources and excellent performance of the approximate density functional developed in KSDFT, yet it is practical for treating systems that are difficult by KSDFT and too large by accurate wave function theory (WFT).

1.2. The Dynamic-Then-Static Ansatz

Liu and Hoffmann recently categorized methods for treating electron correlation into three main families based on the order that static and dynamic correlation effects are evaluated:[20] (1) static-then-dynamic, (2) dynamic-then-static, and (3) static-dynamic-static. They presented an iterative configuration interaction approach,[20, 21] which falls into the static-dynamic-static category. The first category includes a large majority of multireference perturbation methods in WFT, and further discussion of these approaches is provided in reference 20.

In the dynamic-then-static category[22] used in the present multistate density functional theory, the key idea is to first construct an effective Hamiltonian for a primary or active space, consisting of N_p determinants or equivalently spin-adapted

configuration state functions (CSF), $\{|\Psi_A>; A=1,\cdots,N_p\}$, such that dynamic correlation is included. In the second step, the adiabatic ground and excited states are determined by configuration interaction among the states in the active space. The active space typically consists of low-lying energy configurations. A special case is when $N_p=1$, in which the ground state is well separated from all other states and single reference methods (such as KSDFT) can be adequately used. It is of particularly interest to consider systems with strong correlations, including a description of the conical intersections of different potential energy surfaces. In this case, more than one state is needed, but a small number will be sufficient in the active space, and this is the focus of the present study.

The effective Hamiltonian for the active space is formally constructed by contracting the effects (*i.e.*, dynamic correlation) of the remaining N_x states in the full CI (FCI) spectrum of the Schrödinger equation for an *n*-electron system, where $N_x = N_f - N_p$ with N_f being the total number of FCI states. The *I*th low-lying energy state $|\Phi_I>$ ($I \le N_p$) of the FCI solution is written in terms of the active states:[20]

$$|\Phi_I> = \sum_{a=1}^{N_f} c_a |\psi_a> = \sum_{A=1}^{N_p} C_{AI} |\Psi_A> \qquad (1.2.1)$$

where $|\psi_a>$ spans all possible determinants (FCI) for the *n*-electron system and the second equation is a single value decomposition of the FCI vector, $\mathbf{c} = \mathbf{U\sigma V}^\dagger = \mathbf{UC}$, of rank N_p. The contracted functions that form the active space are formally defined by

$$|\Psi_A> = \sum_{a=1}^{N_f} U_{aA} |\psi_a> \qquad (1.2.2)$$

which includes all dynamic correlation from states external to the active space.

A critical issue to make this approach practical is to incorporate dynamic correlation in equation 1.2.2 without a knowledge of the coefficients $\{U_{aA}\}$ in the first place. This is accomplished in MSDFT by projecting the total correlation energy in DFT on to $\{|\Psi_A>\}$,[19] which separates static correlation among the active state, with dynamic correlation included for each individual configuration.

1.3. Multistate Density Functional Theory

In the "dynamic-then-static" ansatz, there are two computational steps: (1) the definition and optimization of the active states, and (2) the diagonalization of the effective Hamiltonian to yield the adiabatic ground and excited states. Although delocalized molecular orbitals can be used to define $\{|\Psi_A>\}$, an equivalent, localized valence-bond (VB) representation is more illustrative for discussion and intuitive for interpreting results, and this is used in the following discussion.

For a given Lewis structure, the *n*-electron molecular system is partitioned into M_A fragments also called blocks, each consisting of n_m electrons ($\sum n_m = n$) and μ_m atomic orbital basis functions. A block-localized (BL) determinant is written as

$$|\Psi_A> = N_A \hat{A}\{\varphi_1^A \cdots \varphi_{M_A}^A\} \qquad (1.3.1)$$

where $\hat{A}$ is the antisymmetrizer, N_A is a normalization factor, and φ_m^A is a product of block-localized Kohn-Sham (BLKS) orbitals of fragment *m*. These orbitals are linear combinations of the atomic basis assigned to the corresponding block; they are orthogonal within a given block, but non-orthogonal in different blocks. Spin-adapted

CSFs are constructed by combining several determinants to represent the corresponding covalent and ionic states. The functions $\{|\Psi_A>\}$ are variationally optimized separately as in standard KSDFT, except that the electron density is obtained from non-orthogonal BLKS orbitals for the particular state.[19]

In MSDFT, the diagonal matrix elements of the effective Hamiltonian are simply the KSDFT energies of the BLKS determinants:

$$H_{AA} = E^{\mathrm{KS}}[\rho_A^{\mathrm{ms}}(\mathbf{r})] \tag{1.3.2}$$

where $\rho_A^{\mathrm{ms}}(\mathbf{r})$ is the electron density for state *A*, and any "standard" (LDA, GGA or hybrid) exchange-correlation functional $E_{xc}^{\mathrm{KS}}[\rho_A^{\mathrm{ms}}(\mathbf{r})]$ can be used to determine $E^{\mathrm{KS}}[\rho_A^{\mathrm{ms}}(\mathbf{r})]$, although the computational details are slightly different,[19] involving non-orthogonal orbitals.

The off-diagonal matrix elements can easily be determined in WFT,[23-25] and they are functions of the individual states as well as the transition density $\rho_{AB}(\mathbf{r}) = <\Psi_A|\hat{\rho}(\mathbf{r})|\Psi_B>$, and this has be used previously in the mixed molecular orbital and valence bond (MOVB) theory.[25] However, a density functional dependent on the transition density does not exist within the KSDFT framework. In MSDFT, the concept of transition density functional (TDF), $E^{\mathrm{TDF}}[\rho_{AB}(\mathbf{r})]$, between states $|\Psi_A>$ and $|\Psi_B>$ is introduced to determine the off-diagonal matrix elements. It includes two components: (1) the electronic coupling between the non-orthogonal wave functions (dominantly for static correlation), and (2) a transition density contribution to account for

dynamic correlation interactions between coupled states. Although there is currently no density functional approximation to $E^{\mathrm{TDF}}[\rho_{AB}(\mathbf{r})]$ in the KSDFT framework, it can be approximated in a similar way as in KSDFT:[1]

$$H_{AB} \equiv E^{\mathrm{TDF}}[\rho_{AB}(\mathbf{r})] = <\Psi_A | H | \Psi_B> + V_c^{\mathrm{TDF}}[\rho_{AB}(\mathbf{r})] \qquad (1.3.3)$$

Here, H is the electronic Hamiltonian, and the exact (wave-function type) exchange between states $|\Psi_A>$ and $|\Psi_B>$ with an overlap $S_{AB} = <\Psi_A|\Psi_B>$ is automatically included in the first part, whereas only correlation contribution is grouped into the density functional in the second term. Although a density functional directly dependent on $\rho_{AB}(\mathbf{r})$ may be developed, to forge ahead, it is approximated by an overlap-weighted average of the KS correlation energies for the two interacting states:[19, 26]

$$V_c^{\mathrm{TDF}}[\rho_{AB}(\mathbf{r})] \approx \frac{\lambda}{2} S_{AB} (E_c^{\mathrm{KS}}[\rho_A^{\mathrm{ms}}(\mathbf{r})] + E_c^{\mathrm{KS}}[\rho_B^{\mathrm{ms}}(\mathbf{r})]) \qquad (1.3.4)$$

where λ is unity, but it could be optimized in the future either as a parameter or as a functional. Note that the approximation in equation 1.3.4 for the correlation contribution to the TDF correctly reduces to the pure state limits ($A = B$).

The coefficients $\mathbf{C} = \{C_{AI}\}$ in equation 1.2.1 are determined by diagonalizing the generalized secular equation $\mathbf{HC} = E\mathbf{SC}$. Consequently, the electron density and energy functional for the ground state ($I = 0$) and the excited ($I \le N_p$) states, $|\Phi_I>$, in MSDFT are given as follows

$$\rho_I(\mathbf{r}) = \sum_{A=1}^{N_p} \{C_{AI}^2 \rho_A^{\mathrm{ms}}(\mathbf{r}) + \sum_{B \neq A} C_{AI} C_{BI} \rho_{AB}(\mathbf{r})\} \qquad (1.3.5.a)$$

$$E_I^{\mathrm{MS}}[\rho_I(\mathbf{r})] = \sum_{A=1}^{N_p} \{C_{AA}^2 E^{\mathrm{KS}}[\rho_A^{\mathrm{ms}}(\mathbf{r})] + \sum_{B\neq A} C_{AI} C_{BI} E^{\mathrm{TDF}}[\rho_{AB}(\mathbf{r})]\} \qquad (1.3.5.b)$$

Note that Coulson structure weights $\{w_A\}$ can be obtained from the coefficients $\{C_{AI}\}$, providing a quantitative measure of the relative contributions of configurations in the active space.[27] Equations 1.3.5 are the key results of this work.

Several remarks can be made: (a). In MSDFT, the ground state density ρ_0 is a configuration-weighted sum of electron densities from multiple determinants as well as contributions from their transition densities (equation 1.3.5.a), and the ground state energy is written as an implicit functional of ρ_0 with the same structural weights on the basis configurations in the active space (equation 1.3.5.b). If the ground state for a system is well separated from all other states, *i.e.*, $N_p = 1$, MSDFT naturally reduces to KSDFT (see below). For situations involving degenerate or nearly degenerate states, the system-dependent static correlation is treated with two or more configurations.

(b). The electron densities and energy functionals for the excited states are treated exactly on the same footing as the ground state in MSDFT (equations 1.3.5). Therefore, the method provides excitation energies and has the correct dimensionality to describe conical interactions. The physical basis for a multideterminant representation of the ground state density has long been established in ensemble density functional theory.[15, 16, 28] Although there are similarities, MSDFT differs from ensemble density functional theory because transition density functional is introduced to account for electronic coupling between different states (equation 1.3.3).[5] Equation 1.3.5 is consistent with the ensemble v_s-representability in ensemble density functional theory since the

determinants[29] in MSDFT can easily be orthogonalized.[30] Importantly, the density and functional in equations 1.3.5 are not the "ensemble" density and energy, but rather they represent the electron densities and energies of the corresponding adiabatic ground and excited states of the system. Note also that a thermally-assisted-occupation DFT method[31, 32] that employs fractional occupations as in the grand canonical approach has been developed to represent the multideterminant character for systems with strong correlation with good results for the ground state.

(c). The ground state energy in many multiconfiguration DFT methods is typically obtained by adding the pure dynamic correlation from KSDFT to the MR energy that takes into account static correlation, $E^{\mathrm{MR}} + E_{xc}^{\mathrm{KS}}[\rho_0]$. However, since static and dynamic correlations are not separable, this combination results in double counting of correlation effects. In MSDFT, ρ_0 is not used directly to determine dynamic correlation. The latter is obtained as a configuration-weighted (not to be confused with the "ensemble weight" in EDFT) sum of the pure dynamic correlation within each (localized) determinant: $E_c^{\mathrm{MS}}[\rho_0(\mathbf{r})] = \sum_A w_{A0} E_{xc}^{\mathrm{KS}}[\rho_A^{\mathrm{ms}}(\mathbf{r})]$, where w_{A0} is a Coulson configuration weight. Thus, non-dynamic correlation is excluded from E_c^{MS} by construction. However, $E_{xc}^{\mathrm{KS}}[\rho_A^{\mathrm{ms}}(\mathbf{r})]$ contains a component that may be regarded as dynamic correlation within the active space. This part of the correlation can be approximated and removed using second-order Møller-Plesset perturbation theory (MP2) with the restriction that only active orbitals are included,

$$E_{xc}^{\mathrm{KS2}}[\rho_A^{\mathrm{ms}}(\mathbf{r})] = E_{xc}^{\mathrm{KS}}[\rho_A^{\mathrm{ms}}(\mathbf{r})] - \sum_{i<j}^{\in A}{}' \sum_{a<b}^{\in A}{}' \frac{|(ia|jb) - (ib|ja)|^2}{\varepsilon_i + \varepsilon_j - \varepsilon_a - \varepsilon_b}. \quad (1.3.6)$$

where the summations run over occupied (*i* and *j*) and unoccupied (*a* and *b*) orbitals defining the active space in configuration *A*, and the superscript KS2 indicates that dynamic correlation estimated by MP2 in the active space has been removed from the KS functional. The primes indicate that the summations are limited within a given block and only the BLKS orbitals corresponding to those used to form the active space (*i.e.*, spin-coupled configurations) with an energy gap greater than 0.01 *a.u.* are included. Because the number of orbitals in the active space are very small compared to the virtual space, the correction to remove double counting of dynamic correlation introduces little extra computational costs.

Furthermore, one could construct a first-order factor, similar to that introduced by Savin and coworkers,[33]

$$\gamma_A = 1 - E_A^{(2)} / E_A^{\mathrm{MP2}} \quad (1.3.7)$$

where $E_A^{(2)}$ is the second term in equation 1.3.6 and E_A^{MP2} is the total MP2 energy for state $|\Psi_A>$. Thus,

$$E_{xc}^{\mathrm{KS2}}[\rho_A^{\mathrm{ms}}] = \gamma_A E_{xc}^{\mathrm{KS}}[\rho_A^{\mathrm{ms}}] \quad (1.3.8)$$

which reduces exactly to $E_{xc}^{\mathrm{KS}}[\rho_A^{\mathrm{ms}}]$ for a single determinant (since there is no unoccupied orbital in the active space), and $E_{xc}^{\mathrm{KS2}}[\rho_A^{\mathrm{ms}}] = 0$ in the limit of full CI, when all virtual orbitals are in the active space (thus, $E_A^{(2)} = E^{\mathrm{MP2}}$). Higher order

perturbations could be used, which would greatly increase computational costs; however, this provides a simple and systematic connection from KSDFT to FCI. Therefore, the MSDFT approach may be regarded as a WFT and DFT hybrid.

(d). This brings me to another possible approximation for the dynamic correlation contribution to the transition density functional in equation 1.3.3 using perturbation theory:

$$V_c^{\mathrm{TDF}}[\rho_{AB}] \approx <\Psi_A|H|\Psi_B^{(1)}> + <\Psi_A^{(1)}|H|\Psi_B> + <\Psi_A^{(1)}|H|\Psi_B^{(1)}> \qquad (1.3.9)$$

where $|\Psi_A^{(1)}>$ and $|\Psi_B^{(1)}>$ are first-order corrections to $|\Psi_A>$ and $|\Psi_B>$. The first two terms and the last term in equation 1.3.9 account for, respectively, dynamic contributions from the active-external block and external-external block, respectively. Equation 1.3.9 and its high-order generalization may be used to guide the development an explicit transition density functional. Note that the zeroth-order term is already included in equation 1.3.3.

(e). In MSDFT, the BLKS orbitals are variationally optimized by KSDFT, independently for each determinant state; the BLKS orbitals are fully relaxed, non-orthogonal and different for different configurations. This is different from typical CI and state-average MCSCF approaches in WFT, in which a common set of orbitals are used for all configurations. The procedure provides an optimal and a clear definition of the reference state for dynamic correlation via KSDFT (as compared to MRPT). Since the orbitals for each state have been individually optimized, just a diagonalization of the Hamiltonian is needed, rather than simultaneous optimization of both the orbital and configurational coefficients as in MCSCF.

(f). The reference function defined by equation 1.3.1[19, 25] may be compared with the spin-coupled valence bond (SCVB) method[34, 35]. In SCVB, delocalized single-electron orbitals are used among which all spin-coupled configurations are included; in the limit of including ionic VB configurations, SCVB is equivalent to CASSCF with *n* electrons in *n* orbitals. On the other hand, in MSDFT, orbitals are block localized and spin coupling is taken into account only between blocks critical for bonding interactions of interest (*e.g.*, the electron pair involved in the dissociation of a single bond). A single block-localized determinant (BLKS determinant) is employed to approximate the SCVB function for the entire block, greatly reducing the number of configurations in the active space. Because orbitals are block localized, the inclusion of ionic VB-like configurations is more important in MSDFT to represent charge delocalization than that in SCVB. Of course, dynamic correlation is incorporated in the reference functions in MSDFT, whereas it is treated as a post-SCF correction in SCVB.[34, 35]

(g). The MSDFT method provides a strategy to directly obtain diabatic states at construction (DAC),[36] which will be presented elsewhere.

1.4. Results and Discussion

The MSDFT calculations are performed using a modified version of GAMESS. Two representative systems involving symmetry-induced intersections in Jahn-Teller molecules and the potential energy surfaces in the photodissociation of NH_3. The PBE0 density functional is used in all computations with the cc-pVDZ basis for the Jahn-Teller systems and aug-cc-pVTZ for ammonia. For open-shell systems spin-polarized (unrestricted) KSDFT[37] is used and the procedure for optimizing block-localized orbitals

has been described in references 19, 25. These systems are chosen because they have previously been studied and their excitation energies and conical intersections have been well-characterized for comparison.

Jahn-Teller active molecules, such as cyclopropenyl radical ($C_3H_3^{\bullet}$) and benzene cation radical ($C_6H_6^{+\bullet}$), represent a special type of conical intersection, where the degeneracy of the electronic state is lifted by non-totally symmetric vibrations. An insightful analysis was provided by Paterson et al.[38] Here, we focus on the qualitative description of the intersections with MSDFT by using just the covalent VB configurations in the active space, while quantitative energies can be obtained by including ionic (zwitterion bond) configurations in the treatment. The Jahn-Teller geometries at the conical intersections are optimized for $C_3H_3^{\bullet}$ at the D_{3h} symmetry and for C_6H_6 at the D_{6h} symmetry.

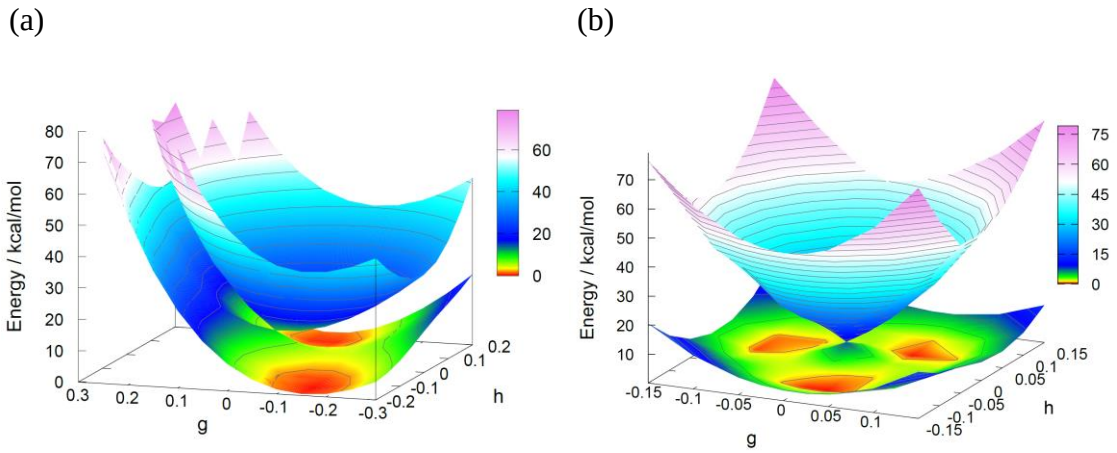

Figure 1.1. Computed potential energy surfaces for the ground and the first excited state for cyclopropenyl radical (a) and benzene cation radical (b) along the gradient difference (g) and derivative coupling (h) vector directions (see text).

For $C_3H_3^{\bullet}$, there are three possible spin combinations in the covalent VB space, each consisting of four orbital blocks to represent the σ-framework (18 electrons) and three singly occupied *p*-orbitals on carbon atoms. At the symmetry-induced conical interaction, the gradient difference (*GD*) and derivative coupling (*DC*) vectors are described by Paterson et al.,[38] which are the e' normal vibrational modes lying in the molecular plane.[38] The potential energy surfaces along these two coordinates are depicted in Figure 1.1.a for the ground and excited states. Restricting the planar geometry, distortion along the *GD* vector leads to a saddle point at C_{2v} symmetry on the ground-state PES with one short and two long CC bonds, which separates two energy minima, also of C_{2v} symmetry but having one long and two short CC distances. Moving away from the C_{2v} symmetry along the *DC*(*h*) direction results in a cone from MSDFT; however, TDDFT produces a spurious seam with KSDFT reference energy higher than the TDDFT excited state (not shown).

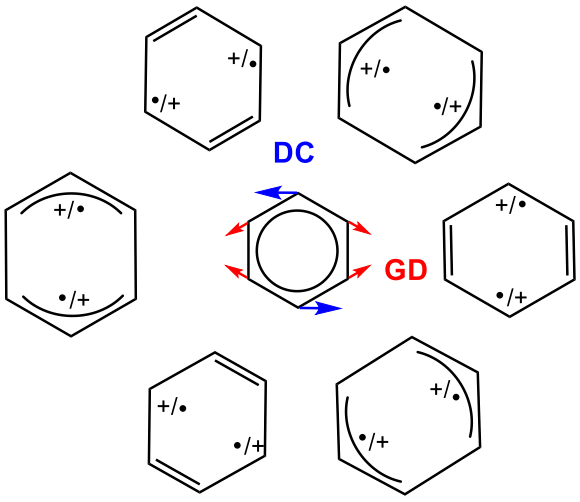

Scheme 1.1. Schematic representation of the valence bond configurations used in MSDFT for benzene cation radical. Deformation from the D_{6h} Jahn-Teller geometry in the center along the gradient difference vector (red) leads to the quinoid configuration on the right, and the antiquinoid structure on the left. There are three equivalent pairs forming the moat around the conical intersection.

The Jahn-Teller geometry and ultra-fast electron dynamics at the conical intersection of $C_6H_6^{+\bullet}$ can be probed by photoelectron spectroscopy, and have been studied by Robb and coworkers.[39, 40] As pointed out by these authors,[39, 40] the moat around the conical intersection is characterized by three pairs of quinoid and antiquinoid VB configurations with the former as the minima and the latter as the transition states on the ground-state PES. We used 12 configurations (Scheme 1.1), including different cation and radical combinations to represent the VB states in MSDFT, to yield the PES shown in the branching space (Figure 1.1.b). Following Vacher et al.,[41] the vibrational mode that leads to the quinoid structure represents to the *GD* vector, and that has sheered motions of atoms on the opposite side corresponds to the *DC* vector (Scheme 1.1). The energies at the critical points in this minimum active space are about 0.2 to 0.3 eV higher than the CASSCF values,[40] but the key features of the adiabatic potential energy surfaces are fully characterized in comparison with the CASSCF surface (Figure 1.1.b), in accord with the VB-based interpretation by Robb and coworkers.[39, 40]

Photodissociation of NH_3 to NH_2 + H has been extensively studied and it is chosen because this process has been considered to embody the key challenges encountered in strongly correlated dissociative potential energy surfaces.[42, 43] We employed 12 CSFs for the ground and excited states (Figure 1.2). Specifically, each σ_{NH}-bond is described by a spin-adapted covalent configuration

$|\sigma_{\mathrm{cov}}^{\mathrm{NHa}}>=N_{\mathrm{cov}}^{\mathrm{a}}(\hat{A}\{\varphi_c^6 n^2 \varphi \bar{s}_{\mathrm{H}}\}+\hat{A}\{\varphi_c^6 n^2 \bar{\varphi} s_{\mathrm{H}}\})$ along with two ionic states, and the nσ* state is represented by $|\sigma_{ex}^{\mathrm{NHa}}>=N_{ex}^{\mathrm{a}}(\hat{A}\{\varphi_c^8 \bar{n} s_{\mathrm{H}}\}+\hat{A}\{\varphi_c^8 n \bar{s}_{\mathrm{H}}\})$. In all calculations two of the N-H bonds are fixed at the experimental value (1.055 Å), which is slightly longer than MRPT result (1.039 Å), and the three H-N-H angles are kept at 120°.[42]

The ground state (1 A_1) minimum of NH_3 has a C_{3v} symmetry, and it is changed to D_{3h} at the excited state (2 A_1) equilibrium. The total energy of NH_3 at the ground-state minimum is -56.51832 *a.u.* from MSDFT, which is slightly lower than the PBE0 value (-56.51661 *a.u.*), suggesting that there is little double counting of correlation. The adiabatic excitation energy is estimated to be 6.10 eV (Figure 1.2), slightly greater than experiment (5.92-5.96 eV). Along the minimum-energy path of a stretched N-H bond (reduced to B_1 state), a saddle point is encountered before reaching the conical intersection between the two surfaces at a C_{2v} symmetry. The conical intersection is located at 2.163 Å with an energy of 5.36 eV above ammonia, which is somewhat longer than the minimum-energy (5.16 eV) conical intersection point (1.990 Å) determined by Truhlar and coworkers;[42] the agreement is reasonable considering that the excited state geometries are not fully optimized in the present study. The transition state is found at 1.284 Å with a barrier height of 0.24 eV, in concert with the best available values (1.298 Å and 0.22 eV).[42] The good agreement between MSDFT with experimental and computational results shows that the present multistate approach can provide quantitative description of the PES for ammonia photodissociation. For comparison, without including dynamic correlation in the CSFs using the mixed molecular orbital and valence bond (MOVB) method, the

computed bonding energy and excitation energy are, respectively, about 1 and 0.6 eV smaller than those from MSDFT and experiments.

The insert in Figure 1.2 shows that the degeneracy at the conical intersection is lifted by moving away from the planar geometry, producing a correct double-cone topology using MSDFT. However, as shown previously,[3, 14] KSDFT and TDDFT calculations result in a spurious curved seam of intersections due to incorrect dimensionality. Furthermore, these calculations also suffer from convergence and instability issues with imaginary eigenvalues. For comparison, CASSCF calculations require a (8,7) active space (490 determinants), but most are high-lying energy states that are unimportant to A_1-B_1 state coupling, while quantitative results can only be obtained with MRPT correction to account for dynamic correlation. In MSDFT, dynamic correlation is built into the CSFs, and a multistate approach using a standard density functional developed for KSDFT, with 12 CSFs (18 determinants) in the present study, is able to quantitatively capture the key features involving strongly coupled dissociative surfaces.

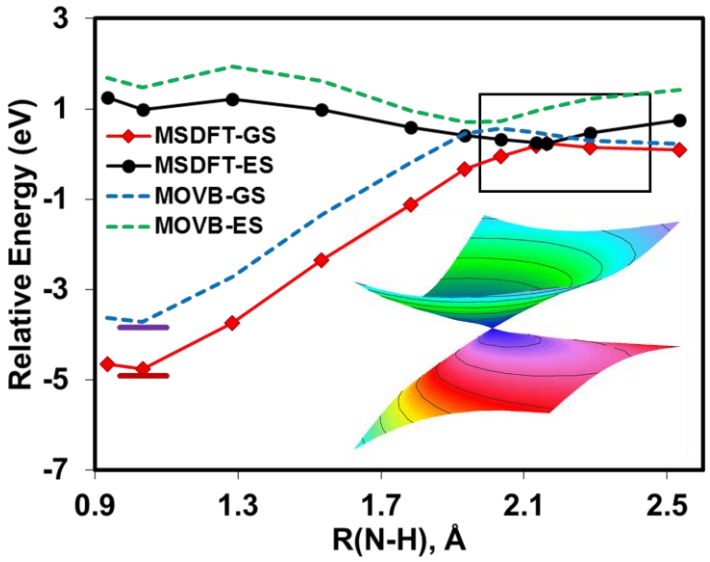

Figure 1.2. Potential energy curves of the ground and nσ* excited states of planar NH3 along a stretched N-H bond at the C_{2v} symmetry using MSDFT and mixed molecular orbital and valence bond (MOVB) calculations. The two horizontal bars are the MSDFT and MOVB (WFT without dynamic correlation) energies at the optimized geometry of ammonia at the C_{3v} symmetry. The insert depicts the double cone topology of the potential energy surfaces in the branching space as the dissociating hydrogen moving away from the planar geometry and the improper dihedral angle moves away from planarity. The PBE0 density functional and aug-cc-pVTZ basis set are used in MSDFT calculations.

1.5. Conclusions

In summary, we propose a multistate density functional theory for treating systems with strong correlation and describing the conical intersections between strongly coupled dissociative potential energy surfaces. MSDFT is different from ensemble DFT because the electron densities and energies for ground and excited states are obtained on the same footing; a transition density functional is introduced to account for state interactions. If the ground state for a system is well separated from all other states, only one configuration is needed and MSDFT naturally reduces to KSDFT. In the limit that all virtual orbitals are included in the active space, MSDFT becomes FCI as in wave

function theory. Thus, MSDFT can be regarded as a hybrid DFT and WFT. The method is built on and makes use of the vast resources of the approximate density functional developed in KSDFT, yet it retains its computational efficiency to treat strongly correlated systems that are problematic using KSDFT, but too large for accurate WFT. Excellent qualitative and quantitative results have been obtained in the test cases, including Jahn-Teller active molecules and the photodissociaiton of ammonia. The results presented here show that MSDFT can be applied to photochemical processes involving conical intersections.

Chapter 2. Diabatic-At-Construction (DAC) Method for Diabatic and Adiabatic Ground and Excited States Based on Multistate Density Functional Theory

This work was performed in collaboration with Zexing Qu and Jiali Gao.

2.1. Introduction

The diabatic representation of potential energy surfaces (PESs) and their interactions is useful for electronically nonadiabatic processes, especially those involving conical intersections of the adiabatic states, because it provides a smooth description of the PESs and represents their couplings in terms of the smoothly varying off-diagonal matrix elements of the scalar electronic Hamiltonian.[7, 25, 36, 44-50] In contrast, the adiabatic PESs, which diagonalize the electronic Hamiltonian, exhibit rapid variations and cuspidal ridges as functions of the nuclear coordinates in these regions, and the adiabatic states are coupled by the vector nuclear momentum operators; these couplings, called nonadiabatic couplings or derivative couplings, are not smooth with singularities at the cuspidal ridges, making them difficult to use in dynamic simulations.[51, 52] The most common way to treat coupled PESs is by wave function theory (WFT) with multireference (MR) methods; however, accurate calculations are very expensive, usually restricting their applications to

small molecules. Density functional theory (DFT) may be the ultimate method in the long-term, but the currently available linear-response time-dependent density functional theory (TDDFT) has the wrong dimensionality for conical intersections involving the ground (reference) state.[2, 5] (This shortcoming can be overcome by modifying the theory,[3, 4, 14] but we shall not pursue that line of approach in the present article.) The present article considers a combination of DFT and WFT that goes beyond the current Kohn-Sham approximation[53] and has advantages compared to using either alone. This article has two objectives: (1) to describe a multistate density functional theory (MSDFT) for constructing quasidiabatic states, and (2) to establish a relationship between the diabatic states obtained from MSDFT and those by the threefold-way diabatization approach.[46, 54]

The nonadiabatic coupling matrix elements are $< \Psi_A(\mathbf{r};\mathbf{R}) | \nabla_R | \Psi_B(\mathbf{r};\mathbf{R}) >$, where $| \Psi_A(\mathbf{r};\mathbf{R}) >$ and $| \Psi_A(\mathbf{r};\mathbf{R}) >$ are adiabatic wave functions for states *A* and *B*, and **r** and **R** specify respectively electronic and nuclear coordinates.[55] Diabatic states (sometimes called quasidiabatic states) are those that make the coupling by nuclear momentum operators negligible or as small as possible. In the general case the nonadiabatic couplings cannot be made to completely vanish,[56] and the transformation to states that make them small is not unique. Numerous approaches have been proposed to model diabatic states.[50, 57-63,49, 64-68,46, 54, 69-72,73-76] A thorough comparison of these methods is beyond the scope of this work, but, instead, we roughly classify them into two categories on the basis of the relationship between diabatic and adiabatic states: (1) adiabatic-to-diabatic (ATD), and (2) diabatic-at-construction (DAC).

2.1.1. Adiabatic-To-Diabatic via similarity transformation:

The ATD category involves similarity transformations of adiabatic states to yield orthogonal diabatic states. In some of these methods, the diabatic states when diagonalized exactly reproduce the adiabatic PESs. A prerequisite is a set of adiabatic states, including (usually) the ground state and the relevant excited states, and the resulting diabatic states depend not just on the diabatization method but also on the choice of how many and which states to include in the transformation. Then, a similarity transformation is used to produce a diabatic representation having the desired properties. The adiabatic states can be obtained qualitatively from multiconfiguration self-consistent-field (MCSCF) calculations such as the state-averaged complete-active-space type (SA-CASSCF),[77] but this method does not yield quantitative PESs because of insufficient dynamic correlation. More quantitative results can be obtained by multireference perturbation theory (MRPT)[78-80] or multireference configuration interaction (MRCI).[9-11] These methods are restricted to relatively small molecules by high computation costs. For larger molecular systems, Kohn-Sham density functional theory (KS-DFT) and linear-response time-dependent DFT (TDDFT) are more efficient ways to include dynamic correlation.[1] Here we use a multistate approach[19, 26, 53] that extends the approximate density functional theory beyond KS-DFT for applications to photochemistry.

Given a set of adiabatic ground and excited states, one diabatization procedure is to minimize the derivative couplings along a given reaction path by making use of energies, gradients, and derivative couplings at selected points.[49, 67, 68] Another strategy is to approximate the diabatic states according to pre-defined, smoothly varying orbitals along

with the condition of configurational uniformity.[46, 50, 54, 69, 70] Alternatively, one could carry out orbital-free diabatization by employing dipole moments, quadrupole moments, electrostatic potentials, and transition moments, and these have been used recently and tested on several molecular systems.[75, 76] Several other ATD diabatization schemes are available, and the reader is referred to recent papers for additional methods and additional references.[81-83]

2.1.2. Diabatic-At-Construction by experimental validation

The diabatic states in the DAC category are often non-orthogonal. For example, they may be chosen on the basis of the electronic configurations of reaction products at the asymptotic dissociation limits, and the valence bond (VB) character of the electronic state may be maintained at all molecular geometries.[18, 19, 24, 25, 36, 84-87] Rather than back-transforming the delocalized adiabatic states, the diabatic states are constructed in the first place as the spin-adapted configuration state functions (CSFs) that serve as a basis for direct calculation of the adiabatic ground state and excited states. Although diabatic states are not unique[56] and their properties are not physical observables, states of the DAC type can be validated by comparison with experiments on observables of the resulting adiabatic ground and excited states. Such comparisons can also provide physically meaningful interpretations of delocalized adiabatic states.

A procedure to construct diabatic states by contracting the eigenvectors from ab initio VB calculations has been described;[36] it involves a CSF space of the multi-configuration self-consistent-field (MCSCF) type. In practice, VB-based diabatic states can be conveniently formulated by block-localized molecular orbitals (BLMO) according

to the Lewis resonance structures for a given chemical system,[88-90] and this has been used in the mixed molecular orbital and valence bond (MOVB) method for studying chemical reactions and charge transfer processes in the context of combined quantum mechanical and molecular mechanical (QM/MM) simulations.[24, 25] The use of BLMO or block-localized Kohn-Sham (BLKS) orbitals reduces a large number of valence bond configurations to a manageable number; only those critical to a given system are retained in a way analogous to the spin-coupled valence bond theory.[34, 35] This method has been extended to density functional theory, in which case it is called multistate density functional theory (MSDFT),[19, 26, 53, 91, 92] and this is the method that is used in the present work.

A related approach is constrained density functional theory[87] that confines the electron density within finite spatial regions to define constrained states. For comparison, localized states are defined in orbital space in MSDFT. The difference is reflected in the computed transfer integrals for electron transfer reactions, where constrained DFT showed,[93] incorrectly, non-exponential dependency with donor-acceptor distance and the computed values can vary as much as five orders of magnitude with different fractions of Hartree-Fock exchange used in a functional.[93] MSDFT does not suffer from electron-transfer contamination of diabatic states found in spatial localization of density, and there is little-to-no dependency on the amount of HF-exchange used.[26]

The LiH molecule, being the second simplest two-electron chemical bond (after the hydrogen molecule), has been intensively investigated; it has a strong ionic–covalent mixing and a prominent ionic–covalent curve crossing.[94-99] In the following, we illustrate

the block-localization procedure to form the DAC states by considering the four lowest $^1\Sigma^+$ states of LiH, which we describe by MSDFT. LiH is chosen because this simple system provides a challenging case for treating avoided state crossings, spanning a coordinate range from the bonding region to more than 10 Å in interatomic separation, and the states of LiH have been extensively studied both experimentally[96, 100] and theoretically so they provide a good case for validation of the present method.[94-96, 98, 99]

The method is explained in sections 2.2 and 2.3. In section 2.4, we compare the computed energetic and geometric results for the adiabatic states with experiments and computational results from accurate wave function theory. This provides a validation of the adequacy of the DAC states as a basis and of the computational accuracy of the MSDFT method. Then we discuss the difference between non-orthogonal and orthogonal diabatic states and some consequences of varying orthogonalization procedures. Differences and similarities are found in the diabatic states obtained by MSDFT[19, 26, 53] and by previous diabatizations.[50, 75, 76]

2.2. Methods

The MSDFT method[19, 53] belongs to the "dynamic-then-static" (DTS) scenario described by Liu for treating electron correlation.[20, 22] There are two computational steps in the DTS approach: (1) the construction and optimization of a set of active states, in which dynamic correlation is first incorporated, and (2) the diagonalization of the configuration interaction (CI) Hamiltonian to include static correlation and to yield the adiabatic ground- and excited-state energies. In the present discussion, it is illustrative to

further divide the first step into three stages. (a) We first construct and variationally optimize a set of N_p Slater determinants formed from block-localized orbitals (see below). (b) Then, the determinants are combined to yield N_p spin-adapted CSFs $\{|\Psi_A>; A=1,\cdots,N_b\}$. (c) Finally, the CI matrices of CSFs of the same symmetry are diagonalized, resulting in a set of variational diabatic configuration (VDC) states.[36] The state functions in either stage b or stage c, which span the same space and therefore yield identical adiabatic states when diagonalized, constitute what we call a primary space or the active space, and they are used to perform configuration interaction calculations in step 2. The calculations of stage a are labeled block-localized Kohn-Sham density functional theory (BL-KS-DFT or, for short, BLKS). The calculations in all other steps or stages are labeled as multi-state density functional theory (MSDFT).

The active states may be regarded as contracted functions from a larger configuration interaction wave function. The dynamic then static scenario is carried out by MSDFT, in which the dynamic correlation in the contracted functions is described by an extension of KS-DFT using the determinants that define the individually localized states in the active space.[19, 26, 53] In this section, we first illustrate the method to construct the diabatic states to form the active space, making use of the four lowest singlet states of LiH as an example. Then, we describe the procedure to determine the effective Hamiltonian in MSDFT.

2.2.1. Step 1(a): Block-localized Kohn-Sham Density Functional Theory

Although delocalized Kohn-Sham orbitals can be used to construct the determinantal functions of step 1 that form a basis for the CSFs of step 1(b), in the present context where our goal is to define diabatic states, it is more convenient to use localized VB configurations.[24, 25, 36, 91] The VB description of Lewis structures is particularly illustrative to understand the asymptotic limits of diabatic states in this work, but one can certainly use the delocalized molecular orbital (MO) picture, as in standard MCSCF approaches, to define spin-adapted configurations.

For an *n*-electron molecule, the atomic orbital basis functions and electrons of the system are partitioned into M_A blocks, also called fragments, according to the Lewis structure of state *A*. Let n_b and μ_b denote respectively the number of electrons and basis functions in fragment block *b* (where $n_1 + \cdots + n_{M_A} = n$). We use block-localized Kohn-Sham (BLKS) orbitals;[19] these are linear combinations of the atomic orbital basis functions restricted to a given block. The determinant function for configuration *A* is

$$|\Psi_A> = N_A \hat{A}\{\varphi_1^A \cdots \varphi_{M_A}^A\} \tag{2.2.1}$$

where $\hat{A}$ is the antisymmetrizer, N_A is a normalization factor, and φ_m^A specifies a product of the BLKS orbitals of block *m*.[24, 25]

2.2.2. Step 1(b): Construction of CSFs.

The qualitative VB description of LiH has been lucidly presented by Mo et al.,[84] and their presentation is consistent with findings of the present study. Here, the atomic

basis functions are conveniently divided into five blocks, one set of four blocks (the core, 2*s*, 2*pσ*, and 3*s*/3*pσ*) on Li and one block (1*s*) on H. Spin-adapted CSFs are constructed by combining several determinants to represent the corresponding covalent and ionic states. Specifically, for LiH, the minimum diabatic representation of the four low-lying $^1\Sigma^+$ adiabatic states, labeled here (as usual) as the X, A, C, and D states in order of

increasing energy, includes seven CSFs, consisting of twelve determinants. They correspond to the ionic and covalent (2*s*) states, and the 2*pσ*, 3*s,* and 3*pσ* excited states of the Li atom:

$$|\Psi_{2s}[(\mathrm{Li}^{\bullet})(\mathrm{H}^{\bullet})]> = N_{2s}[\hat{A}\{\phi_c^2\bar{\phi}_{2s}^1\phi_{1s}^1\} - \hat{A}\{\phi_c^2\phi_{2s}^1\bar{\phi}_{1s}^1\}] \quad (2.2.2.a)$$

$$|\Psi_{\mathrm{ion}}[(\mathrm{Li}^{+})(\mathrm{H}^{-})]> = N_{\mathrm{ion}}\hat{A}\{j_c^2 j_{1s}^2\} \quad (2.2.2.b)$$

$$|\Psi_{-}[(\mathrm{Li}^{-})(\mathrm{H}^{+})]> = N_{+}\hat{A}\{\phi_c^2\phi_{2s}^2\} \quad (2.2.2.c)$$

$$|\Psi_{2p}[(\mathrm{Li}^{\bullet})(\mathrm{H}^{\bullet})]> = N_{\mathrm{cov}}[\hat{A}\{\phi_c^2\bar{\phi}_{2p}^1\phi_{1s}^1\} - \hat{A}\{\phi_c^2\phi_{2p}^1\bar{\phi}_{1s}^1\}] \quad (2.2.2.d)$$

$$|\Psi_{3s}[(\mathrm{Li}^{\bullet})(\mathrm{H}^{\bullet})]> = N_{3s}[\hat{A}\{\phi_c^2\bar{\phi}_{3s}^1\phi_{1s}^1\} - \hat{A}\{\phi_c^2\phi_{3s}^1\bar{\phi}_{1s}^1\}] \quad (2.2.2.e)$$

$$|\Psi_{3p}[(\mathrm{Li}^{\bullet})(\mathrm{H}^{\bullet})]> = N_{\mathrm{cov}}[\hat{A}\{\phi_c^2\bar{\phi}_{3p}^1\phi_{1s}^1\} - \hat{A}\{\phi_c^2\phi_{3p}^1\bar{\phi}_{1s}^1\}] \quad (2.2.2.f)$$

$$|\Psi_{2s/2s}[(\mathrm{Li}^{\bullet})(\mathrm{H}^{\bullet})]> = N_{2s/2s}[\hat{A}\{\phi_c^2\bar{\phi}_{2s}^1\phi_{\mathrm{H}2s}^1\} - \hat{A}\{\phi_c^2\phi_{2s}^1\bar{\phi}_{\mathrm{H}2s}^1\}] \quad (2.2.2.g)$$

where j_c, j_{2s}, j_{2p}, j_{3s}, and j_{3p} are the core (1*s*), valence (2*s* and 2*pσ*), and Rydberg-type (3*s* and 3*pσ*) BLKS orbitals located on lithium, ϕ_{1s} and ϕ_{H2s} are basis orbitals on the hydrogen atom, and ϕ^1 and $\bar{\phi}^1$ respectively indicate single occupation by an electron with respectively α or β spin. Equation 2.2.2 defines singlet states that are eigenfunctions of both the $\hat{S}^2$ and $\hat{S}_z$ operators, and triplet states can be analogously represented, but for brevity they are not explicitly shown here.

The ionic configuration $|\Psi_{-}[(Li^-)(H^+)]>$ slightly affects the adiabatic state energies by about 1 kcal/mol (~0.04 eV), but otherwise it does not make significant contributions to bonding. In addition, the 3*s*-2*s* bonding interaction between lithium and hydrogen (ϕ_{H2s}) is much higher in energy and makes negligible contributions to the low-lying adiabatic states. They are included in test calculations and kept to obtain the adiabatic energies, but we will not further discuss these two states ($|\Psi_{-}[(Li^-)(H^+)]>$ and $|\Psi_{2s/2s}[(Li^\bullet)(H^\bullet)]>$).

2.2.3. Step 1(c): Configuration interaction.

In step 1(a), the BLKS determinants were independently optimized as in standard KS-DFT, except that the electron densities are obtained using non-orthogonal orbitals.[19] In step 1(b), the singlet (and analogously triplet) CSFs, as given by equations 2.2.2.a, and 2.2.2.d-g, were obtained by diagonalizing the corresponding spin-coupled Hamiltonian matrix. These CSFs are not necessarily the diabatic ground and excited states. In step

1(c), to obtain diabatic excited states, the CI matrices of CSFs of the same symmetry, *e.g.*, 2s and 3s, and 2pσ and 3pσ, are diagonalized, resulting in a set of variational diabatic configuration (VDC) states.[36] The VDC states are also called valence-bond diabatic states, and they are compared in section 2.4.2 to the diabatic states obtained by the threefold way from SA(4)-CASSCF and XMC-QDPT calculations as previously reported in references 50 and 75.

Throughout this article, we use the indices A, B, … to specify the basis configurations from any one of the three stages, and I, J, … to indicate adiabatic states.

We note that the choice of fragmental blocks is "natural" and chemically intuitive for bond forming and breaking processes. Thus, the VB-picture is used in this work. For small and medium (~100 atoms) sized molecules, conjugated or not, one can use delocalized orbitals to define configuration space as in MCSCF approaches. For large systems, fragmentation can reduce computational costs. However, for large and extensively conjugated systems (such as graphene), there is probably no simple way to have both efficiency and accuracy both for the ground and excited states. To this end, it is of interest to compare the basis states defined by equation 2.2.2 with the spin-coupled valence bond (SCVB) method[34, 35]. In SCVB, delocalized single-electron orbitals are used among which all spin-coupled configurations are included. In MSDFT, orbitals are block localized and spin coupling is taken into account only between blocks critical for bonding interactions (*e.g.*, the electron pair involved in the dissociation of a single bond). A single block-localized determinant (BLKS determinant) is employed to approximate the SCVB function for the entire block, greatly reducing the number of configurations in the active

space. Importantly, dynamic correlation is incorporated in the reference functions in MSDFT, whereas it is treated as a post-SCF correction in SCVB.[34, 35]

2.2.4. Step 2: Multistate Density Functional Theory:

The adiabatic ground and excited state energies in the DTS scenario are obtained, in the second (final) step of the method, by configuration interaction among the basis states defined and optimized in the active space.[19, 53] In particular, the diagonal matrix elements of the effective Hamiltonian are simply the KS-DFT energies for the corresponding states $\{|\Psi_A>; A=1,\cdots,N_p\}$.[19] In the present case of LiH, N_p is 7, as constructed from 12 BLKS determinants. It is convenient to first consider the determinant representation to describe the matrix elements as follows:[19]

$$H_{AA}(\mathbf{R}) = E^{\mathrm{KS}}[\rho_A^{\mathrm{ms}}(\mathbf{r};\mathbf{R})] \qquad (2.2.3.a)$$

where $\rho_A^{\mathrm{ms}}(\mathbf{r};\mathbf{R})$ is the electron density of configuration *A*, determined from the orbitals that form the determinant $|\Psi_A(\mathbf{r};\mathbf{R})>$. We note that any standard exchange-correlation functional $E_{xc}^{\mathrm{KS}}[\rho_A^{\mathrm{ms}}(\mathbf{r})]$ can be used to obtain $E^{\mathrm{KS}}[\rho_A^{\mathrm{ms}}(\mathbf{r})]$. In the CSF basis, the matrix elements can be conveniently obtained using the transformation matrix defined by equations 2.2.2.a-g:

$$H_{BB}(\mathbf{R}) = 2N_A^2\{H_{AA}(\mathbf{R}) - H_{A\bar{A}}(\mathbf{R})\} \qquad (2.2.3.b)$$

where B specifies a spin-adapted CSF, and A and $\bar{A}$ specify determinants with spin exchanges in equation 2.2.2. Note that $H_{AA} = H_{\bar{A}\bar{A}}$, and $H_{A\bar{A}}(\mathbf{R}) = H_{\bar{A}A}^{*}(\mathbf{R})$ defined

below. If the VDC states are used, a similar transformation will be used with the corresponding transformation matrix.

The off-diagonal matrix elements could in principle be determined by WFT.[23-25] This would involve the transition density $\rho_{AB}(\mathbf{r}) = < \Psi_A \mid \hat{\rho}(\mathbf{r}) \mid \Psi_B >$. However, a transition density functional (TDF)[53] $E^{\mathrm{TDF}}[\rho_{AB}(\mathbf{r})]$ between states $\mid \Psi_A >$ and $\mid \Psi_B >$ does not exist within the KS-DFT framework. $E^{\mathrm{TDF}}[\rho_{AB}(\mathbf{r})]$ might be derived by multiconfigurational approaches[53] and by analogy to methods[101] used for electron scattering. Here though, we approximate it in MSDFT by two contributions:

$$H_{AB} \equiv E^{\mathrm{TDF}}[\rho_{AB}(\mathbf{r})] = < \Psi_A \mid H \mid \Psi_B > + V_c^{\mathrm{TDF}}[\rho_{AB}(\mathbf{r})] \qquad (2.2.4)$$

where H is the electronic Hamiltonian. The first term in equation 2.2.4 is the electronic coupling between the non-orthogonal wave functions, and it is evaluated as an integral between non-orthogonal determinants, which has been used in the MOVB approach.[24, 25]. The second term in equation 2.2.4 is a transition density contribution.[19, 24-26, 53, 92] Note that both exchange and static correlation are included in the first term, whereas only dynamic correlation is in the second term.[53] We then approximated the second term of equation 2.2.4 by an overlap-weighted average of the KS correlation energies for the two interacting states:[19, 26]

$$V_c^{\mathrm{TDF}}[\rho_{AB}(\mathbf{r})] \approx \frac{\lambda}{2} S_{AB} (E_c^{\mathrm{KS}}[\rho_A^{\mathrm{ms}}(\mathbf{r})] + E_c^{\mathrm{KS}}[\rho_B^{\mathrm{ms}}(\mathbf{r})]) \qquad (2.2.5)$$

where λ is unity in the present work (in later work this parameter or functional could be optimized to fit experimental results), where S_{AB} is the overlap integral $< \Psi_A \mid \Psi_B >$,

and where E_c^{KS} specifies the correlation energy in the corresponding diagonal matrix element (as obtained from the exchange-correlation functional).[1]

The adiabatic ground and excited states are obtained as the eigenvalues $\{E_I\}$ and eigenvectors $\mathbf{C}_I = \{C_{AI}\}$ of the generalized secular equation:

$$\mathbf{HC} = E\mathbf{SC} \tag{2.2.6}$$

where E is a diagonal matrix of the adiabatic energies, and $\mathbf{S}$ and $\mathbf{C}$ are the overlap matrix and configuration coefficient matrix. The BLKS determinants in equation 2.2.2 are used to determine the overlap matrix, and the computational procedure is identical to that used in MOVB.[24, 25] The densities and energies for the adiabatic states are then given by

$$\rho_I(\mathbf{r}) = \sum_{A=1}^{N_p} \{C_{AI}^2 \rho_A^{\mathrm{ms}}(\mathbf{r}) + \sum_{B \neq A} C_{AI} C_{BI} \rho_{AB}(\mathbf{r})\} \tag{2.2.7}$$

$$E_I^{\mathrm{MS}}[\rho_I(\mathbf{r})] = \sum_{A=1}^{N_p} \{C_A^2 E^{\mathrm{KS}}[\rho_A^{\mathrm{ms}}(\mathbf{r})] + \sum_{B \neq A} C_{AI} C_{BI} E^{\mathrm{TDF}}[\rho_{AB}(\mathbf{r})]\} \tag{2.2.8}$$

Equations 2.2.7 and 2.2.8 shows that both the ground state ($I = 0$) and excited states ($0 < I < N_p$) are treated on the same footing. Consequently, the method provides energies for all states described by the basis configurations in the active space, and, unlike linear-response TDDFT, the CI matrix has the correct structure to properly describe all conical intersections (even those involving the ground state) and to treat weakly (and strongly) avoided crossings for nonadiabatic processes.[19, 53] Equations 2.2.7 and 2.2.8 represent a hybrid wave function and density functional theory that goes

beyond the Kohn-Sham approximation of DFT from a single determinant for the ground-state density to a multi-determinant representation of ground and excited states. It would be interesting to compare MSDFT[19, 53] to multi-configuration pair-density functional theory,[102] but that is beyond the scope of this article.

2.3. Computational Details

In the present study, we consider the four low-lying $^1\Sigma^+$ states of LiH, which are modeled by the active space defined by equation 2.2.2. At interatomic separations near to and shorter than the ground-state minimum, contributions from higher states play an important role in the various adiabatic states, especially for the second and third excited states, S_2 (C) and S_3 (D), making their detailed behavior even more interesting and complex. The present six (actually seven if the relatively unimportant 2*s*(H) is counted) CSFs are sufficient for illustrating the complicated electronic couplings in LiH.

The atomic orbital bases are approximated using the aug-cc-pVTZ basis set.[103] For Li, the basis set is further divided into four blocks,: (1) the 1*s*-core and 2*s* valence orbitals, (2) the $2p_\sigma$ orbitals with σ symmetry along the bond axis direction as well as *d*-orbitals of the same symmetry, and (3) and (4) the 3*s* and 3*p* orbitals representing Rydberg states. All remaining orbitals are grouped into the first block for convenience (a fifth block could be used, but they make no contribution to the bonding energy due to orthogonal symmetry). For the 3*s* orbital, the standard diffuse function is replaced by the diffuse basis function in the Dunning-Hay basis set[104] (this gives a slightly better energy for the 3*s* state of Li atom from MSDFT calculations), whereas the 3*p* basis functions are

given by the diffuse p functions in the aug-cc-pVTZ basis. Similarly, the aug-cc-pVTZ basis is either used directly for the hydrogen atom, or it separated into two blocks with the diffuse *s* orbital to represent its Rydberg state. Unless special emphasis is needed, in the remainder of the article, we simply use the standard expression of aug-cc-pVTZ, rather than employing a different notation to represent the small difference in the diffuse basis for lithium. We have not attempted to optimize basis functions specifically to model Rydberg states since this is not the main purpose here; the unoptimized nature of the basis will introduce errors for the upper states. The excitation energies for the 2*p* ($^2\mathrm{P}^o$) 3*s* ($^2\mathrm{S}$), and 3*p* ($^2\mathrm{P}^o$) states of Li atom are 1.650, 3.493, and 3.822 eV from MSDFT compared with the experimental values of 1.848, 3.373, and 3.834 eV.[105] Thus, there is an error of about 0.2 eV in the atomic spectra; this kind of error (due to basis set used) will be transferred to the molecular description.

The configurations defined in equation 2.2.2 are built from determinants that are variationally optimized using the hybrid PBE0 density functional;[106, 107] the computational algorithm has been described previously.[19] Either the CSF states[36] or the VDC states are subsequently used to solve equation 2.2.6, and they yield the same adiabatic ground and excited state energies, but the latter basis can be used in analysis of the DAC states. In principle, the BLKS orbital coefficients and configuration coefficients can be simultaneously optimized as in standard ground-state MCSCF methods, resulting in a set of consistently optimized diabatic configurations (CDC states).[36, 86] Although the use of CDC states optimized for the ground states can lower the adiabatic ground-state energy, to obtain diabatic excited states useful for bonding analysis it would be preferable

to use state-averaged optimization. Since the CDC diabatic states are not variationally optimized, they are not particularly useful for analysis and for understanding of bonding interactions (for example, resonance energy). Thus, we do not further pursue the CDC states in this study.

The computational results are dependent on the functional used since MSDFT relies on a single-determinant functional for the configurational state. Given a functional used, it defines the condition for the transition density functional (TDF). Therefore, the relative (and absolute) energies of the diabatic (basis) configurations are fully defined by the specific functional used. We have found that the PBE and PBE0 functionals perform well with the MSDFT method, especially for charge transfer processes.[26, 108]

SA-CASSCF[77] and MS-CASPT2[78] calculations are also performed using the standard aug-cc-pVTZ basis set for comparison. Four states are used in the state-average optimization with equal weights, and they are also treated in the multistate perturbation calculation. The *Molpro* program is used for these WFT calculations,[109] while MSDFT is carried out using a locally modified version of the GAMESS program.[110] All computations are performed on computer clusters in our laboratory at Jilin University and at the Minnesota Supercomputing Institute.

2.4. Results and Discussion

The ground state of LiH is known to be dominated by the ionic configuration, $|\Psi_{ion}[(Li^+)(H^-)]>$, whereas the dissociation limit of the ground state consists of two neutral atomic radicals corresponds to the covalent configuration

$|\Psi_{2s}[(Li^{\bullet})(H^{\bullet})]>$. At short interatomic distances, the excited states are characterized by strong interactions involving several high-lying states, giving rise to further complications. The potential energy curves for the four singlet adiabatic states from MSDFT are shown in Figure 2.1, along with the MS-CASPT2 results for comparison, and those for the four lowest triplet states are displayed in Figure 2.2. The main purpose of this section is to show that the present MSDFT method can provide a reasonably quantitative description of the system ($\leq$ 0.3 eV), and that it can be used to provide insight into the diabatic representation of the potential energy curves.

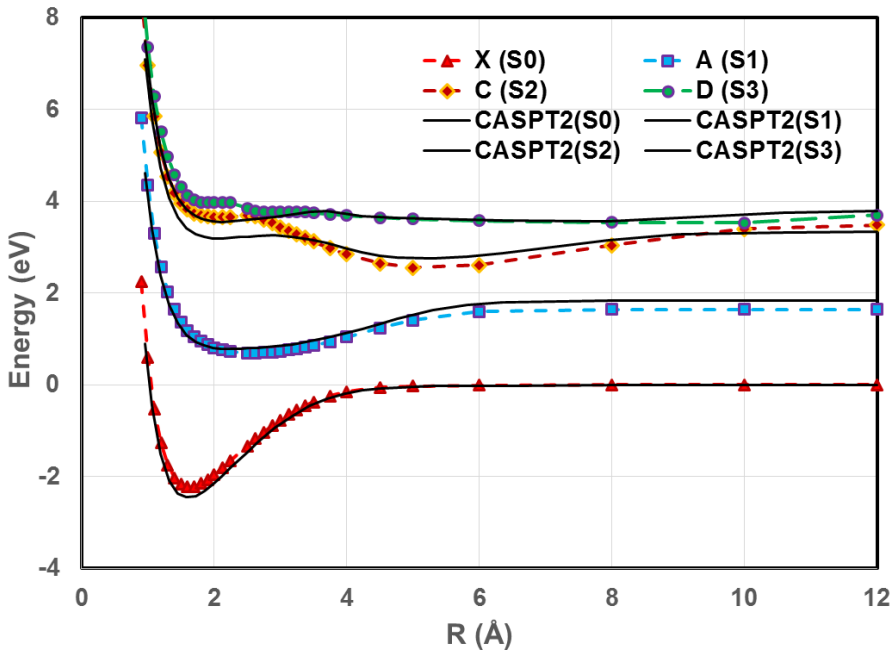

Figure 2.1. Adiabatic potential energy curves for the four lowest $^1\Sigma^+$ states of LiH as functions of interatomic distance from MSDFT (dashed curves) using the PBE0 density functional and from MS-CASPT2//SA(4)-CASSCF(2,9) calculations (solid curves). The aug-cc-pVTZ basis set with the diffuse *s*-function replaced by that of the Dunning-Hay basis (simply denoted by aug-cc-pVTZ throughout) is used in all MSDFT computations, whereas the standard aug-cc-pVTZ basis is used in wave function methods.

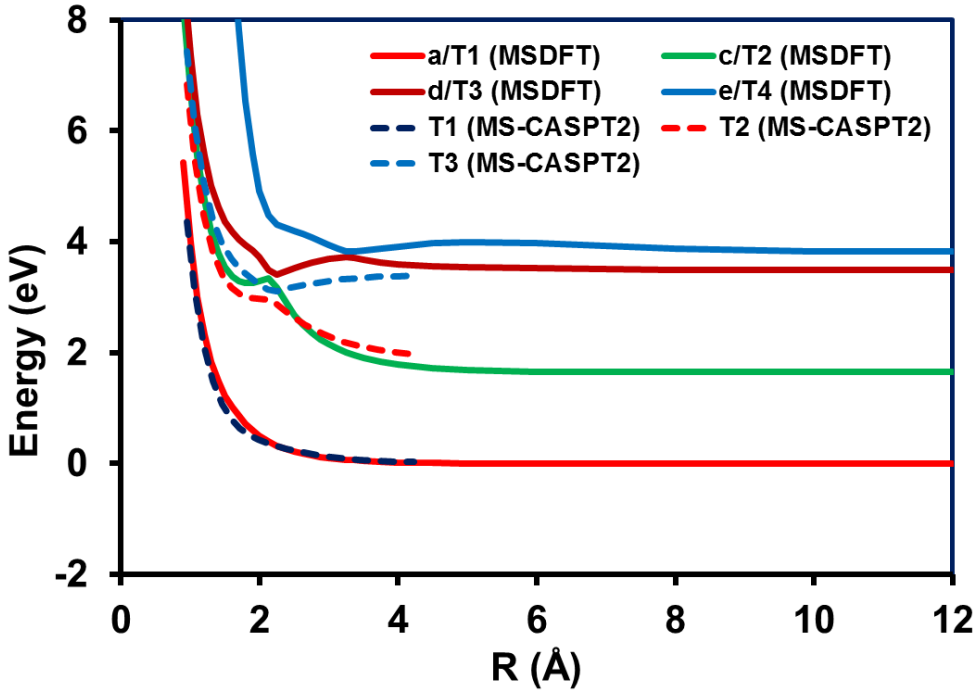

Figure 2.2. Adiabatic potential energy curves for the four lowest $^3\Sigma^+$ triplet states of LiH (**a**, **c**, **d**, and **e** in order of increasing energy) as functions of interatomic distance from MSDFT (solid curves) using the PBE0 density functional, and from MS-CASPT2/SA(4)-CASSCF (dashed curves). The aug-cc-pVTZ basis set is used in all computations (see caption of Figure 2.1).

2.4.1. Adiabatic Potential Energy Surfaces

We compare the MSDFT potential energy curves to MS-CASPT2 results; both the qualitative trends and quantitative results from MS-CASPT2 calculations agree well with more complete or more accurate studies.[94-96, 98-100] The present MSDFT method does not involve the high cost of a SA-CASSCF computation, but it includes all dynamic correlation at the stage of diabatic (basis) state construction, yielding results comparable or better than the more expensive MS-CASPT2 calculation. Furthermore, the number of configurations in the active space is smaller in the present method (12 determinants vs.

45 in the (2,9)-CAS) an advantage of the DTS scenario. There is also no complication in MSDFT due to intruder states.

Table 2.1 summarizes the energies and the corresponding bond distances at the critical points on these potential energy curves. Note that computations are performed using grids with 0.1 to 2 Å intervals (depending on the region), which bracket the precisions of bond distances at the critical points. The global minimum of LiH from MSDFT has a bond length of 1.6 Å with a bond dissociation energy of 2.22 eV, in reasonable agreement with the experimental results (1.596 Å and 2.515 eV)[100] and MS-CASPT2 data (1.588 Å and 2.449 eV) as well as MRCI results (Table 2.1).[94, 96] The small discrepancy (0.3 eV) in bond energy is primarily due to basis set effects in the MSDFT calculation; the deviation is reduced by 0.1 eV if we switch to the aug-cc-pVQZ basis set. Another key energetic quantity is the bond energy relative to the ionic dissociation limit (7.18 eV); this also agrees well with the experimental value (7.15 eV).[100]

Turning to the excited states, we find that the potential energy curves determined using MSDFT are generally in good agreement with those from MS-CASPT2 as well with those from MRCI studies,[94, 96] except for states C and D at short bond distances, where the MSDFT energies are about 0.4 eV higher than the MS-CASPT2 values. This difference may be due to limitations in the basis set used to approximate the Rydberg states or to interactions involving high-energy states that are not included in the VB-localized picture. Overall, the computed vertical and adiabatic transition energies to the A, C, and D states agree well with MS-CASPT2 results, typically within 0.2 eV for the former and within 0.3 eV for the latter. The experimental excitation energy for the A state

is 3.29 eV, which lies between the computed vertical and adiabatic excitation energies (Table 2.1).[96, 100, 111]

The MSDFT calculations correctly yield a stretched bond for the first excited state. It has an equilibrium distance of near 2.5 Å; this may be compared with the experimental value of 2.596 Å,[100] and a somewhat shorter bond distance (2.25 Å) from MS-CASPT2 (Table 2.1). The bond energy for the A state is estimated to be 0.95 eV from MSDFT, as compared to 1.08 and 1.05 eV from MS-CASPT2 and experiment.[96, 100] The C state consists of two energy minima roughly at 2.125 and 5.0 Å on the MSDFT potential energy curves, and the corresponding equilibrium distances are 2.117 and 5.292 Å at the MS-CASPT2 level. The bond energies are 0.6 to 0.9 eV at the longer separation. The inner minimum is produced through interactions involving several states (Figure 2.1), with primary contributions from the 3*s*(Li) and 3*p*(Li) states. Among theoretical studies, comprehensive investigations of the LiH molecule up to the 4*p* state are given in references 95, 96, 99, and the specific features and locations of all avoided crossings found in Figure 2.1 mirror those reported in earlier work very well. Overall, the agreement in qualitative trends of the potential energy curves and in quantitative energies and geometries between MSDFT and MS-CASPT2 along with experimental data shows that the present MSDFT approach can provide a good description of the ground and excited states for LiH.

Table 2.1. Bond energies (D_e) and adiabatic excitation energies (T_e) in eV, and geometries in Å for the ground (*X*) and the first three excited states (denoted as *A*, *C*, and *D*) of LiH. The aug-cc-pVTZ basis set is used in all calculations using the multistate density functional theory (MSDFT) and complete-active-space second-order perturbation theory (MS-CASPT2). The PBE0 density functional is used in MSDFT; the (2,9) active space is employed for MS-CASPT2.

Property[a]	MSDFT	MS-CASPT2	MRCI[94]	Expt.[57, 100]
		$S_0, X^1\Sigma^+$		
R_e	1.6	1.588	1.589	1.595
D_e	2.223	2.449	2.522	2.515
$LiH \rightarrow Li^+ + H^-$	7.180			7.151
		$S_1(2p), A^1\Sigma^+$		
R_e	2.5	2.249	2.577	2.596
D_e	0.95	1.05	1.077	1.076
T_e	2.92	3.24	3.29	3.288
T_{vert}[b]	3.40			
		$S_2(3s), C^1\Sigma^+$		
R_e(in)	2.125	2.117	2.023	2.02[111]
R_e(o)	5.0	5.29	5.384	5.37[111]
$R^{\ddagger}$	2.5	2.91		
$\Delta E^{\neq}_{diss}$[c]	0.12	0.06		
D_e(in)	-0.17	0.14	0.16	
D_e(o)	0.95	1.08	1.15	1.05[111]
T_e(in)	5.88	5.65	5.74	
T_e(o)	4.78	5.21	4.85	4.83[57]
		$S_3(3p), D^1\Sigma^+$		
R_e(in)	1.9, 2.75	2.1	2.8[57]	
R_e(o)	10	7.9	10.5[57]	
D_e(in)	0.06	0.25	0.33[57]	
D_e(o)	0.29	0.24	0.33[57]	
T_e(in)	6.0	6.2	5.9[57]	
T_e(o)	5.7		5.9[57]	

[a] (*in*) and (*o*) specify the inner energy minimum and outer energy minimum, respectively.
[b] Vertical excitation energy at ground-state equilibrium geometry.

[c] $\Delta E_{diss}^{\neq}$ denotes the barrier higher for dissociation (in eV)

The triplet states of LiH have also been studied computationally, although there appears to have little information available from experiment. Representative reports can be found in references 95, 96; the weakly avoided crossing between the c (T2) and d (T3) adiabatic states at about 2.1 Å in Figure 2.2 is clearly shown in the earlier studies. The e (T4) state in Figure 2.2 has a sharper increase in energy at short distance than that obtained in previous studies;[95, 96] this suggests that orbital hybridization may be required and basis set limitations may need to be overcome for describing these high-lying Rydberg states.

2.4.2. Valence-Bond Diabatic States

The potential energy curves for five of the seven VB basis states are shown in Figure 2.3, excluding the high-energy Li(2*s*)H(2*s*) covalent configuration and the reverse ionic state (Li^-)(H^+) since they make relatively minimal contributions to bonding interactions. These are the block-localized, nonorthogonal VDC states with the upper (Rydberg) states orthogonalized to the low-energy electronic CSFs (equations 2.2.2) of the same symmetry. These VB diabatic states approach the dissociation limits of the corresponding adiabatic states by construction. Significantly, the valence characters defined in equations 2.2.2 are kept at all geometries.

A most striking observation of Figure 2.3 is that the ionic state spans the entire relevant energy range, from being the lowest energy diabatic state at the global minimum to becoming the highest energy state at the dissociation limit. The ionic diabatic state

crosses at distances about 2.5, 4.2, 10, and >12 Å, respectively, with the 2*s*, 2p_σ, 3*s*, and 3$p\sigma$ covalent states of lithium that have been considered. These diabatic crossings also create some of the most intriguing strong non-adiabatic couplings among the adiabatic potential energy curves. For instance, the 2*s* state indeed transforms smoothly to the adiabatic ground state, X(S_0), at the dissociation limit, but the non-orthogonal "pure" atomic covalent state does not start nor approach the first adiabatic excited state, A(S_1), at short bond distances. In fact, none of the VB-diabatic states alone can provide an adequate description of the adiabatic surfaces at short bond lengths, except the accidental superposition between the D(S_3) adiabatic state and the 3*p*-diabatic state (see below). The adiabatic states are typically mixtures of at least three major VB states in the present case. This is shown by the adiabatic ground state as an admixture of the dominant Li^+H^- ionic state with the bonding combination of the 2*sp*σ hybrid of Li and the 1*s* orbital of hydrogen. The first excited state includes the antibonding combination of the 2*s* and 2*p*σ orbtials of Li with $1s_H$. The loosely bound minimum at about 5 Å on the C(S_2) state can be attributed to the strong Coulomb attraction in the ionic VB state.

Note that the 3*s* and 3*p*σ VB-diabatic states displayed in Figure 2.3 are not the variationally optimized energies from the functions defined by equations 2.2.2.e and 2.2.2.f, which are non-orthogonal to the lower states of same symmetry. Their energies in Figure 2.3 are obtained by configuration interaction involving states with the same symmetry. Consequently, some upper states exhibit effects of coupling, *e.g.*, on the 3*s* surface (solid-red curve). It is interesting to note that the lithium 2*s*-3*s* configuration interaction has little effects on the energy of the 2*s* valence state, but the overlap-induced

increase in energy of the variationally optimized 3*s* state is more profound (resulting in the solid-red curve).

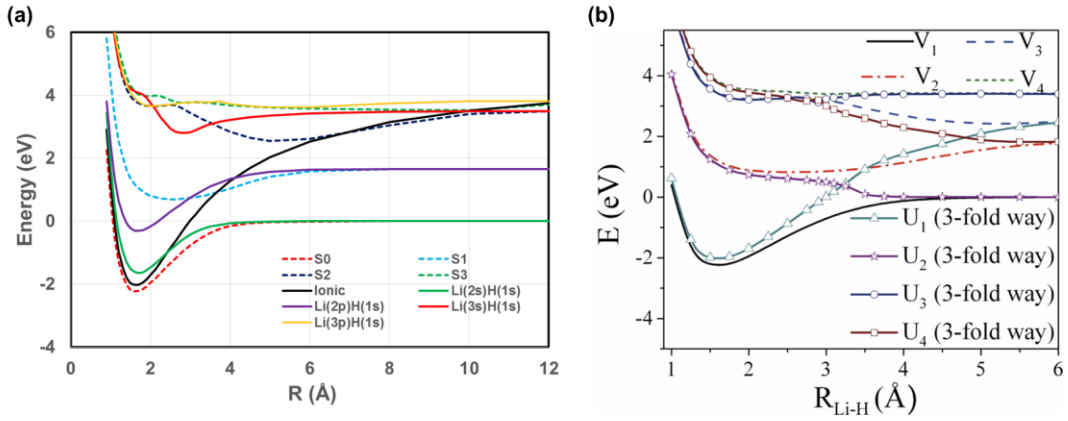

Figure 2.3. (**a**) Valence-bond diabatic (solid curves) and adiabatic (dashed curves) potential energy curves of LiH as a function of interatomic separation optimized by multistate density functional theory (MSDFT). The PBE0 density functional along with the aug-cc-pVTZ basis set (see Figure 2.1) are used in all calculations. (**b**) Diabatic potential energy curves obtained by the Three-Fold-Way diabatization approach. Adapted from Figure 2.5 of reference 75 with permission by the American Institute of Physics.

2.4.3. Orthogonal Diabatic States

The diabatic states are typically expressed as orthogonal states,[86, 112] and in this section we discuss the orthogonalized diabatic states. An example of the diabatic representation of the potential energy curves for LiH from the threefold way diabatization method is reproduced in Figure 2.3.b. Orthogonality makes the expression and computation of nonadiabatic dynamics simpler, but in the DAC approach, diabatic state functions are variationally optimized and only states of the same symmetry are orthogonal by configuration interaction; in general, the full VDC basis states are non-orthogonal. Although the adiabatic potential energy curves are similar in Figure 2.3, the

qualitative trends of the non-orthogonal diabatic states from the DAC approach (Figure 2.3.a) and the orthogonal ones (Figure 2.3.b) from the ATD transformation have very different appearances, except the ionic state. One can orthogonalize the VB-diabatic configurations by similarity transformation so that they can be directly used in nonadiabatic dynamics simulations. Is it possible to reproduce similar qualitative features as that expressed in the orthogonal diabatic states in Figure 2.3.b, starting from the non-orthogonal VB states in Figure 2.3.a? If so, what are the main quantitative differences? These are the questions to be addressed in this section.

Unfortunately, orthogonal transformation is not unique from the set of well-defined VB-diabatic states[112].[56] Here, we examine several orthogonal transformation procedures and compare the results with the well-tested threefold-way diabatization approach. One seemingly appealing approach is the Löwdin transformation using $(\mathbf{S})^{-1/2}$, where $\mathbf{S}$ is the overlap matrix of the VB-diabatic states, which transforms the original vectors into orthogonal ones in a least-square sense by mixing all configurations. This turns out not to be a good choice since the potential energy curves of the resulting states are severely distorted such that they resemble neither the original diabatic states nor the adiabatic ones (not shown here, but see reference 86 for another system).

The Gram-Schmidt (GS) orthogonalization method can maximally preserve the characters of each individual state sequentially; here, we follow the order of increasing energy – ionic, 2*s*, 2*p*, 3*s*, 3*p*, the "reverse ionic", and the H-2*s* diabatic states – to describe the four lowest $^1\Sigma^+$ states of LiH. A set of four different GS transformations of the VB-diabatic states into orthogonal ones, all of which yield the same adiabatic

potential energy curves, are shown in Figure 2.4. They differ in the way of mixing some basis CSFs prior to the GS transformation:

(a) direct GS orthogonalization;

(b) an equal mixture of 2*s* and 2*p* states of Li,

$\Psi'_{2s} = N_b(\Psi_{2s} + \Psi_{2p})$ and $\Psi'_{2p} = N_b(\Psi_{2p} - \Psi_{2s})$

where N_b is a normalization factor;

(c) the same *sp*-mixing as in (b) scaled by the overlap integral,

$\Psi'_{2s} = N_c(\Psi_{2s} + S_{2s2p}\Psi_{2p})$ and $\Psi'_{2p} = N'_c(\Psi_{2p} - S_{2s2p}\Psi_{2s})$;

(d) the inclusion of a small amount (25%) of the 2*s*-covalent state (also overlap-dependent) in the ionic configuration

$\Psi'_{2s} = N_c(\Psi_{2s} + S_{2s2p}\Psi_{2p})$, $\Psi'_{2p} = N'_c(\Psi_{2p} - S_{2s2p}\Psi_{2s})$, and

$\Psi'_{\text{ion}} = N_d(\Psi_{\text{ion}} + 0.25S_{2s2p}\Psi_{2s})$.

Gram-Schmidt orthogonalization by keeping the valence character of the ionic state immediately leads to the familiar curve-crossing features between "neighboring" diabatic states to yield various avoided crossings in the adiabatic curves (Figure 2.4.a). However, the direct GS orthogonalization of the VB diabatic state vectors does not produce a diabatic state closely resembling the first excited state; the latter is formed as a result of antibonding and bonding combinations of the 2*s*(Li) and 2*p*(Li) states with hydrogen's 1*s*(H), *i.e.*, an *sp*-hybrid. A simple mixture of 2*s*(Li) and 2*p*(Li) configurations is not chemically physical, yielding both states having the same energy at the dissociation limit in Figure 2.4.b. The *sp*-hybridization takes place due to chemical bonding interactions at

short interatomic distances, which is overlap dependent. As a result, the bonding patterns seen in the threefold-way diabatization procedure are reproduced in Figures 2.4.c and 2.4.d when the 2*s*-2*p* mixing is scaled by the overlap integral; Figure 2.4.d also includes a small portion of 2*s*-covalent character in the ionic state.

Figures 2.4.c. and 2.4.d shows that the $(Li)^+(H)^-$ ionic state is dominant in the ground state near the equilibrium geometry, both in the orthogonal diabatic state representation and in the non-orthogonal VB representation in Figure 2.3.a. The ionic state smoothly transforms to its dissociation limit, crosses with all other diabatic states, and approaches the S_3 adiabatic excited state at 12 Å in the present study. The *sp*-hybrid covalent diabatic state starts from the $A(S_1)$ state at short bond lengths and ends at the ground-state dissociation limit as $Li^{\bullet}$ and $H^{\bullet}$. In the intermediate bonding region on the $A(S_1)$ curve, the ionic state is dominant, and its interactions with the 2*p*(Li)-1*s*(H) antibonding diabatic state result in an avoided crossing between the S_1 and S_2 adiabatic states as the covalent configuration decays to the 2*p* dissociation limit. The two low-lying crossings occur at about 3.125 Å and 5 Å in Figures 2.4.c and 2.4.d, are somewhat longer than those generated by the threefold-way diabatization method (2.9 and 3.7 Å), but closer to the minimum-gap positions of the corresponding avoided potential energy curves, and to values of 3.2 and 5.3 Å from a diabatization based on nonadiabatic coupling terms.[57] Importantly, all diabatic and adiabatic potential energy surfaces are smooth at all geometries.

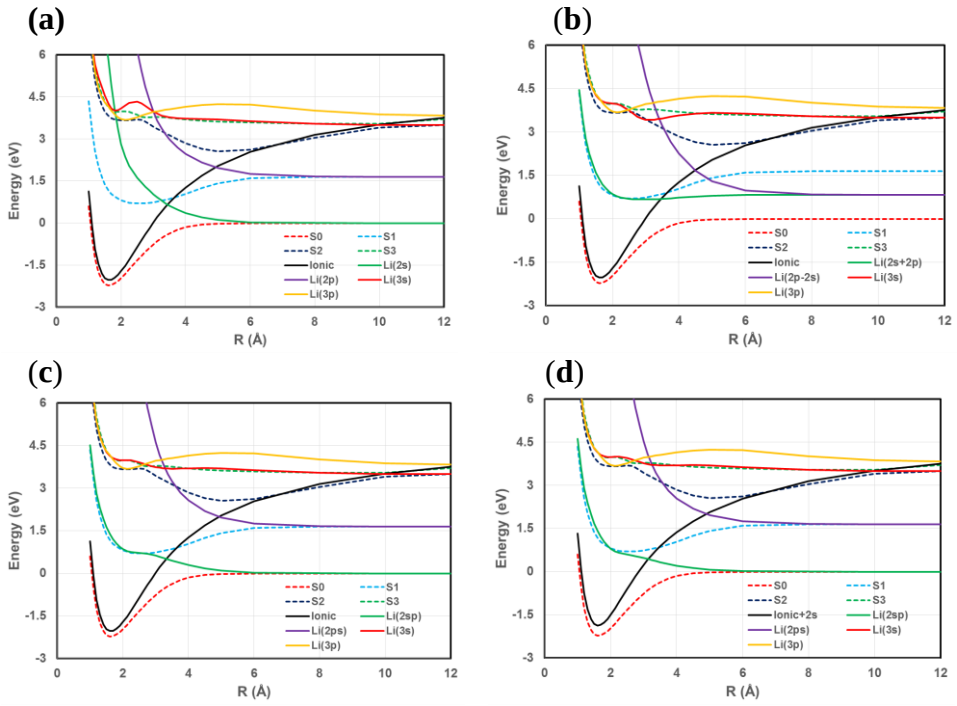

Figure 2.4. Orthogonalized diabatic (dashed curves) potential energy curves of LiH as a function of interatomic separation, transformed from the non-orthogonal VB-diabatic states in Figure 2.3(a) by (**a**) direct Gram-Schmidt (GS) orthogonalization, (**b**) GS-projection of mixed of 2*s* and 2*p* covalent states, (**c**) 2*s*-2*p* mixing scaled by the overlap integral, and (**d**) as in (c) along with a small amount of 25% 2*s* state added to the ionic state. The adiabatic potential energy curves are shown as solid curves.

The S_2 and S_3 states possesses two avoided crossings, one at an outer range near 10 Å due to the $(Li)^+(H)^-$ ionic and 3*s*(Li) interactions, and another at the inner distance of about 2.5 Å. The orthogonal diabatic states in Figure 2.4 (irrespective to the specific orthgonalization details) show that the latter crossing at short distance involves interactions primarily between the 3*s*(Li) and 3*p*(Li) states with the participation of the strongly repulsive 2*p*(Li) state and of 2*s*(H) character (not shown). These results are consistent with previous analysis of LiH excited states, and with the finding that the ionic-3*s* and 3*p* state crossings with the ionic state occur at about 10 and 18 Å.[57, 96, 97, 113]

Figure 2.4 shows that the non-orthogonal VB states can indeed be orthogonalized to yield diabatic states qualitatively similar to those from the Three-Fold-Way ATD transformation procedure, although the 2*p* diabatic state is much more repulsive and shows no particular dependence to the higher adiabatic curves. An overlap-dependent mixing of certain VB states before the diagonalization process is needed to represent orbital hybridization. Importantly, the similarity transformation procedure must maintain certain key identities (*e.g.*, the ionic valency and dissociation limits) of the original vectors. We note also that there is no issue concerning phase consistency of the DAC diabatic states,[50, 69] which is critical in the ATD transformation process; in MSDFT, phases are explicitly expressed, in conjunction with the off-diagonal Hamiltonian matrix elements, in the overlap integral between different states in defining orthogonal as well as non-orthogonal diabatic states.

2.4.4. Diabatic Coupling

The squared diabatic couplings (i.e., the off-diagonal elements of the diabatic Hamiltonian for the orthogonalized diabatic states) energies are shown in Figure 2.5 for the diabatic states of Figure 2.4.d. Since there are numerous pairs among the diabatic states in the present MSDFT approach, which is not restricted to only four adiabatic surfaces, for clarity we show only a few selected couplings directly relevant to the avoided crossing interactions. The diabatic states in the present MSDFT approach are all fully coupled, and their diabatic couplings do not necessarily show peaked values near the crossing geometries often found in the ATD transformed diabatic states.[50, 75, 76] This is because, given that the orthogonalization of the VB diabatic states yielded crossings near

the minimum gap region of the adiabatic potential energy curves, they still retain their respective valence character. In MSDFT, diabatic interactions do not vanish at short interatomic distances, and they play a crucial role in chemical bond formation in all states. On the other hand, the "diabatic couplings" in the ATD transformation quickly decay to nearly zero away from the avoided crossing geometries. These differences between the ATD transformed states and the present DAC states may have consequences in dynamic simulations of nonadiabatic processes, and further studies of their performances, which are beyond the scope of this article on the PES itself, would be interesting.

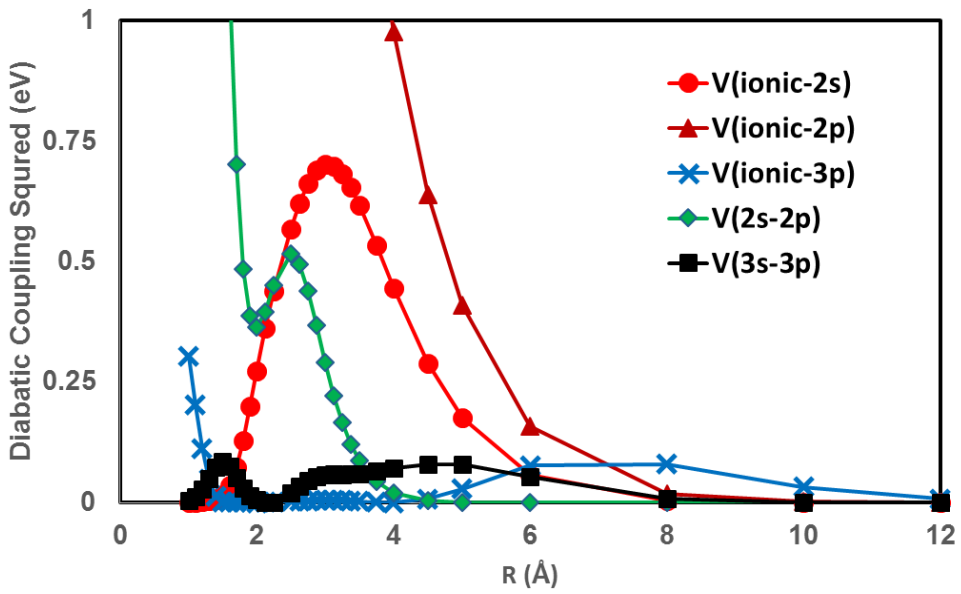

Figure 2.5. Squared diabatic couplings between selected pairs of orthogonal diabatic states of LiH shown in Figure 2.4(d) as a function of interatomic separation. All results are determined by MSDFT with the aug-cc-pVTZ basis set (see Figure 2.1).

In the present study, we have not attempted to minimize, or have examined if the VB-inspired, DAC diabatic states actually minimize derivative coupling. In the present case, as there is only one degree of freedom, we can determine the derivative coupling in the bond dissociation coordinate. The MSDFT derivative coupling results are shown in Figure 2.6. It would be interesting to examine this property on complex systems.

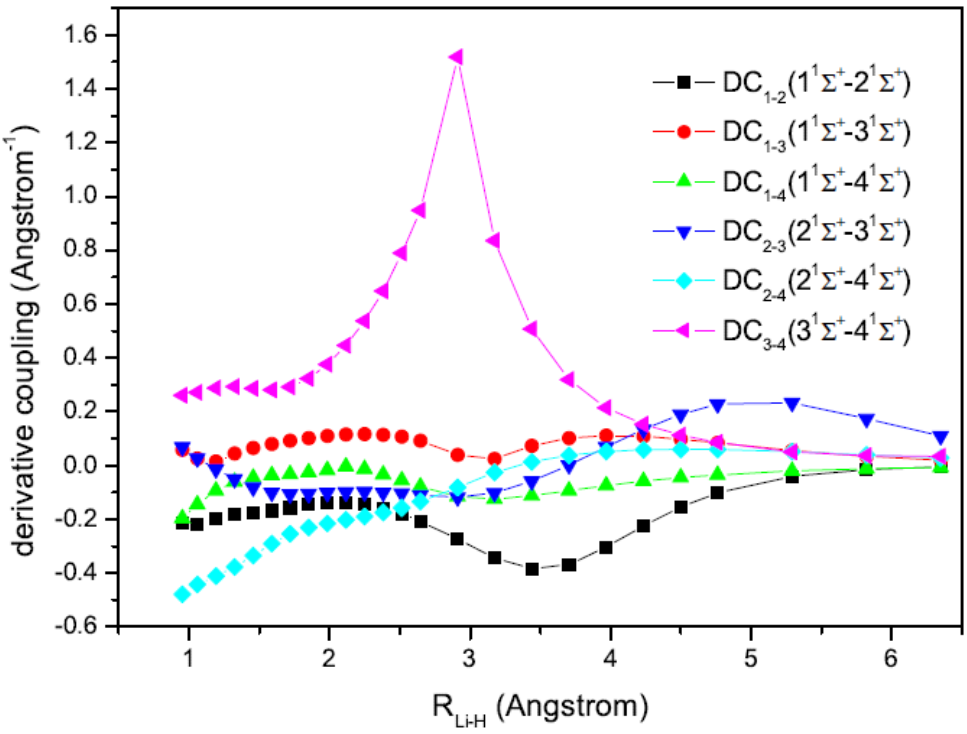

Figure 2.6. Compued derivative coupling values, $<\Psi_I(\mathbf{r};\mathbf{R})|\nabla_R|\Psi_J(\mathbf{r};\mathbf{R})>$ for various states indicated as a function of interatomic separation. All results are determined by MSDFT with the aug-cc-pVTZ basis set (see Figure 2.1).

2.5. Conclusions

Multistate density functional theory (MSDFT) for the calculation of adiabatic and diabatic potentials is presented, and it is illustrated for the extensively studied LiH

diatomic molecule. The method represents the ground and excited states and their potential energy curves according to Lewis resonance structures of a given molecular system. The present method belongs to a category called diabatic-at-construction (DAC) strategy, which differs from the more widely used adiabatic-to-diabatic (ATD) transformation procedure. The DAC diabatic states are non-orthogonal and they are defined (or, the CSFs can be directly used) as the basis states in an active space for configuration interaction to yield the adiabatic states. This is in contrast to the ATD approach, which is based on an orthogonal transformation of a set of pre-selected adiabatic states and a similarity transformation of their energies. There is no rigorous physical interpretation of any set of diabatic states since they are not unique, but the DAC diabatic states are formulated according to the valence bond characters of the dissociation limits of different adiabatic states, which are strictly maintained at all molecular geometries. Therefore, the DAC diabatic states have well-defined physical and chemical meanings, which provide further insight in the understanding of bonding interactions and for determination of specific energy contributions by energy decomposition analysis.[90, 92] The adequacy and completeness of such interpretations and energy component analyses can be validated by the results of the electronic couplings among the DAC states.

Qualitative trends of the ATD diabatic states derived by the threefold way from the relevant adiabatic states can be reproduced by similarity transformation of the non-orthogonal DAC diabatic states, and comparison between the two reveals certain necessary conditions required for this agreement, including mixing of some VB states and retaining the dissociation limits. Quantitative results on the computed diabatic

couplings indicate that the ATD diabatic states represent essentially mixed adiabatic potential energy curves away from the avoided crossing regions with diminished diabatic couplings, but peaked values in these regions. On the other hand, orthogonalized DAC diabatic states do not generally exhibit peaked diabatic couplings at the avoided crossings (although some states do), since they are responsible for chemical bonding interactions. It would be interesting in future studies to gain an understanding of the different roles of the different diabatic couplings from the ATD and the DAC states in dynamic simulations.

Chapter 3. Spin-Multiplet Components and Energy Splittings by Multistate Density Functional Theory

Adapted with permission from A. Grofe, X. Chen, W. Liu, and J. Gao, J. Phys. Chem. Lett. **8**, 4838 (2017).

This work was performed in collaboration with Xin Chen and Jiali Gao.

3.1. Introduction

Kohn-Sham density functional theory (KS-DFT) and time-dependent density functional theory (TDDFT) are widely used to study the structures and properties of ground and excited states of atoms, molecules and condensed-phase systems.[114] In principle, in the absence of an external magnetic field, the ground-state energy of a many-electron system, irrespective of its degeneracy, is solely determined by its exact charge density, ρ.[115] However, KS-DFT,[116] on the basis of a single Slater determinant, is incapable of describing the zero-field degeneracy of spin-multiplet components, ultimately limiting its application to modeling low-spin states in transition metal chemistry, bond dissociation and photochemistry.[117] For example, whereas the high-spin components of a triplet diradical can be adequately modeled by KS-DFT, the $M_S = 0$ component is of two-configurational character, which needs to be treated by multiconfigurational approaches beyond the Kohn-Sham density functional approximation.[118] For the open-shell singlet state, spin-polarized DFT is typically used,[119] in which the approximate exchange-correlation functional is dependent on both the spin-

up (ρ_α) and spin-down (ρ_β) densities. In this case, the single determinant representation of the singlet state is spin-contaminated, and a weighted broken-symmetry scheme is often used to estimate the singlet-triplet energy splitting.[120] The latter approach only works well for simple situations.[121] Analogously, excited states of open-shell systems from unrestricted TDDFT can be heavily spin-contaminated, and spin-adapted (SA) TDDFT approaches[122-124] should be used to correctly yield excitation energies.[125, 126] Therefore, there is urgency and it is significant to develop DFT-based methods to overcome these difficulties.

In this chapter, we first describe a multistate density functional theory (MSDFT)[19, 26, 127] for representing spin-multiplet components and for determining high and low-spin energy gaps of open-shell systems. Then, we show that, for spin-multiplet systems examined in this work, the transition density functional in MSDFT, characterizing the electronic coupling of spin-localized configurations, can be rigorously defined for a given density functional approximation.

In wave function theory (WFT), there is a well-established, systematic route to treat the electronic structure of open-shell systems with inclusion of both static and dynamic correlations. In DFT, multiconfigurational approaches have been explored,[118, 128-134] but they have not yet gained widespread application. A most effective method for predicting singlet-triplet splitting, both in WFT and DFT, is the spin-flip (SF) method,[12, 135-137] which describes both closed and open-shell singlet states by electronic excitation with an $\alpha \rightarrow \beta$ spin inversion, starting from a high-spin reference state (*e.g.*, the triplet state). However, the SF approach does not deal with the general question of multiplet

degeneracy. For a given spin-multiplet component M_S, the density variables ρ_α and ρ_β are dependent on the projection of the total spin S with a spin density of $Q^{M_S} = \{M_S / S\}Q^S$ where Q^S is that of the highest component. Although the ground-state energy depends only on the total density that is identical for all components, an M_S–dependent functional is currently not available in the framework of KS-DFT. The general approach to this problem is to transform the spin-dependent densities into spin-independent variables. This was first described by using the M_S–independent on-top pair density (along with ρ) as the DFT input instead of the spin polarization,[118] and an alternative transformation of the total density and the density of effectively unpaired electrons has been made to replace ρ_α and ρ_β.[138] It is important to note that the first method employs a multiconfiguration self-consistent field (MCSCF) reference wavefunction, such as the complete-active-space self-consistent field (CASSCF), to yield the on-top pair density, whereas single determinants that differ only in spin orientations of unpaired electrons are used in the latter case to model their energy degeneracy. As in standard KS-DFT, the determinant to yield the transformed densities does not model the correct symmetry and corresponds to mixed pure spin states.[138]

3.2. Multistate Density Functional Theory

Multistate density functional theory (MSDFT)[19, 127] is a hybrid approach that combines advantages of both WFT and DFT, and it belongs to the "dynamic-then-static" (DTS) ansatz for treating electron correlation.[20, 22] There are two computational steps: (1)

the construction of an active space consisting of N_p states $\{\Psi_A; A=1,\cdots,N_p\}$, in which dynamic correlation is first modeled into each constituent configuration, and (2) diagonalization of the configuration interaction (CI) Hamiltonian or MCSCF optimization of the wave function to include static correlation. In other words, DFT is used as an effective Hamiltonian to define the N_p electronic configurations in the active (primary) space, which, by construction, includes dynamic correlation in the first place. Then, WFT is employed to yield the wave functions and energies of the adiabatic states, especially for systems with strong static correlation caused by near degeneracies of the ground and low-lying excited states. Other approaches with similar spirit include multireference CI based on Kohn-Sham orbitals (DFT/MRCI)[130] and spin-restricted ensemble DFT.[129, 139]

In MSDFT,[127] the wave function Φ_I, electron density ρ_I, and energy density-functional $E_I^{\mathrm{MS}}[\rho_I]$ for the adiabatic ground state ($I=0$) and excited states ($I<N_p$) are given as follows

$$\Phi_I = \sum_{A=1}^{N_p} a_{AI}\Psi_A \tag{3.2.1}$$

$$\rho_I(x) = \sum_{A=1}^{N_p} \{a_{AI}^2 \rho_A^{\mathrm{ms}}(x) + \sum_{B\neq A} a_{AI}a_{BI}\rho_{AB}(x)\} \tag{3.2.2}$$

$$E_I^{\mathrm{MS}}[\rho_I(x)] = \sum_{A=1}^{N_p} \{a_A^2 E^{\mathrm{KS}}[\rho_A^{\mathrm{ms}}(x)] + \sum_{B\neq A} a_{AI}a_{BI}E^{\mathrm{TDF}}[\rho_{AB}(x)]\} \tag{3.2.3}$$

where a_{AI} is a configuration coefficient for state *I*, satisfying the normalization condition $\sum_{A,B=1}^{N_p} a_{AI} a_{BI} S_{AB} = 1$ with S_{AB} being the overlap between determinants Ψ_A and Ψ_B. The electron density $\rho_A^{\mathrm{ms}}(x)$ of configuration *A* (*A* = *B*), and the transition density $\rho_{AB}(x)$ between basis configurations *A* and *B* are expanded over a set of *m* atomic orbital basis functions $\{\chi_\mu(x), \mu = 1, \cdots, m\}$:

$$\rho_{AB}(x) = \sum_{\mu\nu}^{m} D_{\mu\nu}^{AB} \chi_\mu(x) \chi_\nu(x) \tag{3.2.4}$$

where *x* specifies the spatial (**r**) and spin (σ) coordinates, and $\mathbf{D}^{AB}$ is the density matrix defined by two (in general) non-orthogonal Slater determinants Ψ_A and Ψ_B.[19, 23-25] $E^{\mathrm{KS}}[\rho_A^{\mathrm{ms}}(\mathbf{r})]$, which is the diagonal matrix element of the Hamiltonian, is the KS-DFT energy for state Ψ_A, and $E^{\mathrm{TDF}}[\rho_{AB}(\mathbf{r})]$ is the transition density functional that defines the electronic coupling between Ψ_A and Ψ_B.

The superscript KS in equation 3.2.3 emphasizes that MSDFT is built up on KS-DFT and makes use of the wide range of exchange-correlation functionals that have been developed, such as local density approximation (LDA), generalized gradient approximation (GGA) and hybrid functionals. The superscript TDF specifies a new class of correlation functionals with the transition density from multiconfigurational methods as input. We note that ρ_{AB} satisfies the symmetry, rank, and generalized idempotency conditions,[19] though it can be non-positive or even complex.

Several comments may be made here (for further details, see reference 127).

First, equations 3.1.1 through 3.1.3 represent a departure from conventional KS-DFT, in that there is a multiconfigurational wave function for each adiabatic state in MSDFT, which defines the corresponding total electron density as a sum of the weighted KS densities and transition densities. The latter emphasizes the importance of configuration coupling, which is lacking in ensemble density functional theory.[29] Furthermore, the electronic coupling can be used to estimate the transfer integral needed to compute the rate of electron transfer and excited energy transfer processes.[26] Note that the energy density-functional in MSDFT does not explicitly use the total electron density as an input for an exchange-correlation functional, a fundamental difference from other multiconfigurational density functional approaches.[134] As discussed in reference 127, when $N_p = 1$, MSDFT reduces to the conventional KS-DFT, and when $N_p = N_f$, the full configurational space, MSDFT is equivalent to full CI. In approaching the latter limit, a second-order perturbation-based scaling can be made to convert the diagonal DFT energies into pure determinant energies.[127] Thus, MSDFT is a hybrid WFT and DFT, bridging the two branches of electronic structure theory for molecular systems.

Secondly, the wave function (equation 3.1.1) and energy functional (equation 3.1.3) can be obtained either with the orbitals held fixed for each configuration, involving only one diagonalization of the Hamiltonian (which is used in this study), or by variational optimization of both the configurational and orbital coefficients of all states as in an MCSCF calculation, such as CASSCF. As shown previously, MSDFT provides a natural approach to define electronic diabatic states directly, called diabatic at

construction (DAC),[140] for non-adiabatic processes. In this regard, the basis configurations, $\{\Psi_A; A=1,\cdots,N_p\}$, used in the former (MCSCF type) approach are called the variational diabatic configurations (VDC), and in the latter (CI type) approach, the consistent diabatic configurations (CDC).[36]

Thirdly, the introduction of transition densities, which is natural in a multiconfigurational approach, and of transition density functional $E^{\mathrm{TDF}}[\rho_{AB}(\mathbf{r})]$, which is beyond the Kohn-Sham approximation, represent the key concept of MSDFT. A rigorous definition of E^{TDF} can be made for certain special situations that are examined here in association with a given, approximate exchange-correlation functional developed in KS-DFT. This is the key result of this work (below).

3.3. Transition Density Functional Design for Spin Components

The transition density functional (TDF), representing the electronic coupling between configurations Ψ_A and Ψ_B, includes two components, the contribution identical to that in standard WFT, $<\Psi_A|H|\Psi_B>$, and a dynamic correlation functional, $V_c^{\mathrm{TDF}}[\rho_{AB}(\mathbf{r})]$, involving the external space:[127]

$$E^{\mathrm{TDF}}[\rho_{AB}(\mathbf{r})] \equiv H_{AB} = <\Psi_A|H|\Psi_B> + V_c^{\mathrm{TDF}}[\rho_{AB}(\mathbf{r})] \qquad (3.3.1)$$

where H is the electronic Hamiltonian. The first term in equation 3.3.1 is the electronic coupling between, in general, two non-orthogonal determinant configurations,[23] including correlation within the active space, which has been used in the MOVB (mixed molecular orbital and valence bond) approach.[24, 25] An approximation to resolve double counting of

electron correlation in the active space was given in reference 127, and an alternative approach has been suggested by Savin and coworkers.[33] Since the number of configurations in this study is small, and mostly degenerate, such a static correlation is not included in KS-DFT, which captures dynamic effects of the external space in the present systems. The second term in equation 3.3.1 is a transition density contribution, representing dynamic correlation not included in the first term.[127]

As noted above, there is no correspondence in KS-DFT for $V_c^{\mathrm{TDF}}[\rho_{AB}(\mathbf{r})]$, and approximations such as overlap or $<\Psi_A|H|\Psi_B>$ weighted correlation energies have been used previously with encouraging results.[19, 26, 92, 141] Grimme proposed to scale $<\Psi_A|H|\Psi_B>$ by an exponential function to approximate H_{AB}.[130] Importantly, the multistate density functional (equation 3.1.3) needed for determining the energy of a low-spin component can be obtained rigorously by making use of the energy degeneracy condition of a given (high) spin multiplet, an idea that has been explored.[142, 143] This is straightforwardly illustrated by considering the $M_S = 0$ component of the ground state of carbon, which is a triplet ^{3}P state.

Here, both the $M_S = 0$ component of the ^{3}P ground state (denoting the pure spin state that is both eigenfunction of $\hat{S}^2$ and of $\hat{S}_z$ by $|S, M_S>$, *i.e.*, $|1,0>$) and the first, singlet ^{1}D excited state ($|0,0>$) of carbon result from spin-coupling interactions of the determinants $\Psi_1^{\mathrm{C}} = |cs\bar{s}x\bar{y}|$ and $\Psi_2^{\mathrm{C}} = |cs\bar{s}x\bar{y}|$, where the superscript C indicates carbon atom, *c* specifies all doubly occupied core orbitals (which will be omitted below

throughout for simplicity) and the bar denotes an electron with β spin in a valence orbital. These two determinant configurations fully define the active space ($N_p = 2$ in equation 3.1.1) for the spin-multiplet states $|1,0>$ and $|0,0>$ (in general, the dimension of equation 3.1.1 is the number of spin components in consideration), and diagonalization of the 2×2 Hamiltonian matrix yields their wave functions with in-phase (positive) and out-phase (negative) combinations, respectively, and their energies.

$$\Phi^{\mathrm{C}}_{^3\mathrm{P}}(|1,0>) = \frac{1}{\sqrt{2}}(\Psi^{\mathrm{C}}_1 + \Psi^{\mathrm{C}}_2) \tag{3.3.2.a}$$

$$\Phi^{\mathrm{C}}_{^1\mathrm{D}}(|0,0>) = \frac{1}{\sqrt{2}}(\Psi^{\mathrm{C}}_1 - \Psi^{\mathrm{C}}_2) \tag{3.3.3.b}$$

For a given exchange-correlation functional used to compute the diagonal matrix terms, $H_{11} = E^{\mathrm{KS}}[\rho^{\mathrm{C}}_1(\Psi^{\mathrm{C}}_1)]$ and $H_{22} = E^{\mathrm{KS}}[\rho^{\mathrm{C}}_2(\Psi^{\mathrm{C}}_2)]$, where Ψ^{C}_1 and Ψ^{C}_2 are used as Kohn-Sham determinants for the respective configurations, we make use of the condition that the energies of the high spin component from a single-determinant restricted open-shell KS-DFT calculation, $\Phi^{\mathrm{C}}_{^3\mathrm{P}}(|1,1>) \equiv \Psi^{\mathrm{C}}_3 = |s\bar{s}xy|$, and of the low spin component from MSDFT using $\Phi^{\mathrm{C}}_{^3\mathrm{P}}(|1,0>)$ are identical in the absence of an external magnetic field:[142-144]

$$E^{\mathrm{MSDFT}}(|1,0>) = E^{\mathrm{KS}}(|1,1>) \tag{3.3.4}$$

Then, the correlation energy of the TDF can be uniquely determined by

$$V_c^{\mathrm{TDF}}(\rho^{\mathrm{C}}_{12}) = \Delta E_c^{\mathrm{KS}}(\rho^{\mathrm{C}}_3) - \Delta E_c^{\mathrm{KS}}(\rho^{\mathrm{C}}_1) \tag{3.3.5}$$

where $\Delta E_c^{\mathrm{KS}}(\rho_A)=E^{\mathrm{KS}}(\rho_A)-E^{\mathrm{HF}}(\Psi_A)$ is the energy difference between KS-DFT and Hartree-Fock theory using the Kohn-Sham determinant Ψ_A. Note that $\Delta E_c^{\mathrm{KS}}(\rho_1^{\mathrm{C}})=\Delta E_c^{\mathrm{KS}}(\rho_2^{\mathrm{C}})$ for the two single-determinants of mixed states. The correlation energy defined in equation 3.3.5 for the transition density functional also leads to the energy for the ^{1}D singlet state (equation 3.3.3.b). Together, they yield the singlet-triplet (S-T) energy splitting $\Delta E_{ST} = E_S(|0,0>) - E_T(|1,0>)$ (of course, we have $E_T(|1,1>) = E_T(|1,0>)$).

Equation 3.3.5 is generally applicable to molecular diradicals for determining ΔE_{ST}. One simply replaces the atomic orbitals by the corresponding MOs, and this is used in the AH_2 isovalent electron cases and *ortho*, *meta*, and *para*-didehydrotoluene (DHT), two systems that have been extensively used for validation of theory.[12, 137, 145]

For interactions involving non-degenerate orbitals, the TDFs can be similarly determined. This is illustrated by the low-energy states of boron (Figure 3.1). In this case, transition from the doublet ground-state (^{2}P) to the $2s^12p^2$ configuration yields its lowest excited state, a quartet (^{4}P) state, and three doublets, ^{2}D, ^{2}S, and ^{2}P, in order of increasing energy (^{2}P is above the ionization limit). The $|\frac{3}{2},\frac{3}{2}>$ component of the ^{4}P state, $\Psi_4^{\mathrm{B}} = |sxy|$, of single-determinant character, can be conveniently approximated by restricted open shell (RO) KS-DFT, whereas the active space that defines the $|\frac{3}{2},\frac{1}{2}>$ component and the ^{2}D and ^{2}P multiplets consists of three low-spin determinant

configurations: $\Psi_1^{\mathrm{B}} = |\bar{s}xy|$, $\Psi_2^{\mathrm{B}} = |s\bar{x}y|$, and $\Psi_3^{\mathrm{B}} = |sx\bar{y}|$. The wave function for the $M_S = 1/2$ component of the quartet state from MSDFT is given by

$$\Phi_{^4\mathrm{P}}^{\mathrm{B}}(|\frac{3}{2},\frac{1}{2}>) = \frac{1}{\sqrt{3}}(\Psi_1^{\mathrm{B}} + \Psi_2^{\mathrm{B}} + \Psi_3^{\mathrm{B}}) \tag{3.3.6}$$

Then, the condition $E^{\mathrm{MSDFT}}[\Phi_{^4\mathrm{P}}^{\mathrm{B}}(|\frac{3}{2},\frac{1}{2}>)] = E^{\mathrm{KS}}[\Phi_{^4\mathrm{P}}^{\mathrm{B}}(|\frac{3}{2},\frac{3}{2}>)]$ after solving the secular equation leads to the TDF correlation energies as follows:

$$V_c^{\mathrm{TDF}}(\rho_{12}^{\mathrm{B}}) \equiv V_c^{\mathrm{TDF}}(\rho_{13}^{\mathrm{B}}) = \frac{\Delta E_c^{\mathrm{KS}}(\Psi_4^{\mathrm{B}}) - \Delta E_c^{\mathrm{KS}}(\Psi_1^{\mathrm{B}})}{2} \tag{3.3.7}$$

$$V_c^{\mathrm{TDF}}(\rho_{23}^{\mathrm{B}}) = \frac{\Delta E_c^{\mathrm{KS}}(\Psi_4^{\mathrm{B}}) + \Delta E_c^{\mathrm{KS}}(\Psi_1^{\mathrm{B}})}{2} - \Delta E_c^{\mathrm{KS}}(\Psi_2^{\mathrm{B}}) \tag{3.3.8}$$

where the numbers in the subscript specify the determinant configurations of the basis states $\{\Psi_i^{\mathrm{B}}; i = 1,\cdots,4\}$ that have been defined above. Notice that for B, $\Delta E_c^{\mathrm{KS}}(\Psi_2^{\mathrm{B}}) = \Delta E_c^{\mathrm{KS}}(\Psi_3^{\mathrm{B}})$.

In addition to the low-spin component of the ^{4}P state, the TDF couplings given in equations 3.3.7 and 3.3.8 also determines the energies of the ^{2}D and ^{2}P states:

$$\Phi_{^2\mathrm{D}}^{\mathrm{B}}(|\frac{1}{2},\frac{1}{2}>) = \frac{1}{\sqrt{2}}(\Psi_2^{\mathrm{B}} - \Psi_3^{\mathrm{B}}) \tag{3.3.9.a}$$

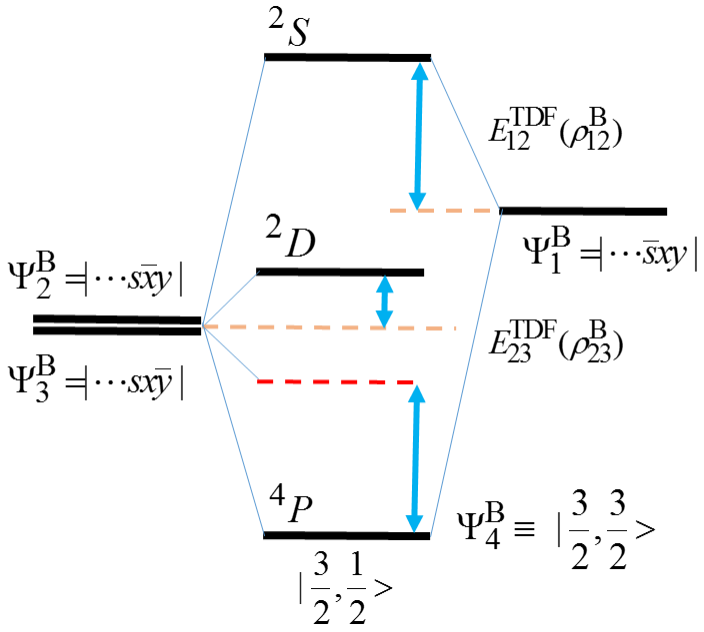

Figure 3.1. Interaction diagram illustrating electronic coupling among the three determinant configurations for the excited $2s^1 2p^2$ configuration of boron atom.

$$\Phi_{^2S}^B(|\frac{1}{2},\frac{1}{2}>) = \frac{1}{\sqrt{6}}(2\Psi_1^B - \Psi_2^B - \Psi_3^B) \qquad (3.3.9.b)$$

It is interesting to note that the configuration $\Psi_2^B = |s\bar{x}y|$ in fact involves a two-electron transition of the ground state $|s\bar{s}x|$, $2p_x \rightarrow 2p_y$ and $2\bar{s} \rightarrow 2\bar{p}_x$, not included in conventional TD-DFT. Of course, they are treated properly in spin flip time dependent density functional theory (SF-TDDFT) by double SF[146] and state average time dependent density functional theory (SA-TDDFT) approaches.[122, 125, 126]

3.4. Results and Discussion

Illustrative examples are presented to show the ability of MSDFT for representing spin multiplet components and for determining energy gaps of high and low spin multiplets. We have selected a series of atomic energy levels of first-row elements. These systems are chosen because there is no ambiguity for comparison with experimental data associated with the geometries and zero-point energies of different adiabatic states of molecules. To further demonstrate its applicability to molecular systems, the energies of low-lying states in the isovalent electron system of CH_2, NH_2^+, SiH_2, and PH_2^+, and of three isomers of didehydrotoluene (DHT) are computed. These compounds exhibit different degrees of diradical character. The hybrid PBE0 and M06-HF functionals are used in the present work, along with the PBEC functional, which, as M06-HF, uses 100% Hartree-Fock exchange. The aug-cc-pVQZ basis set is used for the atoms and AH_2 hydrides, and cc-pVTZ for the DHT isomers; these basis functions are sufficiently large, as shown in previous studies for these systems.[12, 137] The MSDFT calculations are performed using a modified version of GAMESS.[147] We have used restricted open-shell (RO) KS-DFT to model the high-spin components, which are adequately represented by single determinant, and their orbitals are used in the low-spin multiconfigurational calculations.

For atomic systems, the orbital basis functions are partitioned into four blocks: three of p_x, p_y, and p_z symmetry, and the fourth including the rest of the core and valence *s* electrons. Without sacrificing generality here, we use the real atomic orbitals instead of spherical harmonics with specific magnetic quantum numbers. For the

diradical series AH_2 (A = C, N, Si, and P), the molecular orbitals (MO) are divided into three blocks, corresponding to p_z (perpendicular to the molecular plane), n_x (an sp^2-type hybrid orbital in the orientation (*x*) bisecting the two chemical bonds), and the remainder of orbitals (which are doubly occupied MOs). This may be generalized to other open-shell diradical cases such as DHT, of three orbital blocks consisting of two singly occupied MOs and the rest of doubly occupied orbitals. In each case, the orbitals for the $M_S = S$ state are optimized using RO- KS-DFT, and its energy is denoted by $E(|S, M_S = S>)$. These orbitals are then used to construct configurations in the active space for the lower spin components of *S*, and its lower spin multiplets. However, for the AH_2 series, the two closed shell determinants for the $\tilde{a}^1A_1$ and $\tilde{c}^1A_1$ states, corresponding to the configuration $|cn_x\bar{n}_x|$ and its double excitation to $|cp_z\bar{p}_z|$, are optimized separately – a situation that is different from the SF approaches.

Table 3.1. Experimental and computed atomic excitation energies (eV) of beryllium, boron, carbon, nitrogen, and oxygen using multistate density functional theory (MSDFT) and mixed molecular orbital-valence bond theory (MOVB). The pure spin state is indicated by $|S,M_S>$. The hybrid functional PBE0 and PBEC with 25% and 100% Hartree-Fock exchange as well as M06-HF, also containing 100% Hartree-Fock exchange are used. The aug-cc-pVQZ basis is used in all computations. MUD: mean unsigned deviations from experiment.

Config.[a]	Term	$\|S,M_S>$	Exp[b]	MOVB	PBE0	PBEC	M06HF
Be ($2s^2 2p^0$)	^{1}S	$\|0,0>$	0	0	0	0	0
$2s^1 2p^1$	^{3}P	$\|1,1>, \|1,0>$	2.72	1.62	2.29	2.21	3.06
	^{1}P	$\|0,0>$	5.28	5.90	4.59	6.07	4.54
$2s^0 2p^2$	^{1}D	$\|0,0>$	7.05	6.44	6.22	7.08	7.12
	^{3}P	$\|1,1>, \|1,0>$	7.40	7.38	6.41	7.54	7.36
B ($2s^2 2p^1$)	^{2}P	$\|1/2,1/2>$	0	0	0	0	0
$2s^1 2p^2$	^{4}P	$\|3/2,3/2>$, $\|3/2,1/2>$	3.55	2.08	3.18	2.96	4.27
	^{2}D	$\|1/2,1/2>$	5.93	6.08	5.59	6.14	6.43
	^{2}S	$\|1/2,1/2>$	7.88	7.39	7.00	7.62	6.95
	^{2}P	$\|1/2,1/2>$	8.99	10.14	7.75	9.83	7.43
C ($2s^2 2p^2$)	^{3}P	$\|1,1>, \|1,0>$	0	0	0	0	0
	^{1}D	$\|0,0>$	1.26	1.58	1.01	1.29	1.51
	^{1}S	$\|0,0>$	2.68	3.18	2.98	2.17	1.88
$2s^1 2p^3$	^{5}S	$\|2,2>, \|2,1>$	4.19	2.43	3.96	3.60	5.34
	^{3}D	$\|1,1>$	7.95	8.13	7.60	8.27	8.38
	^{3}P	$\|1,1>$	9.33	9.76	9.39	10.12	9.95
N ($2s^2 2p^3$)	^{4}S	$\|3/2,3/2>$, $\|3/2,1/2>$	0	0	0	0	0
	^{2}D	$\|1/2,1/2>$	2.38	2.89	1.96	2.45	2.75
	^{2}P	$\|1/2,1/2>$	3.58	4.82	4.35	4.60	3.36
$2s^1 2p^4$	^{4}P	$\|3/2,3/2>$, $\|3/2,1/2>$	10.33	10.78	10.58	11.27	NC[c]
O ($2s^2 2p^4$)	^{3}P	$\|1,1>, \|1,0>$	0	0	0	0	0
	^{1}D	$\|0,0>$	1.97	2.28	1.64	2.00	2.25
	^{1}S	$\|0,0>$	4.19	4.57	4.42	4.30	3.08
MUD				0.64	0.42	0.43	0.57

a. Configuration
b. Reference 105.
c. NC: RO-SCF not converged.

The computed atomic valence-excitation energies for Be through O are listed in Table 3.1 along with the specific pure spin states indicated by $|S, M_S>$ (negative M_S components are omitted). Note that each $|S, M_S>$ state in Table 3.1 has been explicitly constructed and they are shown to emphasize that the energies of multiplet components are exactly degenerate. For each configuration, only the highest spin component is of single-determinant character, while all other states are multiconfigurational. States that are of single-determinant character are determined by RO-KS-DFT. Thus, the results for the high-spin states reflect the accuracy of the exchange-correlation functional used for these cases. The computed energies for all valence excited states in Table 3.1 are reasonable in comparison with experiments, with the mean-unsigned-deviations (MUD) being 0.42, 0.43, and 0.57 eV for PBE0, PBEC, and M06-HF density functionals, respectively, without inclusion of the two highly excited states (^{3}P of Be and ^{2}P of B). If one only considers the spin-multiplet energy splittings for C, N, and O, the MUD errors are 0.33, 0.04, and 0.30 eV using PBE0, PBEC, and M06-HF. Not surprisingly, Table 3.1 shows that the MUD errors are noticeably larger for results with the MOVB method, which does not include dynamic correlation. Nevertheless, a main purpose of this study is to show that MSDFT can be used to treat both high and low-spin states as well as their individual components with the correct symmetry and energy degeneracy exactly.

The isovalent series of CH_2, NH_2^+, SiH_2, and PH_2^+ molecules have been extensively studied experimentally and computationally, and they are popular choices for testing theory. The qualitative picture of their electronic structures has been lucidly summarized by Slipchenko and Krylov.[145] In addition to the open-shell triplet and singlet states, resulting from configuration interactions of two singly occupied $3a_1$ and $1b_1$ ($5a_1$ and $2b_1$ for the heavier hydrides) orbitals (simply denoted by p_z and n_x where the latter is an sp^n hybrid orbital), there are two closed-shell singlet states. All three singlet states as well as the $M_S = 0$ component of the triplet state are muticonfigurational.

The configuration space for the hydride species in MSDFT calculations includes four determinant configurations, $\Psi_1^{AH_2} = | p_z, \bar{n}_x |$, $\Psi_2^{AH_2} = | \bar{p}_z, n_x |$, $\Psi_3^{AH_2} = | n_x, \bar{n}_x |$, and $\Psi_4^{AH_2} = | p_z, \bar{p}_z |$ (as usual, we have omitted core orbitals in the notation), and their linear combinations yield the four low-spin adiabatic states that are eigenfunctions of $\hat{S}^2$ and $\hat{S}_z$. The TDF for the coupling between the two open-shell determinants was determined exactly for a given exchange-correlation functional. However, an exact expression for the coupling between two doubly occupied configurations ($\Psi_3^{AH_2}$ and $\Psi_4^{AH_2}$) is not available. Here, we have used a weighted correlation energy to approximate the TDF dynamic correlation:

$$V_c^{TDF}(\rho_{34}^{AH_2}) \approx \frac{\Delta E_c^{KS}(\Psi_3^{AH_2}) + \Delta E_c^{KS}(\Psi_4^{AH_2})}{E^{HF}(\Psi_3^{AH_2}) + E^{HF}(\Psi_4^{AH_2})} < \Psi_3^{AH_2} | H | \Psi_4^{AH_2} > \qquad (3.4.1)$$

Computed excitation energies for the hydride series are given in Table 3.2 along with results from the SF approaches.[137] The MSDFT results are compared with SF-CCSD(T) energies, which has a mean error of about 0.036 eV relative to the 7 available experimental data that have been corrected for zero-point vibrational energies.[137] An MUD error of 0.136 eV was found for MSDFT overall all 12 excitation energies, which is just slightly greater than that from non-collinear SF-TDDFT, both using the PBE0 functional. Of the four S-T energy splittings, the relative errors are 0.045 and 0.057 eV for MSDFT and SF-TDDFT, respectively, with respect to CCSD(T) values. The PBE0 functional performs exceptionally well for S-T splitting in the non-collinear SF-TDDFT calculations, but other functionals show large fluctuations and even the opposite sign.[137] This behavior was attributed to using the $M_S = 0$ component for the triplet-state, rather than the high-spin reference itself, which has a small amount of spin contamination. In MSDFT, however, we use restricted open-shell orbitals, which raises the energy for the triplet state by 0.07 eV (1.65 kcal/mol), which contributes to errors in the calculated S-T energies. For the two closed-shell singlet states ($^1A_1$), the resonance stabilization energy (their coupling) due to dynamic correlation (equation 3.4.1) is relatively small (0.02 eV) compared to that of the determinant contribution (0.23 eV) in equation 3.3.1.

Table 3.2. Computed adiabatic excitation energies (eV) of CH_2, NH_2^+, SiH_2, and PH_2^+ molecules. Spin-flip (SF) results are taken from reference 137 for comparison. The PBE0 exchange-correlation functional is used both in SF and in multistate (MS) DFT, and the aug-cc-pVQZ basis set is used in all calculations.[a]

Hydride	State[d]	SF-CCSD(T)[b]	NC-SF-DFT[b]	MSDFT	Expt.[c]
CH_2 ($\tilde{X}\ ^3B_1$)	$\tilde{a}\ ^1A_1$	0.420	0.507	0.431	0.39
	$\tilde{b}\ ^1B_1$	1.410	1.410	1.285	1.425
	$\tilde{c}\ ^1A_1$	2.530	2.820	2.749	
NH_2^+ ($\tilde{X}\ ^3B_1$)	$\tilde{a}\ ^1A_1$	1.253	1.336	1.206	1.306
	$\tilde{b}\ ^1B_1$	1.865	1.856	1.609	
	$\tilde{c}\ ^1A_1$ ($\tilde{c}\ ^1\Sigma_g^+$)	3.318	3.701	3.576	
SiH_2 ($\tilde{X}\ ^1A_1$)	$\tilde{a}\ ^3B_1$	0.892	0.944	0.854	0.91
	$\tilde{A}\ ^1B_1$	1.937	1.918	2.033	1.928
	$\tilde{B}\ ^1A_1$	3.365	3.507	3.633	
PH_2^+ ($\tilde{X}\ ^1A_1$)	$\tilde{a}\ ^3B_1$	0.794	0.800	0.712	0.75
	$\tilde{A}\ ^1B_1$	1.993	1.943	2.008	1.92
	$\tilde{B}\ ^1A_1$	3.640	3.784	3.853	
	MUD (ΔE_{ST})	(0.036)	0.057	0.045	
	MUD (total)	(0.034)	0.105	0.136	

a. Total energies are -39.11577, -55.42594, -290.50214, and -342.03056, for CH_2, NH_2^+, SiH_2, and PH_2^+, respectively, using MSDFT(4)/aug-cc-pVQZ, using geometries optimized by FCI/TZ3P for CH_2,[148] and CISD/TZ3P(2d,2f) in other cases.[149-151]

b. Reference 137.

c. Values are taken from reference 137.

Figure 3.2 shows the adiabatic and "vertical" excitation energies of CH_2 at the optimal geometries of the four states. Clearly seen is that the energy for each state is in

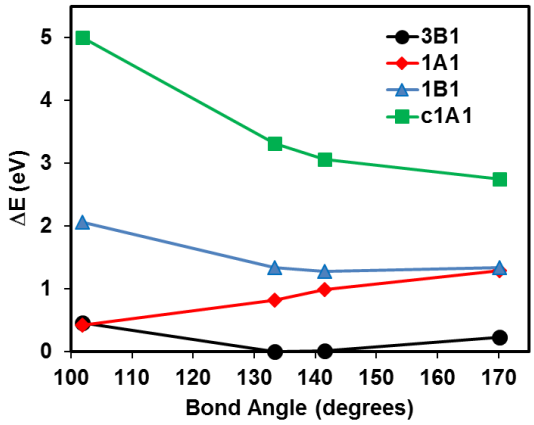

Figure 3.2. Computed adiabatic and vertical excitation energies of CH_2 at the four adiabatic geometries. The PBE0 exchange-correlation functional is used in multistate density functional theory along with the aug-cc-pVQZ basis set. Geometries were optimized using FCI/TZ2P from reference 47.

its minimum at the optimal geometry. The trends can be rationalized by considering the Walsh diagrams.[145] As the bending angle between the AH bonds reaches 180°, the closed-shell ($\tilde{a}\ ^1A_1$) and the open-shell ($\tilde{b}\ ^1B_1$) singlet states become degenerate, denoted by $^1\Delta_g$. At 170°, the optimal geometry of the $\tilde{c}\ ^1A_1$ state, the energy difference between $\tilde{a}\ ^1A_1$ and $\tilde{b}\ ^1B_1$ states is 0.05 eV from MSDFT (Figure 3.2).

Didehydrotoluene (Scheme 3.1) has three isomeric structures (α-2, α-3, and α-4-DHT), which are examples of σ-π diradicals. Unlike the AH_2 dihydride systems above, the closed-shell configurations correspond to π and σ localized zwitterions that do not have significant interactions and are much higher in energy (ca. 1.5 and 3.0 eV above the

ground state, respectively). Therefore, the S-T energy gap is determined by spin coupling between the αβ and βα localized configurations, whose TDF is fully determined by the $M_z = 0$ degeneracy with the $|1,1>$ component. MSDFT results are listed in Table 3.3 along with the SF benchmarks reported by Krylov and coworkers.[137] The ground state of *ortho*- and *para*-DHT are triplet, whereas the singlet state was predicted to be slightly lower in energy than the triplet state in the *meta*-DHT isomer from the SF approaches.[137] Overall, the S-T gaps are reasonably described by MSDFT; however, the small stabilization of the singlet of α-3-DHT was not reproduced. Nevertheless, the trend of relatively smaller energy gap than the other two isomers is obtained. As noted by Bernard et al.,[137] the seemingly good agreement between SF-TDDFT/PBE0 with the CCSD(T) results was in fact an artefact of spin contamination, which is not so lucky with other functionals. Of course, the results from MSDFT are pure spin states. Table 3.3 also lists the results from MOVB, which follows an identical procedure as MSDFT except that dynamic correlation is not included. Even for small S-T energy gaps of these σ-π diradicals, dynamic correlation still makes noticeable contributions.

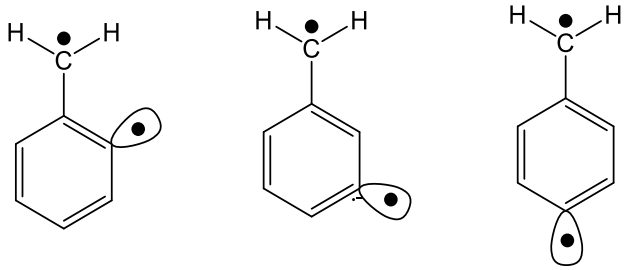

Scheme 3.1. Structures of α-2, α-3, and α-4-didehydrotoluene (DHT).

Table 3.3. Computed singlet-triplet energy gaps (eV) for α-2, α-3, and α-2-didehydrotoluene (DHT) using multistate density functional theory (MSDFT) and mixed molecular orbital and valence bond (MOVB) method along with results from spin flip (SF) approaches. PBE0 is used in DFT methods and cc-pVTZ basis is used in all calculations.[a]

Ground state	Singlet	MSDFT	MOVB	NC-SF-TDA[b]	SF-CCSD(T)[b]
α-2-DHT ($^3B_2$)	$^1A_1$	0.172	0.144	0.230	0.247
α-3-DHT ($^3B_2$)	$^1A_1$	0.024	0.031	-0.025	-0.066
α-4-DHT ($^3B_2$)	$^1A_1$	0.175	0.098	0.248	0.250

a. The total energies for the 2, 3, and 4 diradical isomers are, respectively, -269.98684, -269.98639, -269.98630 a.u. from MSDFT/PBE0/cc-pVTZ, and -268.55012, -268.54904, and -268.54927 a.u. from MOVB/cc-pVTZ.

b. Reference 137.

Note that the computational accuracy of MSDFT on multiplet splitting is dictated by the specific functional used since the spin-coupling given by the transition density functional is uniquely determined for a given KS functional used to characterize the determinant states. In comparison with SF-TDDFT, the states from MSDFT are pure spin states, whereas the SF approach does not guarantee energy degeneracy of spin-multiplet components. This difference contributes to the difference in computational results in comparison with experiments or high-level reference data. Another difference is the treatment of configuration coupling in that the TDF correlation energy in MSDFT is different from that in the NC-SF-TDDFT, whereas it is not present is conventional SF-TDDFT.

3.5. Conclusions

In summary, the multistate density functional theory (MSDFT) is extended to describe spin multiplets and excitation energies of atoms and molecules. In MSDFT, spin multiplet components are expressed as eigenfunctions of both $\hat{S}^2$ and $\hat{S}_z$ operators, and their energy degeneracy in the absence of an external magnetic field is exactly reproduced. MSDFT is a hybrid approach, taking advantage of both wave function theory and density functional theory. Consequently, the wave functions, electron densities and energies for ground and excited states and for different spin multiplet components are treated on the same footing. Valence excitation energies of first row atoms, Be through O, and the isovalent hydrides, including CH_2, NH_2^+, SiH_2, and PH_2^+ molecules, have been evaluated using MSDFT along with the PBE0, PBEC and M06-HF density functionals. Energetic results are found to be in accord with experiments, and of comparable or better accuracy in comparison with SF-TDDFT for singlet-triplet energy splittings. OF the atomic states considered, the mean average deviation is about 0.3 eV from experiments, whereas it is 0.1 eV for the hydride states relative to the SF-CCSD(T) results. Importantly, a key result of this study is that for cases in which the high-spin component can be determined separately by KS-DFT, with a given exchange-correlation functional (LDA, GGA or hybrid), the associated transition density functional in the multistate approach, representing configuration coupling of spin-localized states, can be rigorously determined. This is possible by enforcing the energy degeneracy condition of spin multiplet components. Therefore, even though the exact functional dependency ($E^{\mathrm{TDF}}[\rho_{AB}]$) on the transition density ρ_{AB} is not fully known, its value that defines the

energy of the low-spin components can be evaluated exactly based on the exchange-correlation energies of the relevant KS determinants. Therefore, the numerical results may be explored to design and optimize transition density functionals for configuration coupling in multiconfigurational DFT.

Chapter 4. Perturbation Approach for Computing Infrared Spectra of the Local Mode of Probe Molecules

Adapted with permission from R.-J. Xue, A. Grofe, H. Yin, Z. Qu, J. Gao, and H. Li, J. Chem. Theory Comput. **13**, 191 (2016).

This work was performed in collaboration with Rui-jie Xue and Yin He. We thank Martin A. Suhm and Michal Fárník for providing the raw experimental data.

4.1. Introduction

Molecular vibrations and infrared spectroscopy of small chromophore probes embedded in molecular clusters, solutions, and biomacromolecules have been widely used to investigate solute-solvent interactions, hydrogen-bonding dynamics, and the local electric fields in enzymes.[152-160] Vibrational frequency shifts are especially sensitive to the local electrostatic environment, which can be easily and accurately measured. Thus, the study of vibrational frequency shifts is an efficient way to analyze the local structure and its consequent electric field.[153, 161] Furthermore, measurements of the time-dependent frequency fluctuations or spectral diffusion can provide dynamic information, and it is useful to carry out condensed-phase simulations of solutions or biomacromolecules. To this end, a range of computational methods have been developed for the study of molecular vibration in condensed phases, including path integral simulations.[155, 162, 163] Still, it is a challenging task to determine the instantaneous vibrational frequencies of probe molecules that include nuclear quantum effects on the fly in molecular dynamics simulations.[152, 155, 164] In this study, we present a combined quantum mechanical and

molecular mechanical (QM/MM) perturbation approach to efficiently and accurately determine the vibrational frequency of a probe molecule to construct its linear and two-dimensional infrared (2D-IR) spectra.[165, 166]

We use the HCl-water cluster system to illustrate and validate the present first-order quantum vibration perturbation (QVP1) approach because strong hydrogen-bonding and dispersion interactions are important, and because it has been extensively investigated experimentally[167-178] and theoretically.[176-204] Although this appears to be a small test case, it is in fact challenging because of the strong bond-dissociation character in the oscillator mode. We emphasize that the QVP1 method is equally efficient for condensed-phase simulations as in a combined QM/MM approach.[205] This is illustrated on the vibrational spectral shifts of the carbonyl stretch mode of acetone in aqueous solution. The C=O stretch vibration is widely used as the probe to the secondary structure of proteins,[206, 207]

Experimentally, Suhm and coworkers reported the first IR spectrum of HCl-water clusters,[167, 168] and found that a minimum of four water molecules is required for HCl dissociation. Recently, Havenith and coworkers confirmed that the broad band at 2675 cm^{-1} is due to the dissociated cluster, $H_3O^+(H_2O)_3Cl^-$.[208] On the theoretical side, Born-Oppenheimer molecular dynamics (BOMD) simulations with DFT-based potentials have been used to model $HCl(H_2O)_n$ (n=1 to 4) clusters.[189, 191-196, 198, 209] Marx and coworkers[198] obtained the IR spectra of the HCl-water clusters using the BLYP density functional. A sequential solvation process was proposed to account for the HCl dissociation mechanism, involving the interplay of quantum tunneling and thermal fluctuations from path integral simulations.[184, 188, 194-196] Employing a semiempirical

PM3-MAIS potential, Lin and Paesani extended the investigation to larger clusters up to n = 21.[177] The IR spectra assignment was analyzed on the basis of atomic velocity autocorrelation functions, in which the vibrational quantum effects were ignored.[177] In this regard, Paesani and coworkers have developed highly accurate empirical potential energy functions for liquid water and solutes.[210-212] Various approximate methods are available to account for the time-dependent nuclear quantum effects, including linearized semiclassical initial value representation (LSC-IVR),[213-215] centroid molecular dynamics,[164, 216-222] and ring-polymer molecular dynamics.[221, 223-227] One can, of course, solve numerically the vibrational Schrödinger equation.[164, 216-222] Mancini and Bowman[201-204, 228] employed diffusion Monte Carlo simulations to investigate the high-frequency fundamental modes of HCl-water clusters. Good agreement was observed between the calculated vibrational frequencies and experimental peak positions when the delocalized zero-point vibrational motion was taken into account.[201]

The IR signature of H_3O^+ in the dissociated configuration of $H_3O^+(H_2O)_3Cl^-$ was investigated using vibrational configuration interaction (VCI) with the local monomer (LMon) potential energy surface,[228] providing peak positions and intensities. The VCI calculations employed eight states for each vibrational mode, coupled to up to four other modes, on 10G integration points per mode. Although these studies provided significant insights on mode coupling and peak positions of H_3O^+ for a single fixed water-Cl^- configuration, the method does not provide spectral line shape and is too time-consuming to obtain time-dependent frequencies in dynamics simulations.

Explicit quantum mechanical treatments of both the nuclear motion and the potential energy surface are required to understand the solute-solvent interaction dynamics in 1-D and 2-D vibrational spectroscopic experiments. In principle, path-integral molecular dynamics employing an on-the-fly QM potential can be used; however, the high computational costs limit its broad applications, especially when excitation involving higher vibrational states are investigated. In practice, empirical spectroscopic maps that relate the frequency change to the local electric field have been widely used. The method has been shown to be quite reliable for systems dominated by electrostatic interactions.[152-154, 229, 230] However, the electrostatics-based spectroscopic map does not fully take into account exchange and dispersion interactions, nor explicit polarization effects and charge transfer contributions. Thus, large deviations were found in simulations of N-methyl acetamide (NMA) in $CDCl_3$ solution in which dispersion forces are dominant.[190] To this end, combined QM/MM methods, in which the probe molecule is treated explicitly by electronic structure theory, provide the most general, efficient and systematic approach to represent the potential energy surface.[231, 232] It also avoids the need to fit a secondary dipole moment surface that is typically inconsistent with the electrostatic properties of the empirical potential function.[152, 155, 164, 228] The instantaneous vibrational energy levels can be determined by solving the vibrational Schrödinger equation for a given mode or coupled modes based on the QM/MM potential,[164, 231] but the increased computational costs prevent it from being effectively used to obtain the frequency-frequency correlation function (FFCF). Thus, it is useful to develop computationally efficient methods to accurately determine the time-dependent vibrational

frequencies of a specific vibrational mode of a probe oscillator in solution and biological systems.

In this Chapter, we describe a perturbation approach to efficiently determine the instantaneous vibrational frequency of one or two specific target modes. The method is based on quantum vibrational perturbation (QVP) theory by means of potential-optimized discrete variable representation (PODVR).[233, 234] The key in the QVP method is to estimate the vibrational energy shift of the solute (probe) molecule induced by interactions with the solvent environment without the need to solve the vibrational Schrödinger equation.[235, 236] The QVP method incorporates nuclear quantum effects of the vibrational probe as well as the influence of dynamic fluctuations of the environment, and it can be applied to large molecular systems directly in molecular dynamics simulations with a combined QM/MM potential. The QVP method is illustrated and validated by an application to the small yet challenging HCl-water clusters to determine the IR spectra in the HCl stretching region.

4.2. Methods

In the present QVP approach, the energy of each vibrational state of the oscillator is obtained by treating the solvent fluctuation as a perturbation, $\Delta H(Q,R)$, to the reference configuration $H^0(Q,R_0)$, where Q and R refer to solute and solvent coordinates, and R_0 is the coordinates at the referenced state. Consequently, the instantaneous transition frequency from the ground vibrational state ($\upsilon = 0$) to the first excited state ($\upsilon = 1$) for the mode of interest is given by

$$\omega_{10}(t) = \omega_{10}^{o} + \Delta\omega_{10}(t) \tag{4.2.1}$$

where ω_{10}^{o} is the vibrational frequency of the reference state, which is the minimum-energy structure of the ClH–OH_2 complex. In equation 4.2.1, the frequency shift $\Delta\omega_{10}(t)$ is related to the perturbation energies of the instantaneous structure at time *t*:

$$\Delta\omega_{10}(t) = \frac{\Delta V_1(t) - \Delta V_0(t)}{\hbar} \tag{4.2.2}$$

where $\Delta V_0(t)$ and $\Delta V_1(t)$ are the perturbation energies for the ground and first excited states of the quantum oscillator in the bath of a given solvent configuration.

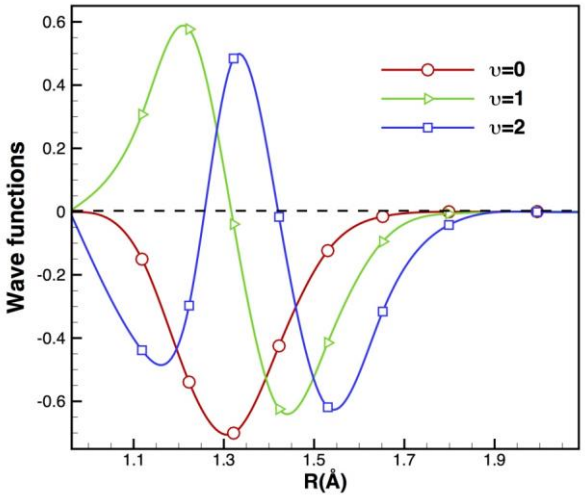

Figure 4.1. Computed vibrational wave functions of the ground, and the first and second excited states of the HCl stretch mode in the optimized HCl(H_2O) structure. Discrete variable representation (DVR) at the eight optimized grid points are indicated.

Specifically, we first solve the vibrational Schrödinger equation for the reference structure defined by $H^0(Q, R_0)$ to yield the vibrational wave functions φ_υ, based on which the optimal number of PODVR points is obtained.[234, 237] For the ClH–OH_2

complex, we found that just eight PODVR points are sufficient to obtain convergent energies and wave functions for the lowest three vibrational states. They are depicted in Figure 4.1. Then, we use perturbation theory to determine the energy shifts for each vibrational level relative to that of the reference state. Importantly, the perturbation energies converge quickly, and the first order approximation (QVP1) is sufficient in the present test cases (see below).

In the PODVR basis $\{\chi^2(q_i;R_0), i=1,\cdots,8\}$ over the discrete points along the HCl stretching mode for the reference state, R_0, the first order perturbation energy for state υ is given by

$$\begin{aligned}\Delta V_\upsilon(t) &= \int dq \Delta H(q,R[t])\,|\varphi_\upsilon(q;R_0)|^2 \\ &= \sum_{l=1}^{8} \Delta H(q_l,R[t]) c_{\upsilon l}^2 \chi^2(q_l;R_0)\end{aligned} \tag{4.2.3}$$

where q_l is the coordinates of the *l*th PODVR point, $\{c_{\upsilon i}\}$ are the optimized and normalized coefficients for state υ in the PODVR basis, and $\Delta H(q_l,R[t])$ is the perturbation energy corresponding to the chromophore at the discrete point q_l and the instantaneous bath coordinates at $R[t]$ at time *t*. Equation 4.2.3 is based on the separation of inter- and intra-molecular motions, which ignores the nuclear quantum mechanical effects on their coupling. This approximation is justified for situations in the present study (except when HCl dissociation occurs with four water molecules) and is valid for most applications in biological systems, where the vibrational frequency of the probe molecule is designed to clearly separate from the bath modes. Nevertheless, coupling to higher quanta of bath modes could be important and a procedure developed by Skinner

and coworkers can be applied here to treat such situations.[163] In practice, $\Delta H(q, R[t])$ can be evaluated using a combined QM/MM potential, or by a mixed fragmental QM model in which the solute and its nearest neighbors are described by a high-level theory embedded in the solvent environment to model long-range electrostatic effects.[238] In the latter case, short-range repulsion, dispersion and charge transfer effects between the oscillator and solvent molecules in close proximity are naturally included in the QM model. For the present HCl-water clusters, the entire system is treated quantum-mechanically using two QM methods: M06-2X[239]/cc-pVTZ and CCSD(T)-F12B[240-242]/cc-pVTZ.

Equations 4.2.2 and 4.2.3 show that the present QVP1 method can be extremely efficient for computation of vibrational frequencies, which involve two weighted averages of the perturbation term. Thus, the computational cost is equivalent to that needed to determine the perturbation energy at the discrete points without explicitly solving the vibrational Schrödinger equation. The weighting coefficients in equation 4.2.3, defined by $\{\omega_i = c_{\upsilon i}\chi^2(q_i, R_0), \upsilon = 1,2\}$, are predetermined for the chromophore oscillator in the reference structure, and optimized to represent the vibrational wave function in the PODVR method. Higher order perturbation terms can be used if greater computational accuracy is desired or becomes necessary.

To quantify convergence of the present perturbation strategy, we selected 40 structures from the molecular dynamical trajectory of $HCl(H_2O)$ at equal interval, and determined the exact vibrational frequencies by solving numerically the Schrödinger equation and those estimated by the QVPn method up to the fourth-order perturbation (n

= 1 – 4). The results are compared in Figure 4.2 spanning a range of vibrational frequency from 2500 cm^{-1} to 2775 cm^{-1}. Figure 4.2 reveals that while the first-order perturbation approach QVP1 has a good agreement with the exact result in the medium range of 2600-2700 cm^{-1}, increased deviations are observed at higher and lower frequencies with an average error of 3.0 cm^{-1}. As the order of perturbation increases, the computation accuracy increases sharply to root-mean-square deviations of 0.1, 0.04 and 0.04 cm^{-1} for the second, third, and forth-order perturbation theory, respectively. However, higher vibration excited states are needed to obtain high-order perturbation energies, which translate to more discrete points in the PODVR evaluation. Since the frequency shifts are relatively large in the present test cases, the first-order perturbation QVP1 is used throughout.

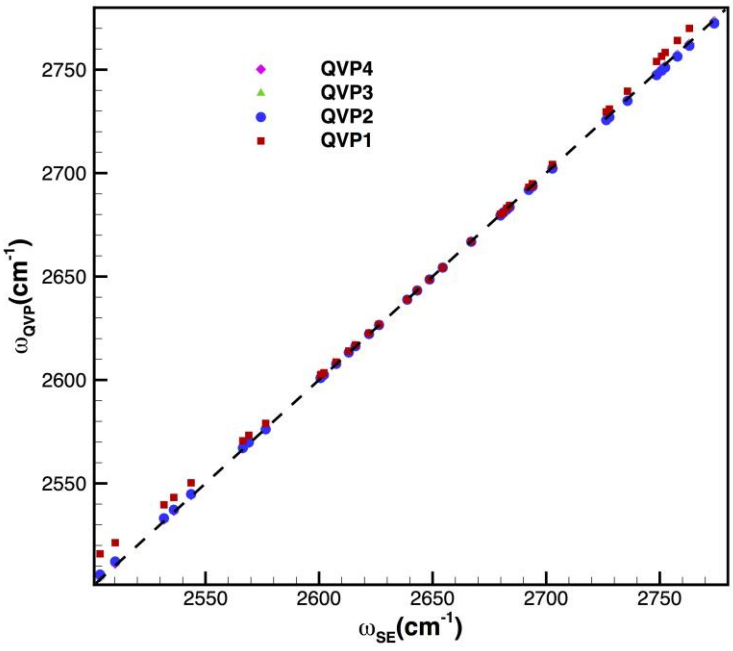

Figure 4.2. Correlation of the exact and the QVP vibrational frequencies for HCl in 40 complex structures from an ab initio molecular dynamics trajectory of the H_2O…HCl cluster using CCSD(T)-F12b/cc-pVTZ-F12. The exact results are obtained by solving the vibrational Schrödinger equation (abscissa) for each complex structure, whereas up to the fourth-order perturbation is used in the quantum vibrational perturbation (QVP) approach (ordinate). The black dashed line represents a perfect match.

4.3. Computational Details

Born-Oppenheimer molecular dynamics simulations were performed using the meta-GGA M06-2X density functional theory with the cc-pVTZ basis for HCl(H_2O) and using BLYP density functional theory augmented by dispersion corrections[88,89] for other cases with a plane wave basis set[86,87,243] For each cluster, the dynamics simulations were carried out at 200 K for a total of 25 ps with an integration step of 30 au (0.72 fs). Additional details of the ab initio simulation procedure are given in the SI. For accuracy in the computed vibrational frequency, all the perturbation energies were determined using the M06-2X/cc-pVTZ and CCSD(T)-F12b/cc-pVTZ-F12 methods.[244] Basis set superposition errors (BSSE)[245] were corrected following the counter poise scheme. Note that as the number of water increases in the HCl$(H_2O)_n$ clusters, HCl dissociation is observed when *n* is 4. This is consistent with the aggregation-induced dissociation mechanism[173, 191] in previous simulations.[191, 193-195, 208, 246]

For comparison, we have determined the linear absorption line shape by classical and mixed quantum/classical approaches.[152, 155] In the classical approach, the line shape function is computed by Fourier transform of the autocorrelation function of the total molecular dipole moment from classical molecular dynamics simulations

$$I_{cl}(\omega) = Q_H(\omega)\int d\omega < \mu(0)\cdot\mu(t) > e^{-i\omega t} \qquad (4.3.1)$$

where $Q_H(\omega)$ is the harmonic quantum correction factor,[247, 248] and the brackets specify a classical statistical mechanical average. In the mixed quantum/classical method,[152, 155] where the HCl vibrational mode is treated quantum mechanically and all other degrees of freedom are modeled classically by molecular dynamics, a key quantity of interest is the $0 \rightarrow 1$ transition frequency and its dependence on the environment (equation 4.2.1). Then, within the Condon approximation, the magnitude of the vibrational transition moment is assumed to be independent of the bath fluctuations,[152] and the semiclassical absorption line shape can be written as

$$I_{sc}(\omega) = \int dt e^{-i\omega t} < e^{i\int_0^t d\tau \omega_{10}(\tau)} > e^{-t/2T_1} \tag{4.3.2}$$

where T_1 is the vibrational energy relaxation time (224 fs), which is estimated following the work of Straub and co-workers[249-252] by computing the classical autocorrelation function of the force along the H-Cl bond. To evaluate the average in equation 4.3.2, the time evolution for $\omega_{10}(t)$ are computed using the QVP1 method on the classical molecular dynamics trajectory. Equation 4.3.2 can be written in terms of cumulant expansion at the second-order truncation:

$$I_{cum}(\omega) = \int dt e^{-i(\omega - <\omega_{10}>)t} e^{-\int_0^t d\tau (t-\tau) C(\tau)} e^{-t/2T_1} \tag{4.3.3}$$

where $<\omega_{10}>$ is the average transition frequency, and $C(t)$ is the frequency-frequency time-correlation function given by

$$C(t) = <\delta\omega(0)\delta\omega(t)> \tag{4.3.4}$$

where $\delta\omega(t) = \omega_{10}(t) - <\omega_{10}>$.

4.4. Results and Discussion

We first present results on the hydrogen chloride-water clusters to demonstrate the performance of the quantum vibrational perturbation approach for determining on-the-fly vibrational frequencies. Here, the full system is represented by an electronic structure method. Then, we illustrate the applicability of the QVP method in condensed-phase simulations, making use of the carbonyl stretching mode of acetone in water as an example. In this case, combined QM/MM molecular dynamics simulations are performed to evaluate the perturbation energy using a semiempirical Hamiltonian.

4.4.1. HCl-Water Clusters

The computed and experimental IR spectra in the HCl stretching region of the bimolecular complex HCl(H_2O) are displayed in Figure 4.3. In this discussion, we first address nuclear quantum effects on the computed frequency, and then, examine a hybrid procedure to increase the accuracy of the results, making use of the M06-2X trajectory. Figure 4.3.a displays the line shape functions using the classical molecular dipole autocorrelation function (DAF) in blue (scaled by the harmonic quantum correction factor), and using equation 4.3.2 based on the QVP1 transition frequencies in green. The spectrum determined from the DAF shows a series of side peaks with an interval of about 50 cm^{-1}, attributed to the coupling with rotations of the water molecule about the H-Cl axis. This effect is not included in the instantaneous frozen-bath approximation in the QVP1 model. The maximum peak position from the QVP1 method is located at 2653 cm^{-1}, red-shifted by 185 cm^{-1} from the strongest peak position (2838 cm^{-1}) displayed on the spectrum based on the classical DAF. Since M06-2X/cc-pVTZ was used in both

approaches, consistent with the dynamic trajectory, the difference between the two methods is primarily due to nuclear quantum effects of the oscillator, which clearly have significant contributions to the computed vibrational frequencies in Figure 4.3.a. Nevertheless, the full widths at half maximum (FWHM) of the spectrum peak are similar from both methods (21 and 23 cm^{-1}, respectively).

Figure 4.3.b compares the results obtained using three different electronic structure methods; M06-2X (green line), CCSD(T)-F12b (red line), and a composite of M06-2X spectral shift and the CCSD(T)-F12b frequency. In the latter approach, the CCSD(T)-F12b frequency for the reference state is used, but the spectral shift due to dynamic fluctuations of the solvent is determined at the M06-2X level using QVP1. We designate this method as CCSD(T)/M06 in Figure 4.3.b, which significantly reduces the computational costs compared with that when the perturbation theory is also carried out at the CCSD(T)-F12b level. Figure 4.3.b shows that the maximum peak position from QVP1 using CCSD(T)-F12b is only 14 cm^{-1} greater than the experimental value (2723.5 cm^{-1}).[167, 168] The M06-2X frequency in the $HCl(H_2O)$ complex is blue-shifted by 84.6 cm^{-1} from the coupled-cluster value, and this is mainly due to the difference in the reference state between the two methods; 80.6 cm^{-1} = 2650.5 cm^{-1} (CCSD(T)-F12b) - 2569.9 cm^{-1} (M06-2X). Thus, the solvatochromic shifts are not very sensitive to the quantum chemical models used, here, differing only by 4 cm^{-1}. Clearly, it can be a major time-saving approach to use density functional theory to estimate the spectral shift, but the reference frequency value is evaluated using coupled cluster theory (equation 4.2.1) since the latter only needs to be computed once. As the computational cost of the QVP method

is equivalent to that required to determine the perturbation energy at the discrete points, allowing the instantaneous vibrational frequency of the oscillator to be determined on-the-fly of dynamics simulations. Indeed, the composite approach, employing the CCSD(T) zeroth order frequency (reference state) and QVP1 frequency shift from M06-2X (blue curve in Figure 4.3.b), yields a maximum peak position at 2725 cm^{-1}, only 13 cm^{-1} different from the CCSD(T)-F12b value (2738 cm^{-1}). Interestingly, the composite result is in better accord with experiment than CCSD(T)-F12b, perhaps due to fortuitous error cancellations. Furthermore, the predicted FWHM from the composite strategy is 21 cm^{-1}, also in good agreement with experiment (18 cm^{-1}),[167, 168] and consistent with pure CCSD(T)-F12b and M06-2X calculations. The agreement between theory and experiment both in peak position and in line shape suggests that the QVP1 composite approach can be used for studying IR spectra of condensed-phase and biomolecular systems.

In Figure 4.3.c, we compare the distribution of instantaneous vibrational frequencies (blue) computed along an MD trajectory with the line shape function (equation 4.3.3) determined at the CCSD(T)-F12b/cc-pVTZ-F12 level (red). Although the average peak positions are the same, the statistical distribution of the computed frequencies is clearly not an adequate approximation to the spectral line shape due to motion narrowing effects. Similar features were found in the study of HOD vibration in H_2O and in D_2O employing a polarizable empirical potential for water.[13]

The 2D pump-probe spectra for the HCl stretching vibration in HCl(H_2O) are computed using the instantaneous vibrational frequencies determined by the CCSD(T)/M06-2X composite strategy along with t_2 evolution (additional details are

given in the SI). In Figure 4.3, the ω_1 axis represents the pump pulse, while the ω_3 axis specifies the probe pulse. The projection on ω_3 is the dynamical line shape both for the vibrational bands of the 1-0 resonance (red) and the 2-1 resonance (blue). The 2D IR spectra are displayed in Figure 4.3 for t_2 waiting times of 0, 302, 504 and 705 fs. At t_2 = 0 fs, the spectrum is diagonally elongated and anti-diagonally narrowed, which demonstrates the anisotropy of the two vibrational bands and indicates a strong correlation of the vibrational bands. The anti-diagonal direction is broadened and the nodal slope (separating the positive region of the 1-0 resonance from the negative region of the 2-1 resonance in the 2D spectra and the slope lines are shown as the blue dashed lines in Figure 4.3) decreases as t_2 increases, indicating reduction of correlation. At t_2 = 705 fs, the nodal slope is closer to zero, where the coupling of the two vibrational bands vanishes.

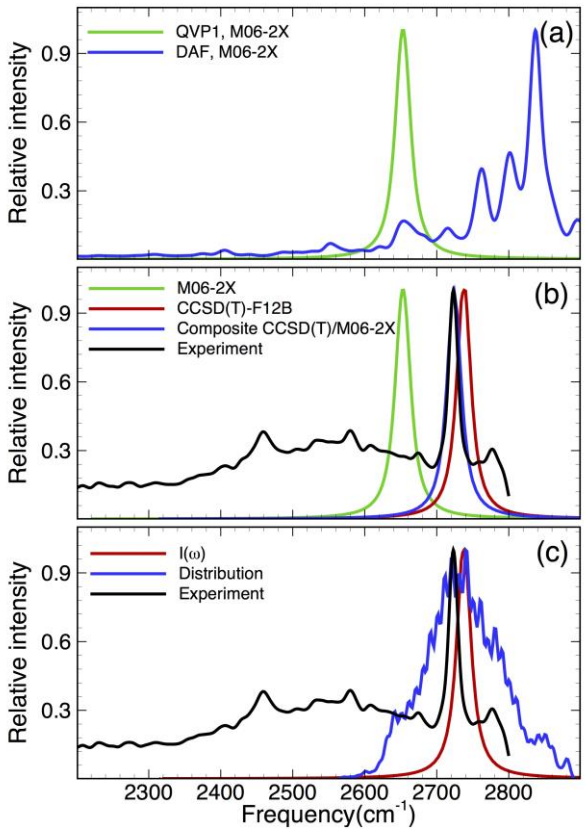

Figure 4.3. Normalized IR line shapes from experiment (black) and computations for the HCl stretching vibrational mode in the HCl(H_2O) complex. (a) The spectrum obtained by Fourier transform of DAF (equation 4.3.1) is given in blue, and that from instantaneous QVP1 frequencies (equation 4.3.2) is displayed in green, both at the M06-2X/cc-pVTZ level. (b) Spectral line shapes determined by the second-cumulant expression based on the frequency-frequency time correlation function (equation 4.3.3) are shown at the CCSD(T)-F12b (red) and M06-2X (green) levels along with the composite of CCSD(T)-F12b frequency for the reference state and M06-2X frequency shifts (blue). The distribution of computed H-Cl stretching frequency (blue) at the CCSD(T)-F12b level is illustrated in (c) along with the corresponding spectral line shape function (red) and the experimental spectrum (black).

Table 4.1. Computed HCl stretching vibrational frequency ω_{Cl-H} and the shift $\Delta\omega_{Cl-H}$ of the HCl(H_2O) complex using harmonic normal mode analysis (NMA), Fourier transform of the dipole autocorrelation function (DAF) and the spectral expansion (equation 4.3.3) of the frequency-frequency time correlation function from the QVP1 method, along with the experimental value. Vibrational frequencies are given in cm^{-1}.

	Method	Basis Set	ω_{Cl-H}	$\Delta\omega_{Cl-H}$ [a]
	HF	Q[b]	3033.0	309.5
NMA[15]	MP2	T[b]	2791.0	67.5
	CCSD(T)	D[b]	2782.0	58.5
DAF	M06-2X	cc-pVTZ	2837.6	114.1
	M06-2X	cc-pVTZ	2653.0	-70.5
QVP1	M06-2X+ CCSD(T)-F12b	cc-pVTZ+cc-pVTZ-F12[c]	2724.8	1.3
	CCSD(T)-F12b	cc-pVTZ-F12	2737.6	14.1
EXP[15,16]			2723.5	

[a] $\Delta\omega_{Cl-H} = \omega_{Cl-H} - \omega_{\exp}$.

[b] aug-cc-pVXZ, X=D,T,Q.

[c] M06-2X/cc-pVTZ+CCSD(T)-F12b/cc-pVTZ-F12

The 2D IR spectra provide a direct measure of the anharmonicity of the probe mode. Figure 4.4 indicates that the anharmonic frequency shift from the QVP1 approach is 140 cm^{-1} for H-Cl stretching vibration in the HCl(H_2O) complex, which is the difference between the central frequencies at positive (red) and negative (blue) peak regions on the ω_3 axis. In comparison with the anharmonic frequency shift of 104 cm^{-1} estimated for an isolated HCl molecule, hydrogen bonding interactions as well as dispersion contributions further increase anharmonicity in the HCl(H_2O) cluster. It is interesting to note that 1-0 and 2-1 transitions for the HCl stretching mode in HCl(H_2O)

are red-shifted, respectively, by 161 and 197 cm^{-1} relative to an isolated HCl. Apparently, hydrogen bonding interactions have a greater effect on the higher vibrational energy levels than the ground state.

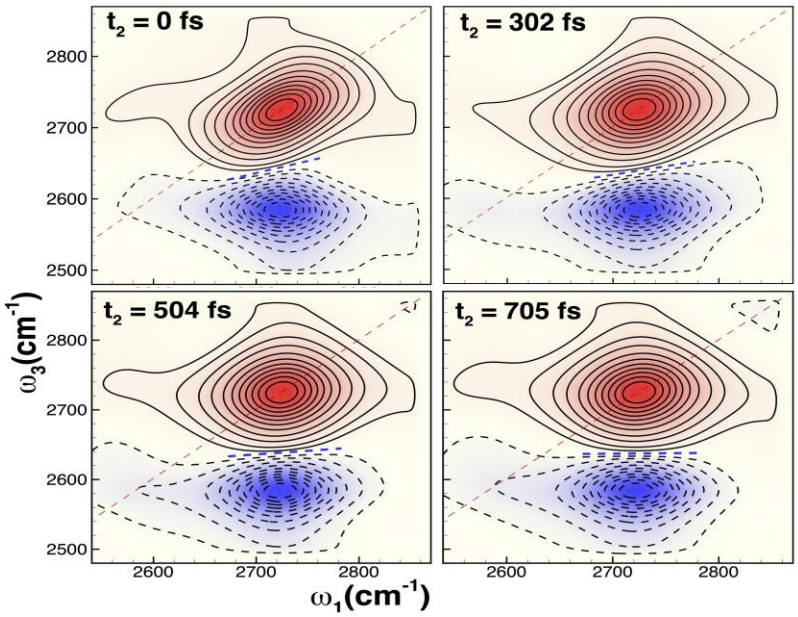

Figure 4.4. The 2D pump-probe spectra of the HCl stretching vibration in the $HCl(H_2O)$ complex are given at the evolution time t_2 equaling to 0 fs, 302 fs, 504 fs and 705 fs respectively. See text for specific details.

There are two HCl stretching vibrations in $(HCl)_2(H_2O)$. Here, we focus on the HCl stretching mode in which the hydrogen atom is hydrogen-bonded to the oxygen of water. Figure 4.4 depicts the line shape of the main peak, which is in good agreement with the experimental peak.[167, 168] The peak position is centered at 2634 cm^{-1} which is 54 cm^{-1} greater than the experimental value. The calculated line shape is similar to that from experiment, indicated by the blue arrow of the spectrum in red. For this system, the time-dependent trajectories, including the $HCl(H_2O)_2$ cluster below, were sampled at the

BLYP/Plane wave level, but the vibrational frequencies were determined by using the composite QVP1 strategy.

Table 4.2. Computed H-Cl stretching vibrational frequencies (cm^{-1}) for (HCl)2(H2O) by solving two independent one-dimensional (E_{1D}) Schrodinger equation and a two-dimensional (E_{2D}) vibrational Schrodinger equation. The potential energy surfaces were determined using M06-2X/cc-pVTZ. Q_1 and Q_2 represent, respectively, the H-Cl stretch associated with the HCl molecule directly hydrogen-bonded to water and hydrogen-bonded to the probe HCl molecule (Figure 4.4).

Mode	E_{1D}	E_{2D}	$\Delta\nu$
Q_1	2617.0	2612.3	4.7
Q_2	2692.6	2693.7	-1.1

The present QVP method is applied to a single mode of interest, which ignores vibrational mode coupling in order to increase computational efficiency. For applications to biological systems, in which the vibrational frequency of the probe molecule (e.g., chromophores with triple bond or C-D stretch), the effect is expected to be small. However, because of the proximity of two similar HCl vibrations, mode coupling could be important. To address this question, we have determined the frequencies both HCl molecules in the optimized $(HCl)_2(H_2O)$ complex (see Figure 4.5) by solving one-dimensional and two-dimensional vibrational Schrodinger equations, *i.e.*, one based on the potential energy surface of independent modes, and the second employing the full potential of the two modes, both at the M06-2X/cc-pVTZ level (Table 4.2). Mode coupling is included in the latter approach. It was found that the mode corresponding to the HCl molecule directly hydrogen-bonded to water is lowered by 4.7 cm^{-1} due to coupled interactions with the second HCl molecule, whereas the stretch frequency of the

other HCl is enhanced by 1.1 cm^{-1}. Thus, the effect due to mode coupling is not significant in this case.

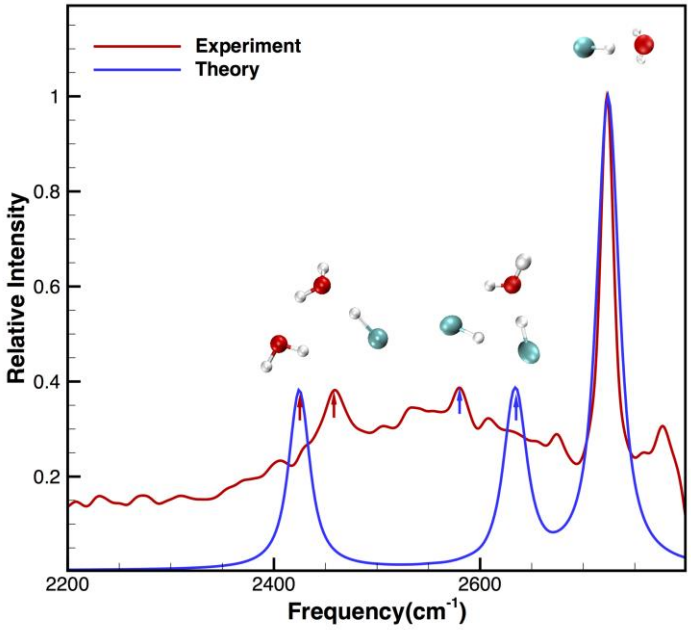

Figure 4.5. The experimental spectra and the overall computed HCl stretching vibrational spectra for a mixture of $(HCl)(H_2O)$, $(HCl)_2(H_2O)$ and $(HCl)(H_2O)_2$ clusters with weighting factors of 1, 0.41 and 0.46 for the relative intensities based on the experimental intensities. The blue and red arrows specify the HCl stretching mode in the $(HCl)_2(H_2O)$, $(HCl)(H_2O)_2$ clusters, respectively, and the strongest peaks correspond to that in the $HCl(H_2O)$ complex. The latter was sampled by M06-2X/cc-pVTZ, whereas the remaining systems were sampled using BLYP-D Born-Oppenheimer molecular dynamics simulations.

The peak position of the $HCl(H_2O)_2$ stretching vibrational mode of the 1:2 cluster, illustrated in Figure 4.5, is found at 2424 cm^{-1}, which is close to the peak at 2460 cm^{-1} found experimentally.[167, 168] The computed line shape for $HCl(H_2O)_2$ complex is somewhat narrower than that from experiment, highlighted by the red arrows in Figure 4.4.

Finally, we note that Figure 4.5 was constructed by summing up the individual HCl stretching vibrational spectra of the $(HCl)(H_2O)$, $(HCl)_2(H_2O)$ and $(HCl)(H_2O)_2$ clusters with weighting factors for relative intensities of 1, 0.41 and 0.46, respectively. Both the peak positions and line shapes are in reasonable agreement with the experimental spectra, which further support our assignments of those peaks as the HCl stretching mode in the $(HCl)(H_2O)$, $(HCl)_2(H_2O)$, $(HCl)(H_2O)_2$ clusters, respectively.

4.4.2. Acetone in Aqueous Solution

To illustrate the general applicability of the QVP method in condensed-phase simulations, we carried out "on-the-fly" vibrational frequency for the carbonyl stretching mode of acetone in aqueous solution. Combined quantum mechanical and molecular mechanical (QM/MM) potential[205, 253] is employed, in which the chromophore is approximated by the semiempirical Austin Model 1 (AM1)[254] Hamiltonian, and the solvent is represented by the TIP3P model for water. A single solute molecule is embedded in a cubic box of 467 water molecules using the isothermal-isobaric (NPT) ensemble at 25 ^oC and 1 atm. The time-step in the simulation is 1 fs and a convergent QVP spectrum of C=O vibration is obtained using a 50 ps trajectory. All computations are carried out using CHARMM. Here, the instantaneous vibrational frequency of the carbonyl stretch in water is determined using the composite approach described in the previous section, where the reference state is determined at a high level of theory, whereas the perturbation energy is obtained at the combined QM/MM level to account for solvent effects. In particular, the C=O vibrational wave functions for the first three vibrational states of an isolated acetone molecule in the gas phase are determined using

the potential energy curve from CCSD(T)-F12/cc-pVTZ-F12 calculations along the C=O normal mode coordinate. The 0→1 transition frequency is estimated to be 1776 cm^{-1}, in reasonable agreement with the experimental value of 1738 cm^{-1} in the vapor phase, and the small difference of +38 cm^{-1} will be fully transferred to the solution result.

Figure 4.6 displays the computed vibrational spectra for the C=O stretching mode of acetone in water using the Fourier transform of the dipole autocorrelation function (DAF) (blue curve) and that from the cumulant expansion of the QVP1 frequency fluctuation autocorrelation function (red curves), along with the experimental results (black curve).[255] The peak position at 1741 cm^{-1} from the QVP1 method represents a solvent-induced red shift of -35 cm^{-1}, which may be compared with a solvent effect of -41 cm^{-1}, corresponding to a maximum peak position at 1697 cm^{-1}. The agreement indicates that the AM1 model used in combined QM/MM simulations can capture the large bulk of solvation effects. In addition, the calculated FWHM (14.8 cm^{-1}) is in good accord with the experiment (15.1 cm^{-1}).[255,256] On the other hand, the maximum peak position is found at 1414 cm^{-1} by Fourier transform of DAF, which is red-shifted by -30 cm^{-1} from the corresponding gas-phase value. The AM1 Hamiltonian severely underestimate the carbonyl stretch frequency of acetone by 294 cm^{-1} compared with experiment, which is fully translated into the condensed-phase results by direct application of the molecular dipole autocorrelation function. Since the Fourier transform of DAF includes anharmonicity and captures the same solvent effect as that in the QVP1 calculations, the small difference of 5 cm^{-1} between the two methods is attributed to nuclear quantum effects. The difference between the QVP1 and DAF results also illustrates the use of the

composite approach to effectively correct errors in the low-level QM/MM representation of the absolute vibrational frequency.

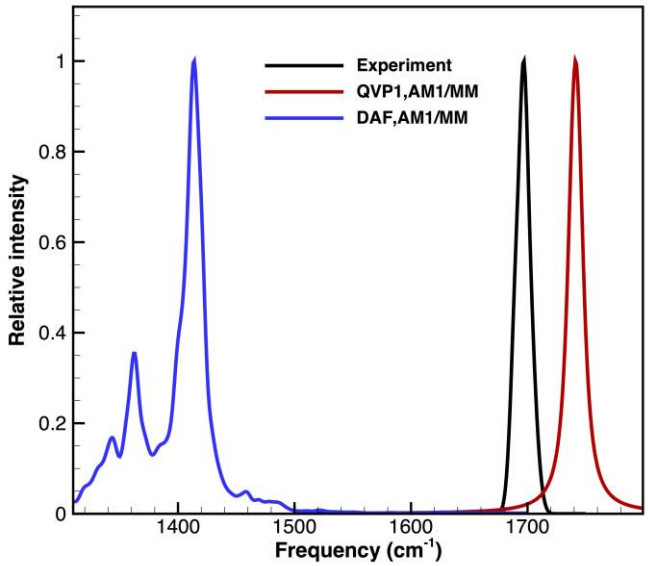

Figure 4.6. Experimental (black) and computed vibrational spectra of the carbonyl stretching region of acetone in water. The spectrum from the first-order quantum vibration perturbation (QVP1) calculation employing a composite of the CCSD(T) reference frequency and a QM(AM1)/MM perturbation potential is shown in red, and that from the Fourier transform of the molecular dipole autocorrelation function determined using AM1 directly in QM/MM simulations is given in blue.

4.5. Conclusions

We have presented a nuclear quantum perturbation (QVP) method for efficiently determining the instantaneous vibrational frequency of a chromophore in molecular dynamics simulations. The QVP approach is a semiclassical approach that combines quantum mechanical treatment of nuclear motions of specific vibrational modes with classical dynamics simulations. The method treats intermolecular interactions as a

perturbation to the vibrational Hamiltonian on a predefined reference state. Computational efficiency is achieved as a result of three key ingredients, including (a) the use of potential optimized discrete variable representation (PODVR) of the vibrational wave functions for all levels of interest, (b) the application of perturbation theory to evaluate the energy shifts due to solvent dynamic fluctuations, and (c) the representation of the potential energy surface by a combined QM/MM approach for condensed-phase and macromolecular systems. Furthermore, we found that first-order perturbation is sufficiently accurate for the present HCl-water cluster system, a small but challenging test case due to strong bond-dissociation character associated with the vibrational mode as well as hydrogen bonding interactions. The use of the PODVR representation and perturbation theory to determine the energy shifts avoids the need to solve the vibrational Schrödinger equation. Thus, the computational cost of the QVP method is equivalent to that needed to determine the potential energies at the PODVR points. The use of a combined QM/MM approach incorporates naturally the effects of solvent dynamics on the potential energy surface, which can be systematically improved in accuracy and is computationally efficient. It also avoids the need to develop an empirical potential energy surface and the accompanying dipole moment surface for every new system. Since time-dependent vibrational frequencies can be determined on the fly in molecular dynamics simulations, the mode-specific linear and 2D-IR spectra can be extracted from the frequency time correlation function. Although the QVP method is validated using the HCl-water clusters, we emphasize that the approach can easily be extended to macromolecular systems since the perturbation theory calculation is only concerned with

one-electron integrals in a combined QM/MM potential. Thus, as long as it is possible to carry out QM/MM simulations at the desired QM level, the QVP1 method can be used to determine on-the-fly vibrational frequencies at the same or better accuracy.

Intra and intermolecular mode coupling can be important, but it is not specifically included in the present QVP method except the effect due to intermolecular interactions in the QM/MM potential energy surface. This is a subject of future research, though one can straightforwardly extend the present single mode approach to two or more coupled modes (as illustrated in the text), making use of the PODVR numerical method. Intramolecular (and intermolecular) mode-coupling can also be treated by using vibrational configuration interaction (VCI) as implemented in the MULTIMODE program, but the computational costs are prohibitive for computation of time-dependent vibrational frequencies. A linear scaling strategy is clearly desired.

To further reduce computational costs, we examined a hybrid, or composite strategy that can yield accurate peak position and line shape. In this scheme, the reference-state vibrational frequency (equation 4.2.1) is determined with a highly accurate method only once, but the vibrational frequency shifts at each instantaneous configuration along the MD trajectory are evaluated using the QVP method with a lower-level QM/MM potential. In the HCl-water cluster test cases, we compared the spectral result determined by using CCSD(T)-F12b on the entire system with that from the hybrid strategy with CCSD(T)-F12b reference frequency and M06-2X frequency shift. The agreement is very good, especially considering the tremendous cost-saving. Importantly, the inclusion of nuclear quantum effects, either using he semiclassical (equation 4.3.2) or cumulant

expansion (equation 4.3.3) algorithm, has a large effect on the computed spectra and is found to be in better agreement with experiment than that obtained by Fourier transform of the classical dipole autocorrelation function. We found that anharmonicity in the H-Cl stretch is significant and has a large solvent effects in the relaxation process exhibited in the computed 2D-IR spectra. To illustrate the general applicability, solvent effects on the carbonyl stretch of acetone in water were determined using QVP1 with a dual-level approach using the CCSD(T) results as the reference state coupled with combined QM(AM1)/MM simulations to account for solute-solvent interactions. The computed solvent-induced spectral shifts is in accord with experiment. The present QVP method complements other computational approaches, including path integral-based molecular dynamics, and represents a major improvement over the electrostatics-based spectroscopic mapping procedures.

Chapter 5. Implementation of Quantum Vibration Perturbation Theory: Application to Acetophenone Solvatochromic Shifts and Hydrogen Bond Exchange Dynamics of Acetophenone in Methanol and Other Solvents

This chapter is a result of collaborative efforts between the author and several members from the Massari group: Ivan C. Spector, Courtney M. Olson and Aaron Massari.

5.1. Introduction

The vibrational Stark effect offers a powerful experimental probe for understanding the electrostatic environment at the microscopic level both in condensed phases and in proteins. In practice, the electric field on the probed vibration mode is linearly related to the shift of the vibrational frequency.

$$\Delta\nu = -\Delta\boldsymbol{\mu}_{\text{probe}} \cdot \mathbf{E}_{\text{env}} \tag{5.1.1}$$

where $\Delta\boldsymbol{\mu}_{\text{probe}}$ is the difference in the dipole moment between the ground and excited vibrational state, which is often called the linear Stark tuning rate, and $\mathbf{E}_{\text{env}}$ is the electric field of the environment on the normal mode. In general, successful probes typically display two characteristic features. First, the vibrational mode is sensitive to the external electric field with a significant linear Stark tuning rate. Second, the vibrational

solvatochromic shifts can be adequately described by classical electrostatics. The reason for the first property is to have easily accessible spectral change, but the second is less obvious. When nitriles are used as the vibrational probes, it was found that there is significant quantum mechanical effect due to hydrogen bonding interactions with the solvent, resulting in large deviations from linearity with the external electric field. On the other hand, carbonyl groups have been shown to maintain an excellent linear correlation with respect to hydrogen bonding.

There are two contributing factors to the differential solvent effects on the dipole moments in the ground and the excited vibrational states. First, since the ground and excited vibrational states represent different nuclear motions, the expectation values of the position operator will be different even when the electronic configuration and charge density remains the same. Secondly, the probe molecule can also have differential polarization effects, which lead to an altered molecular dipole moment. There is no clear separation of the two effects and they are intimately coupled.

A variety of vibration probe molecules have been used to understand solvation dynamics and the electrostatic field effects on enzyme catalysis. Often, it is desirable that the vibrational frequency of the probe molecule is distinctly different from those of typical solvent molecules and amino acids. At the same time, there is strong absorbance to have sufficient sensitivity in the experiments. Thus, small molecules containing triple bonds such as azide and nitriles have been favored choices in these studies because their vibrational absorptions have strong absorbance, occurring in a region at about 2000 cm^{-1}, which is inert for aqueous and most organic solvents as well as biological systems. One

primary drawback is that the introduction of these functional groups could perturb the local environment of a biological molecule such as the active site of an enzyme. Alternatively, the C-D stretch vibration also has a frequency around the 2000 cm^{-1} region, which would introduce essentially no steric and electrostatic perturbation to the site being probed, and indeed, C-D stretching probes have been used in many biological systems. However, it is also not without shortcomings for its lack of strong absorption intensity. The use of carbonyl stretching vibrations from the amide bonds as well as several amino acid side chains has gained popularity because they have strong absorption intensities. These vibrational modes can be identified by difference spectra through isotope substitutions.

The small molecule acetophenone has been extensively studied as a vibrational probe to understand solvation effects, and the correlation of observed vibrational Stark effects and solvent electric field exerted on the vibrational mode coordinate. Boxer and coworkers[257, 258] performed Fourier transform infrared spectroscopy (FTIR) on acetophenone in a range of solvents, and coupled this with molecular dynamics simulations to calibrate the electric field with the solvent shift. Then they inserted an amino acid with an acetophenone side chain to measure the electrostatic environment inside ribonuclease-S, which suggests a relatively nonpolar environment. Subsequent work[154, 259, 260] by the Boxer group suggests that carbonyl vibrational probes are advantageous due to the fact that they maintain linearity with respect to hydrogen bonding. In fact, they used a 19-nortestosterone as a product-like inhibitor in ketosteroid isomerase, and found very high electric fields on carbonyl upon binding, which supports

the hypothesis that the catalytic mechanism goes through an enolate intermediate.[154] The solvent effects on the vibrational frequency shifts are investigated in this study. Furthermore, in collaboration with Professor Aaron Massari and his group, we extend the work to understand the local solvent dynamics through two-dimensional FTIR spectroscopy.

To understand solvent dynamics on the observed one and two-dimensional vibrational spectra, it is necessary to determine the time-dependent vibrational frequencies of the oscillator in molecular dynamic simulations. The most effective and widely used approach to estimate instantaneous vibrational frequency shifts on the fly in molecular dynamics simulations is based on an electrostatic map. This technique goes beyond a simple linearized Stark effect by sampling the electrostatic field surrounding the probe molecule. As an empirical approach, anharmonic and quantum mechanical effects are included in an average sense into the parameterization. A particular advantage of the electrostatic map is that solvent effects on vibrational properties can be estimated efficiently. Nevertheless, one drawback is that each property needs to be parameterized separately; for example, the calculation of vibrational frequency and transition dipole moment require different electrostatic maps.

In principle, molecular vibration can be modeled directly by solving the vibrational Schrödinger equation, and this approach has been applied to numerous systems. In this case, there is no need to specifically parameterize electrostatic maps for different molecules. For instance, it possible to perform normal mode analysis at step in a molecular dynamics trajectory.[261] However, this method is time consuming because it

requires the computation and subsequent diagonalization of the Hessian matrix at each step, and it yields frequencies that do not include anharmonicity and are often include negative eigenvalues yielding imaginary frequencies. Another approach is to solve the one-dimensional vibrational Schrödinger equation, which avoids the calculation of the Hessian, includes anharmonicity and yields quantum mechanical frequencies. In this approach, a basis set is used for variational optimization and the Hamiltonian matrix elements are determined by numerical quadrature.[262, 263] The difficulty with this approach is that a large number of basis functions (~75-100) is required for converged results,[264] and the vibrational coordinate must be well defined throughout the molecular dynamics trajectory. Furthermore, the discrete variable representation (DVR) permits the variational solution of the one-dimensional Schrödinger equation by using localized basis sets that are amenable to numerical quadrature.[262, 265-270] The purpose of this chapter is to present a quantum mechanical model without explicitly solving the vibrational Schrödinger equation in a manner that obtains computational efficiency.

5.2. Theoretical Methods

The quantum vibration perturbation (QVP)[271] approach is an efficient method for computing the instantaneous vibrational frequencies of a probe molecule in condensed phases and in proteins. Currently, it is designed for one and two specific modes along with the coupling between these two modes. QVP combines two computational concepts to achieve computational efficiency: (1) a numerical representation of the nuclear wave function for the solute and (2) a perturbation theory to account for the solvent effects.

Consequently, the method enables vibrational energy levels and wave functions to be efficiently determined on the fly of molecular dynamics simulations.

In QVP, we first use a potential-optimized discrete variable representation (PO-DVR) to evaluate the vibrational Hamiltonian matrix elements over quadrature points of the vibrational wave functions. Then, the changes in wave function and the corresponding eigenvalue due to instantaneous fluctuations of the solute geometry and solvent configuration are determined using perturbation theory. In the present study, the interactions between acetophenone and water molecules are modeled by a combined quantum mechanical and molecular mechanical (QM/MM) method, in which the solute is treated quantum-mechanically and the solvent by the all atom optimized potential for liquid simultations (OPLS-AA). Thus, the instantaneous change of the potential energy surface of the solute molecule, which is essential for interpreting two-dimensional infrared experiments, is included in the present model. The following highlights the key computational details as it was implemented in the CHARMM package.[272]

5.2.1 QVP Implementation

In this section, the two computational components of the quantum vibrational perturbation (QVP) method are presented, namely (1) potential optimized discrete variable representation (PO-DVR) of the nuclear wave function, and (2) a perturbation approach to determine solvent effects on the vibrational frequency shifts.

In the first computational step, we solvent the vibrational Schrodinger equation numerically using a PO-DVR approach. The DVR method described by Colbert and

Miller[273] has been widely used in reaction dynamics calculations due to several features that are convenient for computation.[274] In the original approach, the basis set for the vibrational Hamiltonian is an infinite basis of evenly spaced sinc functions (equation 5.2.1.c), which are already localized. Thus, the position operator is diagonal, and the locations (q_μ) of the sinc functions are the Gaussian quadrature points for numerical integration.[274]

The kinetic energy operator has an analytical solution, therefore, it is exact at the limit of a complete set of basis functions. The only approximation begin made in the kinetic energy operator is due to truncation of the basis set. For a finite basis set representation, the error in the kinetic energy diminishes exponentially outside the classically allowed region of phase space.[275] Consequently, for practical purposes, DVR results converge quickly with a reasonably large basis[268] (see table 5.1). The definition of the DVR requires only two parameters, the grid spacing (Δq) and the number of basis functions (N^{DVR}). Additionally, there is no assumption as to the functional form of the potential operator because it only needs to be evaluated at the quadrature points. The grid spacing defines an upper bound to the kinetic energy,[275] and the Hamiltonian operator is written as

$$H_{\mu\mu} = \frac{\hbar^2\pi^2}{6m\Delta q^2} + V(q_\mu) \qquad (5.2.1.a)$$

$$H_{\mu\nu} = \frac{\hbar^2(-1)^{\mu-\nu}}{m\Delta q^2(\mu-\nu)^2} \quad for \;\; \mu \neq \nu \qquad (5.2.1.b)$$

$$\chi_\mu(q) = \frac{\sin(\pi(q-q_\mu)}{\pi(q-q_\mu)} \qquad (5.2.1.c)$$

where m is the reduced mass of the oscillator, $V(q_\mu)$ is the potential energy at the DVR point, and q is the normal mode coordinate. An approximation[274, 276] commonly used in the DVR method is to assume a diagonal form of the potential energy operator.

Table 5.1. First and second transition energies calculated using different number of basis functions and grid spacing values using the discrete variable representation (DVR) approach described by Colbert-Miller, and the potential optimized DVR (PO-DVR) method for the same configuration of acetophenone in water. For convenience, bold texts are used to highlight digits that match the exact values (from the largest grid calculations).

Number of Basis	Grid Spacing (Å)	$\nu_{0\to1}(cm^{-1})$	$\nu_{1\to2}(cm^{-1})$
1000	0.001	**1952.513805**	**1936.732571**
50	0.01	**1952.513805**	**1936.732571**
30	0.01	**1952.5**22591	**1936**.914562
PO-DVR: 10	-	**1952.513**742	**1936.7325**08

The procedure described by Colbert and Miller is general for practical applications. Nevertheless, it has been shown that the number of quadrature points can be

significantly reduced for a given potential $V(x_i)$, which will significantly increase the computational speed, especially in molecular dynamics simulations. Consequently, ab initio wave function theory or density functional theory can be directly used to represent the potential energy surface to obtain the instantaneous vibrational frequencies in molecular dynamics simulations. To this end, a minimal number of quadrature points is generated to best represent a given potential at a convergence tolerance. Thus, the numerical quadrature points are optimized according to the potential used, giving rise to the name for the method, potential optimized DVR (PO-DVR).[277, 278] The method amounts to a single-value decomposition of the position operator in the full basis into a reduced N^{PO}-dimension, where N^{PO} is the number of PO-DVR points used for numerical representation of the vibrational wave function. First, the Hamiltonian is solved in the full basis by diagonalizing the Hamiltonian, then the position operator of the optimized basis is calculated by using the lowest N^{PO} eigenvectors of the Hamiltonian. This matrix is then diagonalized to yield to potential PO-DVR points. The coordinate transformation can be summarized as follows

$$\boldsymbol{x}^{PO} = \boldsymbol{V}^{\dagger}\boldsymbol{U}^{\dagger}\boldsymbol{x}\boldsymbol{U}\boldsymbol{V} \tag{5.2.2}$$

where $\boldsymbol{U}$ is a rectangular matrix of eigenvectors for the Hamiltonian in the full basis. The dimension of this matrix is $N^{DVR} \times N^{PO}$. $\boldsymbol{V}$ is a unitary matrix that diagonalizes the

position operator ($\boldsymbol{U}^{\dagger}\boldsymbol{x}\boldsymbol{U}$). $\boldsymbol{x}^{PO}$ and $\boldsymbol{x}$ are diagonal, representing the PO-DVR and DVR points, respectively. The same transformation is performed on the Hamiltonian, which is diagonalized to yield the eigenvalues and eigenvectors of the PO-DVR basis.

The second ingredient of the QVP method is to enhance computational efficiency. Here, we use perturbation theory to determine the eigenvectors and eigenvalues rather than performing a direct diagonalization. Here, we define the QVP energy as

$$E_i(\boldsymbol{r}_k) = E_i^0\left(\boldsymbol{r}_k^{ref}\right) + \Delta U_i(\boldsymbol{r}_k) \tag{5.2.3}$$

where $E_i(\boldsymbol{r}_k)$ is the configuration-dependent energy eigenvalue of the nuclear wave function of state *i*, $E_i^0\left(\boldsymbol{r}_k^{ref}\right)$ is the eigenvalue of the unperturbed reference state, and $\Delta U_i(\boldsymbol{r}_k)$ is the change in potential energy due to configuration fluctuations. The latter is obtained using the Raleigh-Schrödinger perturbation theory.[279] The perturbation operator between PO-DVR wave functions *i* and *j* is defined as

$$\mathrm{V_{ij}}(\boldsymbol{r}_k) = \sum_{l}^{N^{PO}} c_{li}(q_l)\left(U(\boldsymbol{r}_k; q_l) - U\left(\boldsymbol{r}_k^{ref}; q_l\right)\right)c_{lj}(q_l) \tag{5.2.4}$$

where $c_{li}(q_l)$ is the PO-DVR eigenvector and $U(\boldsymbol{r_k}; q_l)$ is the potential energy of configuration, $\boldsymbol{r_k}$, with the normal mode at the PO-DVR point, q_l. The Raleigh-Schrödinger correction to the energy is given by:

$$\Delta U_i(\boldsymbol{r_k}) = \Delta U_i^{(1)}(\boldsymbol{r_k}) + \Delta U_i^{(2)}(\boldsymbol{r_k}) + \cdots \quad (5.2.5.a)$$

$$\Delta U_i^{(1)}(\boldsymbol{r_k}) = V_{ii}(\boldsymbol{r_k}) \quad (5.2.5.b)$$

$$\Delta U_i^{(2)}(\boldsymbol{r_k}) = -\sum_{j \neq i}^{N^{PO}} \frac{\left|V_{ij}(\boldsymbol{r_k})\right|^2}{E_j^0(\boldsymbol{r_k}) - E_i^0\left(\boldsymbol{r_k^{ref}}\right)} \quad (5.2.5.c)$$

where the expansion in equation 5.2.5.a can be carried out to $N^{PO} - 1$ order, but for small perturbations, equation 5.2.5.a converges quickly relinquishing the need for higher order corrections. The formulae for third and fourth order corrections can be found in reference [279]. In the PO-DVR representation, the calculation of $\Delta U_i(\boldsymbol{r_k})$ requires only single-point energies at the quadrature points without the need to directly solve the vibrational Schrodinger equation.

5.2.2 Transformation Matrix for the Normal Mode

As the molecular frame and eigenvector of the desired mode change during a molecular dynamics simulation, it is necessary to transform the coordinates, and, thus, the normal mode vector to match the reference eigenvector throughout the trajectory. Here, we adopt an algorithm[280] used in computer vision in which the coordinates of a moving

object are treated as a roughly rigid body to be transformed to the reference set of points. The relationship between the reference and instantaneous coordinates is given below,

$$\boldsymbol{r}_k^{ref} = \boldsymbol{T}(\boldsymbol{r}_k - \boldsymbol{R}^{com}) + \boldsymbol{\zeta}_k \tag{5.2.6}$$

where $\boldsymbol{r}_k$ is the set of instantaneous coordinates, $\boldsymbol{r}_k^{ref}$ is the reference set of coordinates. The reference coordinates have their center of mass at the origin. $\boldsymbol{R}^{com}$ represents the rigid-body translation of the center of mass, and $\boldsymbol{\zeta}_k$ is a noise term which in the present case for molecular vibration refers to atomic displacements. Each of the bolded terms in equation 5.2.6 is a three-dimensional vector, and the ones that include the index k are part of a set of N^a vectors resulting in $3N^a$ degrees of freedom where N^a is the number of atoms. In equation 5.2.6, $\boldsymbol{R}^{com}$ can be computed exactly from the Cartesian coordinates. The effect of the $\boldsymbol{\zeta}_k$ term will be discussed in the context of QVP later in this section. $\boldsymbol{T}$ is the rotation matrix between the reference and instantaneous coordinate frames and is a three-dimensional matrix. The calculation of the rotation matrix (T) is nontrivial and is a main contribution of this algorithm.

Arun and *et al.* showed that the calculation of the rotation matrix is equivalent to solving the unitary transformation that leads to a maximum in the sum of the dot products of all of the position vectors, which may be expressed as follows

$$F = \max\left(Trace\left(\sum_{k}^{N^a} \boldsymbol{Tr_k}\left[\boldsymbol{r_k^{ref}}\right]^T \right) \right) \tag{5.2.7}$$

When $\boldsymbol{\zeta_k}$ is nonzero, this equation results in the least squares solution for the rotation. If $\boldsymbol{\zeta_k}$ is zero, then, by the Cauchy-Schwarz inequality, T, which maximizes F, is exact and unique for cases without symmetry (*vide infra*). To solve equation 5.2.7, we begin by computing:

$$\boldsymbol{S} = \sum_{k}^{N^a} \mathbf{r_k}\left[\boldsymbol{r_k^{ref}}\right]^T = \sum_{k}^{N^a} \begin{bmatrix} x_k x_k^{ref} & x_k y_k^{ref} & x_k z_k^{ref} \\ y_k x_k^{ref} & y_k y_k^{ref} & y_k z_k^{ref} \\ z_k x_k^{ref} & z_k y_k^{ref} & z_k z_k^{ref} \end{bmatrix} \tag{5.2.8}$$

where $\boldsymbol{S}$ is a 3 x 3 real nonsymmetric matrix, where the trace of $\boldsymbol{S}$ is the dot product of the two sets of position vectors. Next, a singular value decomposition is performed on $\boldsymbol{S}$.

$$\boldsymbol{s} = \boldsymbol{U}^T \boldsymbol{S}\, \boldsymbol{V} \tag{5.2.9}$$

where $\boldsymbol{s}$ is the diagonal matrix of singular values and $\boldsymbol{U}$ and $\boldsymbol{V}$ are the left and right singular vectors. Thus, the rotation matrix that maximizes equation 5.2.7 is:

$$\boldsymbol{T} = \boldsymbol{V}\boldsymbol{U}^T \tag{5.2.10}$$

Equation 5.2.10 reduces the effect of the cross terms, or off-diagonal elements in equation 5.2.8, which results in a maximum due to the Cauchy-Schwarz inequality. It was noted earlier that this algorithm yields unique solutions for systems without symmetry only.

Next, we explore the effects of symmetry on this algorithm.

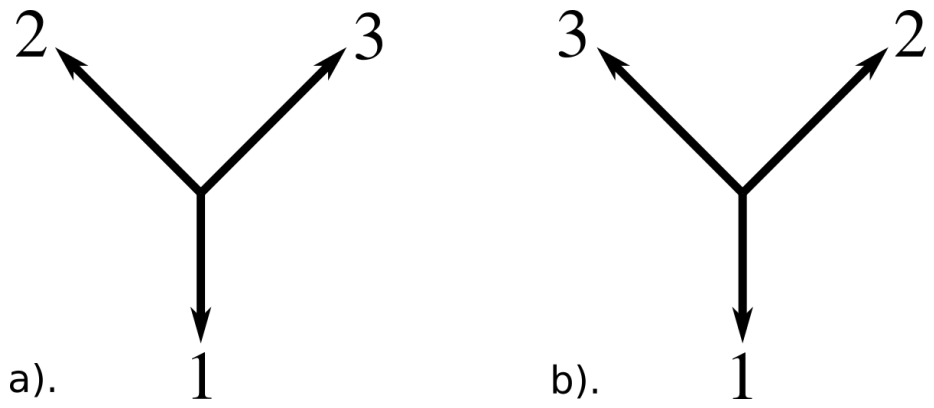

Figure 5.1. Two sets of three coplanar position vectors in the C2v point group. The index of each vector is given at the tip of each vector. The only difference between the two sets is reflection through the mirror plane.

Consider, two sets of vectors shown in Figure 5.1 as possible target for this algorithm. These vectors are given in the C2v point group, having a mirror plane along the principle axis of rotation (along vector 1). If we assume ζ_k is zero, then both sets of vectors have the same solution to equation 5.2.7, suggesting that any symmetry transformation of one solution would similarly be a valid solution to equation 5.2.7, which shows that the solution is not unique. To clarify, every symmetry operation in group theory has a matrix representation. This means that if one multiplies the rotation matrix by a symmetry operator, then this yields the same result for equation 5.2.7. This

concept demonstrates that the vectors are indistinguishable with respect to index due to the summation in equation 5.2.7. This may not be a particular issue for general parameter sets from computer vision that may not display a significant amount of symmetry, but for molecules, different position vectors could correspond to different atomic identities. In practice, we observed that incorrect orientations of normal mode have been generated directly using equation 5.2.7, leading to spurious frequencies in the trajectory (see Figure 5.2).

This problem can be circumvented by weighting $\boldsymbol{S}$ according to the magnitude of the normal mode displacements:

$$\boldsymbol{S} = \sum_{k}^{N^a} |q_k|^2 \left(\boldsymbol{r_k} \left[\boldsymbol{r_k^{ref}} \right]^T \right) \tag{5.2.11}$$

where $|q_k|$ is the magnitude of the normal mode displacement of the kth atom. This modification highlights different contributions of the atomic displacement of the vibrational mode of interest. Consequently, incorrect solutions due to symmetry have been avoided, or, at the very least, the solutions would remain within the vibrational point group. An advantage of the modified algorithm is that the implementation is straightforward using singular value decomposition and data in the program already.

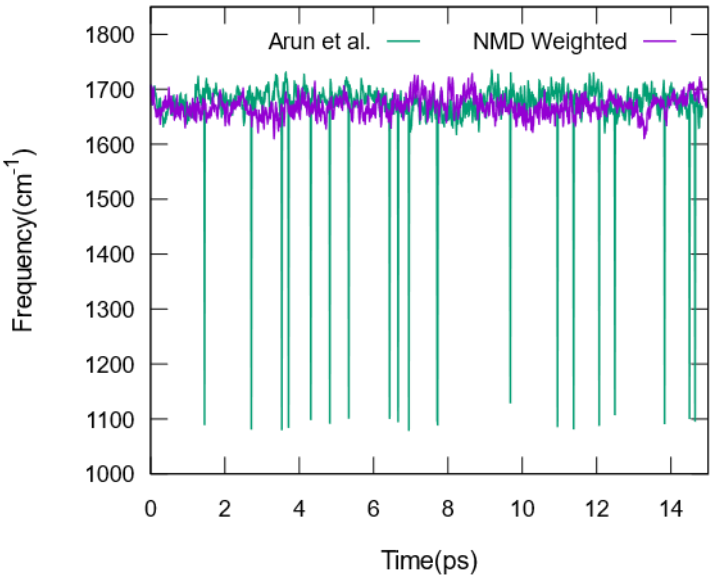

Figure 5.2. Frequency trajectories computed using the Arun et al. algorithm for the rotation matrix and the normal mode displacement (NMD) weighted algorithm presented in equation 5.2.11.

The weighted transformation brings the solute molecule at an arbitrary orientation, coupled with internally distorted geometry, sampled during a molecular dynamics simulation to maximally superimpose with the reference mode structure, allowing the vibrational frequency to be computed using the QVP method.

The instantaneous vibrational frequency for a mode of interest is determined by its frequency shift relative to the reference state. In QVP, the numerical quadrature points are optimized with respect to the minimum energy geometry. However, the geometry of the solute molecule at time t is somewhat distorted from the reference structure. Thus, to ensure numerical accuracy, it is important to further refine the maximally matched geometry such that there is minimal deviation from the quadrature points. Here, we perform local restrained geometry optimization along the reference mode direction to

locate its minimum position. Then, the ζ_k term in equation 5.2.6 has the effect to match the minimal of one-dimensional potential energy profile along the mode coordinate for the MD structure to the origin of that for the reference geometry.

Shown in Figures 5.3 (a) and (b) are the computed vibrational frequencies using QVP with second order perturbation (QVP2) compared with the exact values for acetophenone in water sampled in molecular dynamic simulations. Figures 5.3 (c) and (d) display the potential energies curves along the mode coordinate, both for the reference configuration and for one randomly chosen structure in Figures 5.3 (a) and (b). Figures 5.3 (a) and (c) correspond to QVP2 calculations employing the reoriented configurations without the ζ_k term, whereas results displayed in Figures 5.3 (b) and (d) are obtained by aligning the minimum of the one-dimensional potential energy curve of the MD structures with the reference state. The minima are obtained by restrained geometry optimization involving atoms of the local mode only (in the present acetophenone, the carbonyl group and atoms directly connected to the carbonyl carbon atom), while all other atoms are held fixed using the adopted basis Newton-Raphson method in CHARMM. The shaded areas depicted in Figures 5.3 (c) and (d) illustrate the magnitude of the perturbation energy. The only difference between Figures 5.3.c and 5.3.d is translation along the normal mode coordinate. Overall, the mean-unsigned-errors (MUE) are 3.2 and 2.4 cm^{-1} for calculations with and without the ζ_k term, and the results without potential alignment systematically underestimate the computed vibrational frequencies.

Figure 5.3 shows that both perturbation contributions due to interactions with the solvent and the instantaneous geometric distortions of the solute and the errors in the computed frequencies are smaller when the mode displacements are performed at the potential energy minimum. Since we are interested in the carbonyl stretch, this means that the bond length for the reference structure and the instantaneous structure can be different, and that the normal mode displacements occur from the potential energy minimum.

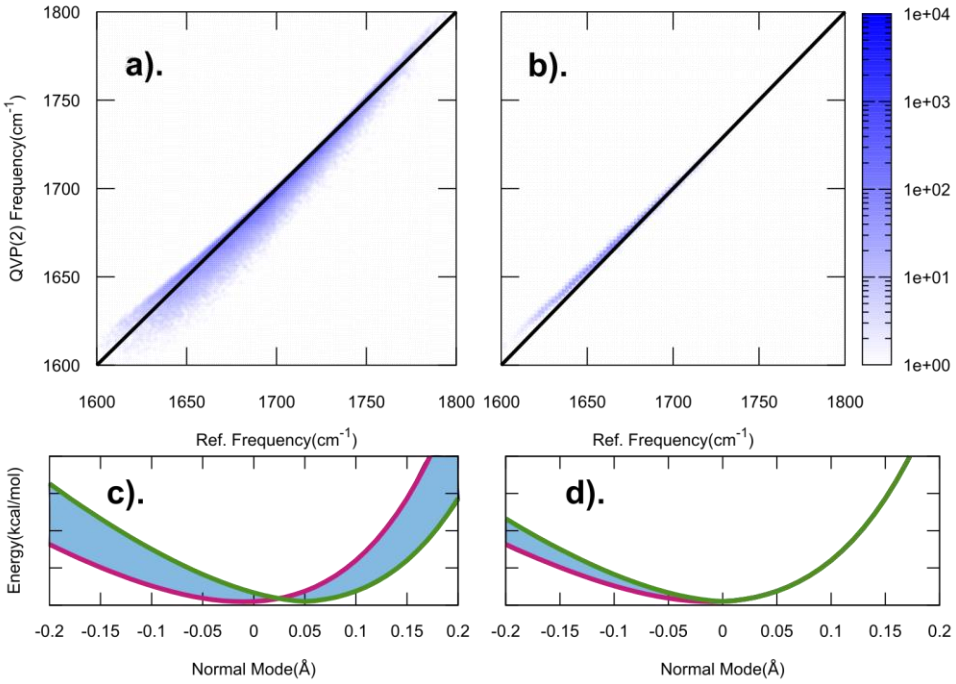

Figure 5.3. (a) and (b). Computed vibrational frequencies using second order quantum vibrational perturbation (QVP2) method against the exact results calculated with 50 discrete points at a grid interval of 0.01 Å (Reference) with (a) and without (b) alignment of the potential energy minimum along the mode coordinate. **(c) and (d)** show the potential energies along the mode coordinate for one randomly selected structure without (c) and with (c) the minimum matched against the reference state. The shaded region represents the magnitude of the perturbation operator in QVP.

5.3 Computational Details

Molecular dynamics simulations were performed employing in the isothermal-isobaric ensemble at 1 atm and 298 K for a single acetophenone solute in solvent boxes of ca. 40 × 40 × 40 $Å^3$. The solvents considered in this work cover a wide range of polarities, including carbon tetrachloride (CCl_4), n-hexane, diethyl ether (DEET), N,N-dimethyl acetamide (DMA), chloroform ($CHCl_3$), acetonitrile (MeCN), methanol (MeOH) and water. All calculations were performed using a locally modified version of the CHARMM software package, in which the QVP method up to the fourth order perturbation has been implemented.[272] The potential energy surface was described using a combined quantum mechanics and molecular mechanics (QM/MM) approach. The solute molecule, acetophenone, is represented by PM3[281-283] and the organic solvents are modeled with the OPLS-AA[284, 285] force field. Following an initial equilibration, molecular dynamics was carried out for 2-4 ns at a 1-fs time step, during which coordinates were saved on every 10 *fs*, sufficient for the analyses and Fourier transform of the response functions.

5.3.1. QM/MM potential for the carbonyl stretch vibration and hydrogen bonding interactions of acetophenone

The C=O stretch vibrational frequency (1942.4 cm^{-1}) from DVR calculations using the PM3 potential is overestimated by 240.0 cm^{-1} in comparison with a value of 1702.4 cm^{-1} based on the MP2/aug-cc-pVDZ representation of acetophenone in the gas phase. The MP2 result is in good accord with the experimental observation (1701 cm^{-1}). Here, the one-dimensional potential energy curves are scanned along the normal mode

coordinate for each method. Thus, the DVR results include anharmonic contributions as well as nuclear quantum effects, although mode coupling is ignored. It is possible to make a constant shift of the absolute vibrational frequency from PM3 to match the experimental data in the gas phase, when solvent effects are studied. However, we have decided to modify the core-core energy term (equation 5.3.1) in PM3 for the carbonyl carbon and oxygen atoms since solvent dynamics is investigated through 2D-FTIR calculations. These changes only affect the carbonyl group, and its interaction with the solvent, without altering the electronic structural part of the Hamiltonian.

$$H_{core}^{PM3} = Z_A Z_B \langle AA|BB\rangle (1 + e^{-\alpha_A R_{AB}} + e^{-\alpha_B R_{AB}}) + \frac{Z_i Z_j}{R_{AB}} \left(\sum_k^4 a_{k_A} e^{-b_{k_a}\left(R_{AB} - c_{k_A}\right)^2} + \sum_k^4 a_{k_B} e^{-b_{k_a}\left(R_{AB} - c_{k_A}\right)^2} \right) \quad (5.3.1)$$

where Z_A and Z_B are the effective nuclear charges (note only valence electrons are treated explicitly in semiempirical methods) of atoms *A* and *B*, R_{AB} is the interatomic distance, $\langle AA|BB\rangle$ is the electron repulsion integral between two s-orbitals, and α_{k_A} and α_{k_B} are damping parameters. The remaining Gaussian terms in equation 5.3.1 are introduced to account for errors in the bonding region in the origin MNDO model and their parameters are optimized in the parameter fitting process

Figure 5.4 shows the computed potential energy curves for the carbonyl stretch vibration along the normal mode coordinate using MP2 and PM3 methods, along with

their difference and a polynomial fit. Negative and positive values of the mass-weighted coordinate (in a.u.) in Figure 5.4 represents extension and compression from the equilibrium geometry. Evidently, the errors of PM3 dominantly comes from its more steep increase in energy as the C=O bond is stretched, consistent with a higher vibrational frequency. The energy difference, $\Delta U(q)$, between the MP2 and PM3 results, expressed in equation 5.3.2 with a fitting error of less than 0.1 kcal/mol, are added to the original core-core term between the carbonyl carbon and oxygen atoms since their atomic displacements account for more than 95 % of the normal mode motion.

$$\Delta U(q) = Aq + Bq^2 + Cq^3 + Dq^4 + Eq^5 + Fq^6 \qquad (5.3.2)$$

where q is the mass-weighted displacement vector of the carbonyl stretch mode. The PM3+ΔU potential energy surface gives a carbonyl stretch frequency of 1704.1 cm^{-1}, reproducing the MP2 value. The parameters in equation 5.3.2 are given in Table 5.2.

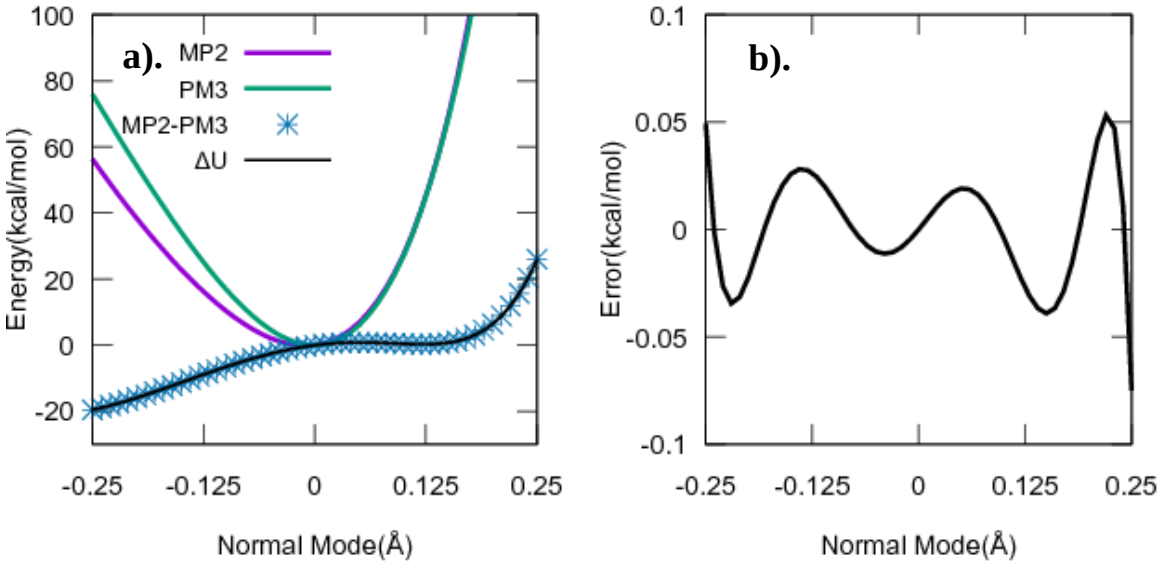

Figure 5.4. a). Potential energy scans of the normal mode of the carbonyl stretch of acetophenone at the level of MP2/aug-cc-pVDZ, PM3, and the difference between both levels of theory and result of fitting equation 5.3.1. **b).** The error of the fit as a function of the normal mode.

Table 5.2. Fitted parameters for equation 5.3.1

Parameter	Value
A(kcal/mol/Å)	34.6
B(kcal/mol/Å^2)	-358.8
C(kcal/mol/Å^3)	-128.2
D(kcal/mol/Å^4)	5048.6
E(kcal/mol/Å^5)	16454.7
F(kcal/mol/Å^6)	24341.1

In the combined QM(PM3)/MM potential, the Gaussian terms in equation 5.3.1 between QM and MM atoms are not included, and a value of 5.0 for aS for all MM atoms has been recommended.[286] To best describe hydrogen bonding interactions between the

carbonyl group with a hydrogen bond donor such as methonal, we re-introduced a single Gaussian term on the oxygen atom

$$H_{OM}^{QM/MM} = H_{OM}^{PM3} + \frac{Z_M}{R_{AM}}\left(ae^{-b(R_{AB}-c)^2}\right) \qquad (5.3.3)$$

where Z_M is the partial charge of "MM atom" *M*, R_{AM} is the distance between the carbonyl oxygen of acetophenone and *M*, and the parameters *a*, *b* and *c* are fitted to reproduce the potential energy curve for hydrogen bonding interactions between acetophenone and methanol determined at the MP2/aug-cc-pVDZ level of theory. The final parameters are summarized in Table 5.3.

Figure 5.5 displays the results obtained using the final combined PM3/MM potential that includes the two additions to the potential on the carbonyl carbon and oxygen atoms that affect the internal C=O stretch of acetophenone itself and hydrogen bonding interactions between acetophenone and solvent molecules, along with those from MP2/aug-cc-pVDZ and the original PM3/MM without these additions. One notices that the standard QM/MM potential with PM3 Hamiltonian underestimate hydrogen bonding interactions between acetophenone and methanol by 1.4 kcal/mol, compared with a binding energy of -7.6 kcal/mol from MP2 calculations. The present acetophenone stretch-vibration specific model, PM3v, gives a binding energy of -7.4 kcal/mol. The PM3v model is used to perform molecular dynamics simulations of acetophenone in solutions.

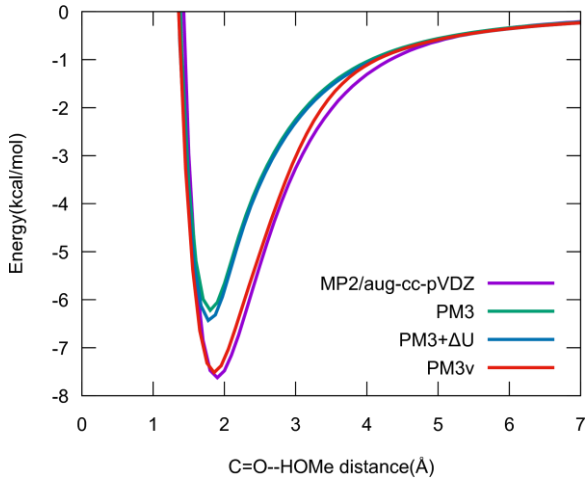

Figure 5.5. Computed interaction energies between acetophenone and methanol as a function of the distance between donor and acceptor oxygen atoms using the MP2/aug-cc-pVDZ (purple), the standard PM3/OPLS potential, the PM3+ΔU model for the QM part, and the final PM3v/OPLS model.

Table 5.3. Fitted parameters for equation 5.3.3

Parameter	Value
a	13.3 (kcal/mol)Å/e^-
b	0.92 $Å^{-2}$
c	2.05 Å

5.3.2. Carbonyl Stretch Vibrational Frequency and Electric Field Calculations

The vibrational spectra for the solute in different solvents can be directly obtained from Fourier transforms of the molecular dipole autocorrelation functions, which include contributions both from solvent effects and anharmonicity, although nuclear quantum mechanical effects on solute motions are ignored. The latter is included in the present QVP method, but nuclear quantum mechanical effects due to solute-solvent coupling are not included. We used second-order perturbation, denoted as QVP2, to determine the

ground state and the first two excited vibrational energy levels and the first and second transition energies. In all, for each configuration in the dynamic trajectory, the solute molecule was first energetically optimized using the adopted-basis Newton-Raphson (ABNR) algorithm with the solute and the solvent coordinates fixed except for the atoms participating in the normal mode. This was followed by 10 single-point QM/MM energy calculations at the PO-DVR grid points along the carbonyl stretching vector. The overall computational cost in the QVP2 analyses is of the same order as that used to carry out the QM/MM dynamics simulations. Additional computational details can be found in reference 287.

The QVP calculations yield time-dependent vibrational frequencies of the C=O stretch mode, based on which both linear infrared (IR) and 2D-FTIR spectra can be determined.[288, 289] The linear absorption line shape[290-292] was calculated using

$$I(\omega) \sim Re \int_0^{t_{max}} dt\, e^{-i(\langle\omega\rangle-\omega)t} \langle \exp[i \int_0^t dt'\, \delta\omega(t')] \rangle \exp\left[-\frac{t}{2T_1}\right] \qquad (5.3.4)$$

where, T_1 is the population relaxation time corresponding to the 1→0 transition, $\delta\omega(t)$ is the fluctuation of the C=O frequency at time *t* from the mean, $\langle\omega\rangle$. For T_1, the experimental value of 1.73 ps was used. The two dimensional Fourier transform infrared (2D-FTIR) spectra corresponding to the photon echo experiments were computed following the procedure described in Reference 291, which permits modelling of non-Gaussian fluctuations,[292] for describing hydrogen bonding interactions.[293] We found that

it is particularly important to model non-Gaussian fluctuations for acetophenone in methanol because there are two overlapping absorption peaks corresponding to different hydrogen bond configurations (see Figure 5.7 and the supporting information of reference 260). Kwac and Cho[292] showed that using the second cumulant expansion response functions does not adequately model non-Gaussian fluctuations, resulting in a single peak instead of two overlapping peaks.

The linear Stark effect was analyzed in order to compare with the work by Fried e al.[257, 258] In the present simulation, the electric field on the carbonyl stretch mode of acetophenone was calculated in a similar manner to that reported in reference 258. Briefly, the force on the carbonyl carbon and oxygen atoms was calculated with and without electrostatics. Then the difference between these two vectors yields the electric field. Subsequently, these vectors are projected onto the bond vector, and averaged to yield the effective electric field on the mode:

$$E_{mode} = -\frac{1}{2}(\boldsymbol{E_C} \cdot \boldsymbol{r_{co}} + \boldsymbol{E_O} \cdot \boldsymbol{r_{co}}) \qquad (5.3.5)$$

5.4 Experimental Details

The Fourier transform infrared (FTIR), and 2D-IR spectra of acetophenone in methanol were also obtained experimentally by Ivan C. Spector, in collaboration with the Massari group. The IR spectra were collected on a Nicolet 6700 FTIR spectrometer (Thermo Scientific) with at least 16 scans and a resolution of 2 cm^{-1}. The 2D-IR instrument has been described in detail previously.[294, 295] Mid-IR pulses (3 μJ /pulse, 1

kHz repetition rate, 90 fs duration FWHM, ~200 cm^{-1} bandwidth FWHM) were tuned to the carbonyl stretching region (~ 1700 cm^{-1}), divided into three ~1 μJ p-polarized pulses, and focused on the sample in a BOXCARS geometry.[296] The generated vibrational echo signal was coaligned with a local oscillator reference pulse (0.3-0.5 nJ per pulse), spectrally resolved in a 0.32 meter monochromator with a 75 line/mm grating, and detected with a liquid N_2 cooled 64-element mercury cadmium telluride (MCT) linear array detector (Infrared Associates, Inc). The spectral resolution of the detection system is ~ 4 cm^{-1}. Data collection was performed with fibrillation to remove scatter from all three pump beams, as described in reference 297.

Purely absorptive 2D-IR spectra were obtained using the technique described by Khalil and coworkers.[298, 299] In order to account for systematic and random errors in the instrumentation, the data were phase processed, as described in detail by others.[300] The pump-probe projection theorem and absolute value center method were used as constraints during this procedure.[301] IR pump-probe spectroscopy was carried out using the same laser system described above.[295] The resulting purely absorptive and absolute value data plots were then analyzed using peak volumes to extract kinetic information directly from the 2D-IR data, as described in more detail below. [302-304] Center line slope analysis was performed on the on-diagonal peaks in the purely absorptive spectra.[300]

Figure 5.7 shows two representative experimental 2D-IR spectra at 0.25 ps and 3.0 ps following the initial activation. Spectral intensity increases in the region above the diagonal between the two peaks. This is a strong indication of exchange between the absorption modes associated with the two on-diagonal peaks. The peaks are assigned as

hydrogen bonded (1677 cm^{-1}), and non-hydrogen bonded (1688 cm^{-1}) and therefore the growth of the off-diagonal peak above the diagonal indicates the breaking of hydrogen bonds. On-diagonal peaks decay due to population relaxation with an exponential decay constant T_1. Off-diagonal peaks arising from processes other than anharmonic coupling will decay more slowly than the on-diagonal peaks. Chemical exchange or vibrational energy exchange rate constants are extracted by normalizing off-diagonal peaks by their corresponding on-diagonal peaks.[302, 303] Exponential rise fits were performed on the amplitude of the ratio of off-diagonal peak volume to the on-diagonal peak volume at the same probe/ω_m frequency. The exponential growth time from fitting this ratio to an exponential rise function of the form: $Exchange = C + A * (1 - e^{-\frac{T_w}{\tau_{rise}}})$; is 1.0 +/- 0.8 ps. Gaffney and coworkers found H-bond breakage in MeOD oligomers on the time scale of 0.2-2 ps.[305]

The change in the on-diagonal peak shapes (spectral diffusion) is quantified by the center-line-slope (CLS) analysis.[300] Center-line-slope decays were fit according to the procedures developed by Kwak and coworkers which has been regularly utilized by the Massari group.[294, 300] The challenge in CLS analysis presented by lack of complete resolution between the off-diagonal and the two on-diagonal peaks was overcome by narrowing the spectral range for CLS fitting. The range (~ 8 cm^{-1}) covered the maxima and excluded the region where the two on-diagonal peaks overlapped. The CLS decay time constants for a single exponential of the form: $CLS = A * e^{-T_w/\tau}$; are 3.2 +/- 0.7 ps

for the red peak centered at 1677 cm^{-1} and 4.0 +/- 0.9 ps for the blue peak centered at 1688 cm^{-1}. These time constants are reasonable for small molecules in normal solvents based on other literature values.[294, 306] All experimental errors are quoted at the 95 % confidence interval.

5.5. Results and Discussion

The striking solvent effects on the computed vibrational Stark shifts for acetophenone in the solvents examined in this study are given in Figure 5.6 and Table 5.4. The trends from the present QM/MM molecular dynamic simulations are in good accord with that observed by Boxer and coworkers. There is a good correlation of the magnitude of red-shift with solvent polarity as measured by the ET(30)[307] scale.[308-310] A linear fit between the observed spectral shifts in Figure 5.6 and the computed electric fields yields a Stark tuning rate of 0.45 cm^{-1}/MV/cm, which is similar to that obtained by Boxer and coworkers (0.484 and 0.412 cm^{-1}/MV/cm for AMOEBA and AMBER force fields respectively).[308, 309] In comparison with experiments, Table 5.1 shows that the computed solvatochromic shifts have a mean-unsigned-error (MUE) of 3.0 cm^{-1}. The largest errors are due to acetophenone in methanol, carbon tetrachloride and chloroform, each exhibiting unique behaviors.

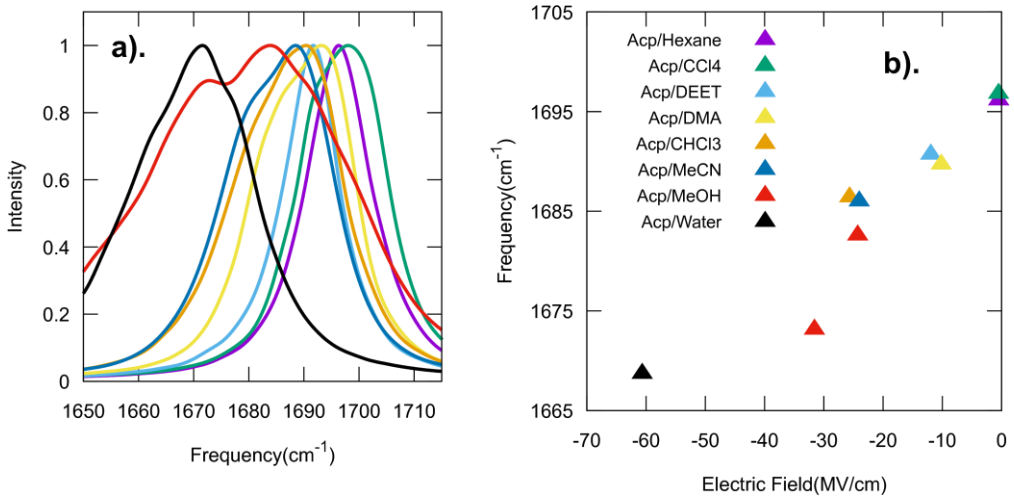

Figure 5.6. a). Calculated infrared spectra of the carbonyl stretch vibration of acetophenone in n-hexane, tetrachloromethane, diethyl ether, N,N-dimethylacetamide, trichloromethane, acetonitrile, methanol, and water. **(b).** Correlation between the computed carbonyl vibrational frequency and the electric field on the carbonyl group. . All results were obtained from molecular dynamics simulations employing the combined PM3/OPLS-AA potential. The PM3 frequencies have been shifted by 240 cm-1 to match the experimental value in the gas phase. A linear regression fit in (b) resulted in $\nu(E_{mode}) = 0.45\, E_{mode} + 1696.4$.

Table 5.4. Computed peak positions from PM3/OPLS-AA simulations, and solvatochromic shifts of acetophenone in various solvents, compared to experimentally measured solvatochromic shifts. Hexane was used as the reference for all of the solvatochromic shifts.

Solvent System	$\nu_{calc}(cm^{-1})$	$\Delta\nu_{calc}(cm^{-1})$	$\nu_{exp}(cm^{-1})$	$\Delta\nu_{exp}(cm^{-1})$
Carbon Tetrachloride	1697.1	0.5	1691.0[a]	-5.4
Hexane	1696.4	0.0	1696.4[b]	0.0
Diethyl Ether	1691.0	-5.4	1692.9[b]	-3.5
N,N-dimethyl acetamide	1690.0	-6.4	-	-
Acetonitrile	1685.3	-11.1	1686.1[b]	-10.3

Chloroform	1686.7	-9.7	1683.3[b]	-13.1
Methanol (0[c])	1682.6	-13.8	1688	-8.4
Methanol(1[c])	1673.2	-23.2	1677	-19.4
Water	1669.0	-27.4	1669.4[b]	-27.0

a. Reference 311
b. Reference 309
c. Number of hydrogen bonds

The carbon tetrachloride simulations shows a small positive shift with respect to hexane and similarly displays a comparable electric field. It is possible that non-electrostatic terms play a significant role in the solvatochromism for this system. For instance, halogen atoms due to their larger size compared to hydrogen display a larger polarizability. However, if we use the Lorentz-Lorenz equation[312] as a way to approximate the isotropic polarizability (see Table 5.5), then we observe a decrease in the polarizability of the solvents as the polarity increases. Carbon tetrachloride has a smaller polarizability than hexane, which suggests that using a polarizable force field may not lead to better results. Instead, halogen bonding may play a role in the experimental solvatochromism.

Table 5.5. Isotropic polarizability computed using the Lorentz-Lorenz equation $\left(\alpha = \frac{3}{4\pi N}\left(\frac{n^2-1}{n^2+2}\right)\right)$, where n is the refractive index and N is the number density of the solvent. The values used in the equation were taken from reference 313. The polarity of each is given using the normalized ET(30) scale.[307]

Solvent System	$\alpha(cm^3)$	ET(30)
Carbon Tetrachloride	6.35	0.052
Hexane	7.15	0.009

Diethyl Ether	5.37	0.117
N,N-dimethyl acetamide	5.78	0.386
Acetonitrile	2.64	0.460
Chloroform	4.85	0.259
Methanol	1.96	0.762
Water	0.87	1.00
Acetophenone	8.72	0.306

The experimental FTIR of acetophenone (see Figure 5.7) of methanol displays interesting behavior. There are two clearly separated peaks, which may be attributed to different hydrogen bonding interactions in the first solvation layer. Similar behaviors have been observed in several studies,[314-316] notably in the work of Gai and coworkers on the carbonyl stretch vibrational frequency shifts of ester compounds in methanol. Gai and coworkers[315] determined an average exchange rate of about 0.1 ps^{-1} between zero and one hydrogen bonds to the carbonyl group in methanol.

To shed light on the origin of the observed twin peaks of the carbonyl stretch vibration of acetophenone in methanol both from experiment and computation, we separated configurations from the molecular dynamic trajectory according to the number of hydrogen bonds, and computed the corresponding frequency shifts (Table 5.4). We used a combination of geometric criteria to define a hydrogen bond, on the basis of donor-acceptor distance (less than 3.3 Å) and deviation from linearity of the hydrogen bond (less than 20° for the acceptor-donor-hydrogen angle). These geometric criteria are based on the minimum of the first solvation peak in the O-O radial distribution functions

between the solute and solvent and are consistent with other studies. We found that 62 %, 33% and 5 % configurations of the entire molecular dynamic trajectory consist of 0, 1, and 2 hydrogen bonds as nearest neighbors, respectively. It is particularly surprising in that a large majority of the solution configurations have no direct hydrogen bonding interactions between methanol and acetophenone, although a large fraction of the structures were also found not to form direct hydrogen bond in the much smaller solute ethyl and methyl acetate in methanol. The greater amount of configurations without nearest hydrogen bonding interactions in the present acetophenone system may be attributed to the relatively larger steric congestion in the proximity of the carbonyl group than that in the ester compounds.

We have determined the average carbonyl stretch frequencies associated with the zero and one hydrogen bonded configurations, and the results match the maximum peak positions of the computed FTIR spectrum very closely (Figure 5.7). This also allows us to fully assign the twin peaks both in the computed and experimental spectra to solvent effects with zero (smaller red-shift from n-hexane solution) and one (greater shift from n-hexane solution) nearest hydrogen bonding interactions. The peak splitting estimated computationally is 9.4 cm^{-1}, in good accord with the experimentally value at 11 cm^{-1}. However, the linewidth of the computational carbonyl stretch vibration of acetophenone in methanol is much broader than that of the experimental FTIR spectrum (Figure 5.7). This difference indicates that the hydrogen bond strength modeled by the present PM3v/OPLS potential may be too weak, although the binding energy is in good agreement with MP2/aug-cc-pVDZ results. The relatively greater peak height

corresponding to the zero-hydrogen bond configuration than that from experiment is also consistent with a somewhat weaker hydrogen bonding interaction between acetophenone and methanol.

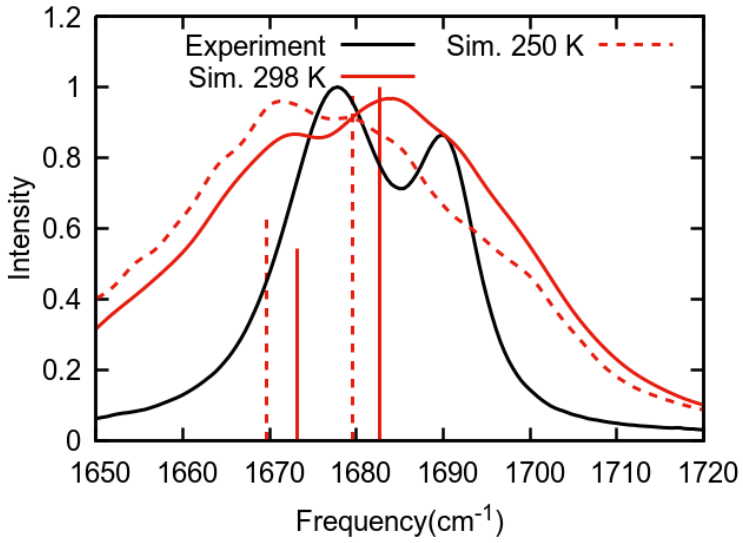

Figure 5.7. Simulated and experimental FTIR spectra for acetophenone in methanol. The vertical lines are the ensemble averaged frequencies for the 0 and 1 hydrogen bonding states, and heights of the lines indicate the relative proportion in the trajectory. The full simulated line was from the trajectory with a temperature of 298 K, and the dashes lines were from a simulation at 250 K.

To further understand the hydrogen bonding interactions in the first solvation layer, we have carried out another simulation of acetophenone in methanol at 250 K. The lower temperature conditions would reduce solvent dynamics, favoring hydrogen bonded configurations. Indeed, this expectation is confirmed by the distribution of hydrogen bonding pattern with 58 %, 37 % and 6 % populations for configurations with the zero, one, and two nearest solvent neighbors, respectively. This represents 4% and 1% increase

in one and two hydrogen bonded complexes at a lower temperature at the expense of the zero hydrogen-bond configurations. Concomitantly, the average vibrational frequencies are red-shifted by 3 to 4 cm^{-1} to 1679.5 and 1669.6 cm^{-1} at 250 K.

The solvation dynamics were studied using two-dimensional infrared spectroscopy (2DIR). Two representative spectra at delay times of 0.2 and 3 ps both from experiment and from computation are shown in Figure 5.8. We observe two overlapping peaks at low waiting time (T_w) in the experimental spectrum and simulated spectrum at 250 K. Interestingly, the computed 2DIR at 298 K displays 3 peaks across the diagonal line, the higher frequency of which may correspond to a somewhat different solvation shell in the overall zero-hydrogen bond ensemble (we have not further investigated the difference). As T_w increases, off-diagonal broadening occurs consistent with hydrogen bond exchange between acetophenone and methanol in both the experimental and the simulation at 250 K. For the simulation at 298 K, the spectral density of the 1 HB state transfers to the 0 HB state due to the population lifetime of the diagonal peaks resulting in a decay of the diagonal peak and a growth of the off-diagonal peak. Taking the ratio of the off-diagonal peak volume and the diagonal peak volume for the zero-hydrogen bonded state resulted in an exponential rise of 2.0 ps for the 298 K spectrum and 0.56 ps for the 250 K spectrum. Interestingly, the former rate compares well with the experimental value of 1.0 +/- 0.8 ps. This difference in the rates can be accounted for by population inversion of the ensembles. At 250 K, there are more oscillators in the single hydrogen bonded ensemble that could undergo a transition to the zero-hydrogen bonded ensemble.

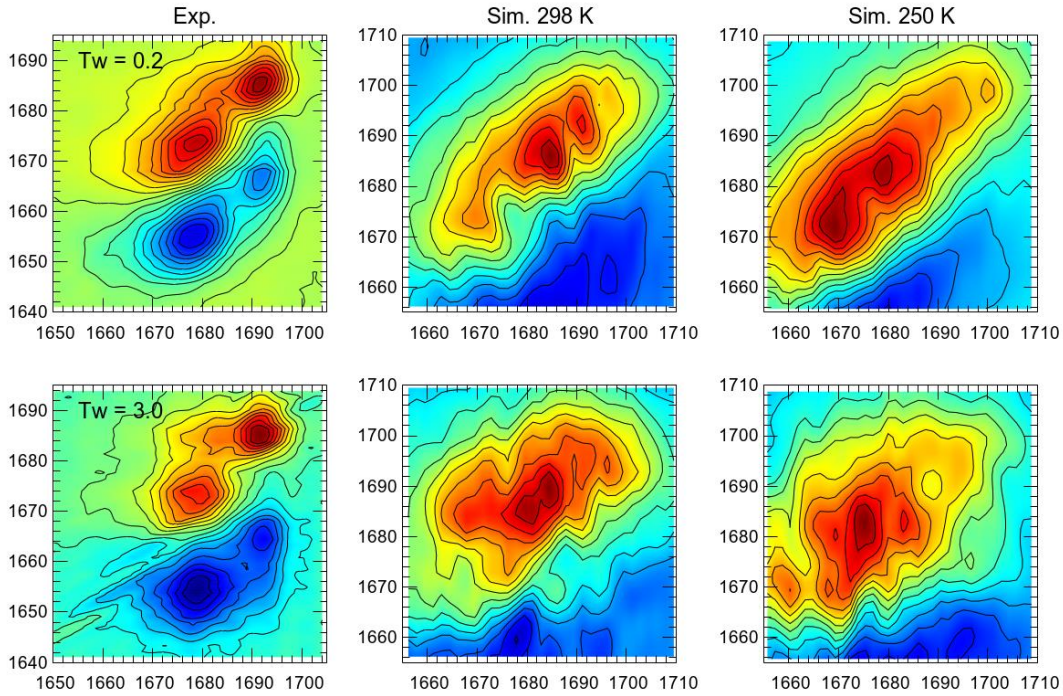

Figure 5.8. 2DIR of acetophenone carbonyl stretch in methanol. The first column is the experimental 2DIR (at 298 K) and the second and third columns are from the simulations at 298 K and 250 K respectively. The rows are for waiting times of 0.2 and 3.0 ps.

The hydrogen-bond correlation function was computed to compare the rise of the off-diagonal peak volume. The hydrogen bond correlation function can be averaged over trajectories that maintain a continuous (unbroken) hydrogen bond or an intermittent hydrogen bond, which includes trajectories in which the hydrogen bond breaks and re-forms. The continuous hydrogen bond correlation function yielded an average lifetime of 0.09 ps and 0.13 ps for 298 K and 250 K, respectively. It is possible that the larger linewidth in the computed FTIR is due to faster exchange of hydrogen bonds leading to a smaller pure dephasing time as compared to experiment. Meanwhile, the average lifetimes for the intermittent hydrogen bond correlation function were 5.0 ps and 8.5 ps.

In both correlation functions, we observe an increase in the lifetime as the temperature is reduced. These observations are consistent with Chuntonov et al.[315] because the population dynamics present in the 2DIR depend on both the exchange rate between ensembles and the probability of each state being occupied.

5.6. Concluding Remarks

Fourier transform infrared (FTIR) spectra for acetophenone in solvents with different polarities, and the two dimensional spectra in methanol have been determined both experimentally and computationally. First, we described the quantum vibration perturbation theory (QVP) for efficient computation of vibrational frequencies of a probe mode in solution, and its implementation in the CHARMM program. To more effectively align the instantaneous structure of a solute molecule in solution sampled during molecular dynamic simulations with the reference configuration, a normal mode weighted transformation approach was introduced to account for molecular symmetry as a modification of the algorithm[317] originally designed for facial recognitions. We further showed that computational accuracy can be significantly improved if the minimum position of the mode motion is matched with the reference state.

The solvatochromism of acetophenone was modelled using second order perturbation, QVP2. The results show reasonable agreement with experiments, with a mean unsigned error of 3.1 cm^{-1} for the computed solvent shifts using the PM3/OPLS-AA potential. Experimental FTIR of acetophenone in methanol showed a double crested peak, which was reproduced by simulation. The results of the simulation suggest that it is possible to definitively assign the two peaks as the 0 and 1 hydrogen bond states

between acetophenone and methanol. 2DIR was then simulated to test the capability of QVP2 in modelling dynamics and compared reasonably well to experiment. Overall, this shows that QVP2 can be applicable to systems with small differences in the vibrational frequency, such as a solvatochromic series or be used in monitoring dynamics through 2DIR.

Chapter 6. Enhanced Vibrational Solvatochromism and Spectral Diffusion by Electron Rich Substituents on Small Molecule Silanes

Adapted with permission from C.M. Olson, A. Grofe, C.J. Huber, I.C. Spector, J. Gao, and A.M. Massari, J. Chem. Phys. **147**, 124302 (2017).

This work was performed in collaboration with the Massari group. All experiments were performed by Courtney M. Olson, Christopher J. Huber and Ivan C. Spector.

6.1. Introduction

Solvent motions play a critical role in chemical reactivity and solvation dynamics.[318-321] Perhaps the most obvious example is found in electron transfer reactions in which solvent shell dynamics contribute the energy needed to reach the transition state geometries of the donor and acceptor species.[322, 323] In fact, for any condensed phase reaction, solvent-solute interactions can stabilize or destabilize the transition state, thereby directly influencing the rate coefficient.[324-328] For example, in biomacromolecules, key structural motions for the function of proteins or enzymes can be slaved to the dynamics of the surrounding solvation layer.[329-334] Likewise, catalytic rate constants are always specific to a solvent system,[335-338] and ultrafast dynamics in the solvation shell have

been directly correlated with proposed mechanistic steps for organometallic catalysts.[339, 340]

A variety of approaches have been used to characterize solvent dynamics.[298, 341-351] All of these techniques report some facet of solvent motions, but none of them delivers the full dynamic picture. Complete structural evolution is filtered by the sensitivity of the reporter to each dynamic component, and only a subset of the coupled dynamics is visible through the lens of a particular measurement technique. For example, two-dimensional infrared (2D-IR) spectroscopy monitors the time dependent frequency fluctuations of a vibrational mode on a solvated solute species.[298, 348-350, 352] Changes in the vibrational frequency are dependent on the time scales of solvent motions in the proximal solvation shell and the degree to which those motions perturb the vibrations of the solute. The latter effect depends on solvent polarity and the strength of solute-solvent interactions – generally only the closest solvation shells exert a measurable influence on frequency fluctuations of the solute.[318, 319, 321, 340] Therefore, the 2D-IR spectrum of a particular solute vibrational mode is blind to solvent motions in the bulk and even excludes dynamics in the solvation shell that do not perturb its vibrational frequency. In this context, molecular dynamics (MD) simulations can complement experimental measurements to provide detailed, structural insights into the microscopic mechanism of solvation.[331, 353-362]

In this work, we report a combined experimental and computational investigation of vibrational solvatochromism and spectral diffusion in small silane molecules in various solvents using FTIR and 2D-IR spectroscopies. To elucidate substituent effects on solvation dynamics, trimethoxysilane (TriMOS) and triphenylsilane (TriPS) were chosen in our study since the same vibrational mode can be monitored in the presence of

different electron withdrawing ligands, giving rise to different solvatochromic responses. The study of these model molecules reveals the role of substituents on spectral diffusion in different solvents. The time scales and amplitudes of spectral diffusion are extracted from the 2D-IR data, which are further analyzed through molecular dynamics (MD) simulations, in which each solute molecule is represented explicitly by a quantum mechanical method, embedded in the solvent environment approximated by a molecular mechanics force field. Such a combined QM/MM potential to treat solute-solvent interactions allows a direct probe of the effect of solvent dynamics on the instantaneous change of the solute potential energy surface and its vibrational frequency as measured experimentally.

6.2. Experimental Methods

Trimethoxysilane (TriMOS, 95%, Sigma-Aldrich), triphenylsilane (TriPS, 97%, Sigma-Aldrich), chloroform (99.9% purity, anhydrous, Acros Organics), isopropanol (99.5%, anhydrous, Sigma-Aldrich), and pentane (*n*-pentane, 98%, Sigma-Aldrich) were used as received.

TriPS and TriMOS solutions were prepared in each solvent as 5% wt/vol and 5% vol/vol solutions, respectively, giving absorbances of 100 – 200 mOD for the Si-H vibration on both solutes. Solutions were used within 1 week of preparation. Spectroscopic studies were performed on solutions sandwiched between two 3 mm CaF_2 windows with a 50 μm Teflon spacer to define the sample path length.

Fourier transform infrared (FTIR) spectra were collected on a Nicolet 6700 FTIR spectrometer (Thermo Scientific) with at least 16 scans and a resolution of 1 cm^{-1}. A

background spectrum of each of the solvents was subtracted from the respective TriMOS and TriPS spectra.

The 2D-IR instrument has been described previously.[294] The mid-IR pulses were tuned to the Si-H stretching frequency (2200 cm^{-1} for TriMOS and 2130 cm^{-1} for TriPS). All of the 2D-IR spectra were analyzed using the centerline slope (CLS) method, and then iteratively fit with the linear lineshape to obtain the frequency-frequency correlation function (FFCF) as a homogeneous term plus a sum of exponentials: $FFCF(t) = \frac{\delta(t)}{T_2} + \Delta_1^2 \exp\left(\frac{-t}{\tau_1}\right) + \Delta_2^2 \exp\left(\frac{-t}{\tau_2}\right)$.[300, 363] IR pump-probe spectroscopy was carried out with the pump and probe beams polarized at the magic angle to remove contributions from orientational relaxation,[364] as described previously.[295] The data were fit from 1 to 75 ps to determine the population relaxation times (lifetime, T_1) for the v = 0-1 and 1-2 transitions. The vibrational relaxation times for these two transitions were consistently the same within error, and the 0-1 values were used in data analyses.

The computational analysis followed a two pronged approach: (1) density functional theory (DFT) calculations were performed with two continuum solvation models using the M06-2X functional along with the 6-31+G(d,p) basis set, and (2) combined quantum mechanical and molecular mechanical (QM/MM) simulations were carried out to understand the microscopic solvation dynamics of the vibrational chromophore. DFT calculations and subsequent analyses were performed using Gaussian 09.[365] The QM/MM simulations were performed using CHARMM,[366] in which the solute is treated by the semiempirical Austin model 1 (AM1) method[367] to provide an adequate sampling of the configuration space. For each solvent, the molecular dynamics were executed for 2 ns

with 1 fs integration time-step with periodic boundary conditions at 1 atm of pressure and 25 ^{o}C of temperature. The simulations boxes were configured to contain enough molecules to fill a roughly (45 Å)^3 box. Coordinates were saved every 10 fs, resulting in a total of 200,000 configurations, which were used for all subsequent analyses.

The instantaneous vibrational frequency of the silicon hydride mode at a given solvent configuration was determined using a vibration quantum-mechanical perturbation theory (QVP) that was developed recently.[368] In this approach, the effects of solute-solvent interactions on the vibrational wave function and transition energies of the solute are treated as a perturbation to a reference state. In the present study, the reference vibrational state was the vibrational wave function at time zero after the initial equilibration for data collection (which can be regarded as an arbitrary moment in time during the MD simulation). Numerically, the wave function of the reference state was modeled using the potential optimized discrete variable representation (PO-DVR).[369-371] In this manner, the changes in wave function for the ground state and the first two excited states due to the instantaneous solvent fluctuations as well as the change in solute geometry at future times were determined by perturbation theory. Although second-order perturbation yields sufficient precision (~1 cm^{-1}), we used the fourth-order perturbation theory (QVP4) thanks to the computational efficiency using the present QM/MM potential, which ensures that the computed vibrational frequencies are within 0.5 cm^{-1} of the exact result for each configuration. Because a discrete variable representation is employed, the calculation of the perturbation operator only requires single point energy calculations at the PO-DVR points without the need to explicitly solve the vibrational

Schrödinger equations. Consequently, the QVP4 approach is computationally efficient, providing the instantaneous, on-the-fly transition energies of the solute for the 0-1 and 1-2 excitations. Importantly, nuclear quantum mechanical effects as well as solvent dynamics on the solute potential energy surface are explicitly included in the computation, although nuclear quantum effects on solute-solvent coupling are neglected. A complimentary alternative approach is the widely used electrostatic potential mapping procedure. Further details concerning the QVP implementation are given in Chapter 5. Overall, the QVP4 calculations captured the time-dependent evolution of the vibration excitation energies of the solute, which were used to model the linear and nonlinear absorption spectra and the FFCF.[372]

The hydrogen bonding lifetime (τ_{HB}) of the solvent was determined by calculating the hydrogen bond correlation function.[373, 374]

$$C(t) = \left\langle \frac{\sum h_{ij}(t_0) h_{ij}(t + t_0)}{\sum h_{ij}(t_o)^2} \right\rangle \qquad (6.2.1)$$

where $h_{ij}(t)$ is unity when the pair of solvent molecules *i* and *j* are hydrogen bonded, and zero otherwise. The computed correlation function was fitted to a set of three exponentials,[373-375] and the average τ_{HB} was determined by integrating the correlation function. For these calculations, a hydrogen bond was defined by geometrical criteria such that the donor-acceptor distance was less than 3.0 Å and the OH–O angle was greater than 130°. This methodology has been implemented into the MdAnalysis library in Python[375] and possibly underestimates the lifetime since it does not take into account instances of transient breaking and reforming of the same bond.

Before concluding this section, we make a distinction in the trajectories used to determine correlation functions. First, there is the molecular dynamics trajectory, which encompasses the entirety of the dataset from which the correlation function is calculated. Second, there are correlation trajectories, which are a subset of the molecular dynamics trajectory, upon which the correlation function is averaged at each point in the correlation function. In the calculation of the hydrogen bond correlation function, correlation trajectories were only accepted if the hydrogen bond was continuous throughout the correlation trajectory. This could in principle underestimate the hydrogen bond lifetime because it does not include transient breaks of the hydrogen bond. However, this is compensated for by using a generous hydrogen bond geometric criteria of 3 Å for the hydrogen-acceptor distance and 130° for the donor-hydrogen-acceptor angle. This algorithm was further modified to calculate the hydrogen bond lifetime at the solute-solvent interface by only including correlation trajectories that were within the first shell of the solvent. The first shell was determined by having any distance between the atoms of the solute and the atoms of each solvent molecule be less than 6 Å, the minimum following the first peak of the radial distribution function (Figure 6.2.c) between the central carbon of isopropanol and the hydride hydrogen.

6.3. Results and Discussion

Shown in Figure 6.1.a are the solvent-subtracted FTIR spectra for the silicon hydride, Si-H, stretching vibration of TriMOS and TriPS in three different solvents: isopropanol, chloroform, and pentane. A most striking finding is the large substituent effect on the silane stretch mode; its vibrational frequency is blue-shifted by 74 cm^{-1} when the phenyl

groups of TriPS are replaced with the electron-withdrawing substituents in TriMOS in the non-polar solvent pentane. The experimental finding on the effect of CH_3O-substitution on the Si-H frequency in pentane is reproduced by the computational results of 78 and 81 cm^{-1} using, respectively, the Minnesota solvation model (SMD)[376] and the polarizable continuum model (PCM)[377] at the M06-2X/6-31+G(d,p) level of theory (Table 6.1). The corresponding change of 59 cm^{-1} was obtained from QM/MM molecular dynamics simulations (Table 6.2). The TriMOS hydride stretch frequency (ν_{Si-H}) also exhibits a strong hypsochromic change with absorption peak maxima at 2194.6, 2203.2, and 2207.2 cm^{-1} in isopropanol, pentane, and chloroform, respectively. Similarly, the corresponding values for TriPS are 2125.7, 2129.2, and 2131.1 cm^{-1}. The experimental trend of solvatochromic shift in order of isopropanol < pentane < chloroform for ν_{Si-H} is surprising in that it does not follow any solvent polarity scales. Continuum model calculations, explicit MD simulations, and experiments predict the vibrational frequency to decrease monotonically with the solvent polarities (polarity trend: pentane < chloroform < isopropanol), in accordance with the Stark effect.[153] Interestingly, although the trend is the same, TriMOS and TriPS experience different degrees of solvatochromism. It has been established that ν_{Si-H} is tuned by the inductive effect of the substituents.[378-382] A major difference between TriMOS and TriPS is the presence of electronegative oxygen atoms in the methoxy ligands that strongly polarize the Si-O bonds; the partial atomic charge on silicon changes from 0.08 *e* in TriPS to 1.03 *e* in TriMOS (Table 6.1). Previous analysis showed that the hydrogen bonding ability of the solvent was correlated with solvatochromic shifts of ν_{Si-H} on silanes and silica sol-gels.[383] Consequently, we

hypothesized that the solvent interactions with the oxygen atoms would have the greatest influence on the vibrational mode due to the inductive effect.[383, 384] Yet, the fact that the solvatochromic trend in Figure 6.1.a is the same for TriPS, which lacks oxygen atoms in its ligands, indicates that the solvent influence is not limited to this specific interaction.

Table 6.1. Normal mode vibrational frequencies for the Si-H stretch (cm^{-1}) of trimethoxysilane (TriMOS) and triphenylsilane (TriPS) in the gas phase and in pentane, chloroform and isopropanol solution using M06-2X/6-31+G(d,p) with the Minnesota solvation model (SMD), and the polarizable continuum model (PCM). And gas phase CHELP partial atomic charges (a.u.)

Solecule	Solvent	ν_{SiH} SMD (cm^{-1})	$\Delta\nu_{SiH}$ SMD (cm^{-1})	ν_{SiH} PCM (cm^{-1})	$\Delta\nu_{SiH}$ PCM (cm^{-1})	Si Charge SMD	H Charge SMD
TriMOS	gas	2342.3	0.0	2342.3	0.0	1.03	-0.17
	pentane	2337.0	-5.3	2339.6	-2.7	1.05	-0.17
	chloroform	2334.8	-7.5	2338.3	-4.0	1.05	-0.16
	isopropanol	2342.1	-0.2	2338.8	-3.5	1.05	-0.15
TriPS	gas	2260.8	0.0	2260.8	0.0	0.08	-0.08
	pentane	2258.7	-2.1	2258.6	-2.2	0.08	-0.08
	chloroform	2256.3	-4.5	2257.5	-3.1	0.09	-0.08
	isopropanol	2255.6	-5.2	2257.1	-3.7	0.04	-0.07

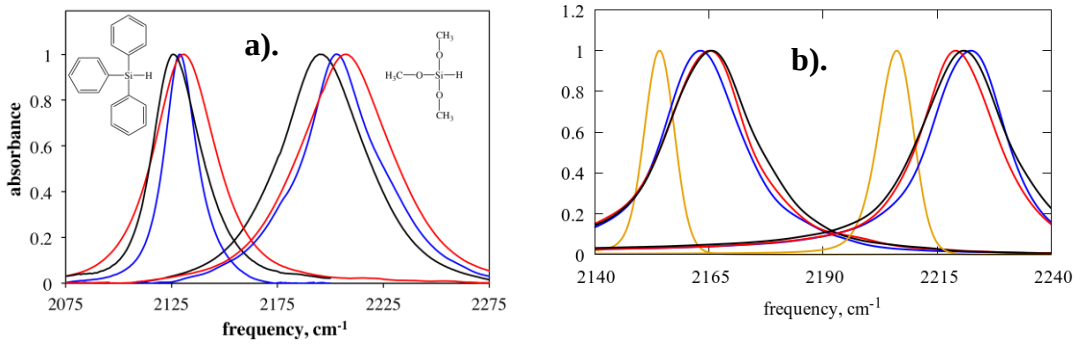

Figure 6.1. a). Solvent subtracted, baselined, and normalized FTIR spectra of the Si-H vibration for TriPS (left) and TriMOS (right) in isopropanol (black), chloroform (red), pentane (blue), and gas phase (orange). This coloring convention is used throughout. **b).** Computed linear spectra in the Si-H stretch vibrational frequency region for TriPS (left) and TriMOS (right).

To gain insights into the solvatochromism for TriMOS and TriPS, we modeled the $\nu_{Si\text{-}H}$ vibrations through a combination of DFT calculations on solutes using two continuum solvent models (SMD[376] and PCM[377]) and MD simulations. Continuum solvation methods introduce the equilibrium electric polarization into the Born-Oppenheimer surface, probing the Stark effect on the vibrational frequency, but the unusual trend of the Si-H vibrational frequency shifts observed experimentally was not fully reproduced by either continuum modelsF. In particular, the simulations yielded the correct relative frequency shifts for TriPS between pentane and chloroform solvents, but not in isopropanol, and for TriMOS the order between pentane and isopropanol was correct, yet not in $CHCl_3$. We suspect that the large dispersion contributions from chloroform are partly responsible for the unusual experimental findings. The DFT/SMD calculations yielded a large blue shift for TriMOS in isopropanol, a clear departure from other computational methods and experiments. Nevertheless, the trends obtained using

the PCM model and QM/MM simulations are in agreement with each other, suggesting that dielectric and electrostatic interactions are consistently represented. The SMD model includes contributions due to surface tension terms, which may be too sensitive in the Hessian for the present systems.

A plausible explanation for the unusual frequency trends is that specific solvent-solute interactions that were not captured by implicit solvent modeling might be needed to reproduce the experimental order of spectral change. In calculations with TriMOS, the inclusion of an explicit H-bond donor (methanol) near the oxygen atoms of the methoxy ligands was able to yield the red spectral shift observed in isopropanol relative to that in pentane. Similarly, introducing an explicit $CHCl_3$ solvent molecule in the solvation shell of TriMOS led to a mild blue shift (6.8 cm^{-1}), which could be further enhanced by constraining the solvent geometry to maintain a halogen bonding configuration to the hydride.[385, 386] The fact that this configuration was not maintained for this single $CHCl_3$ molecule indicates that the halogen bond is not the most stable interaction, however, solvent packing effects in the condensed phase would lead to this interaction being more significant. In addition, the radial distribution functions between the hydrogen of the silane mode and the chlorine of chloroform (Figure 6.2.a) in our simulations of both TriPS and TriMOS show a moderate peak at roughly the same distance as the halogen bond determined by the constrained QM geometry optimization. The integrals of the distribution peaks show that their occupations are greater than one, which suggests that on average the halogen bond is maintained through most of the simulations. We conclude that the unusual experimental solvatochromic trend for $\nu_{Si\text{-}H}$ is understood as

arising from specific hydrogen and halogen bonding interactions with the solute. Given that the solvatochromism is not fully reproduced from QM/MM suggests that non-electrostatic effects, such as dispersion and charge transfer, also play a role for $CHCl_3$.

An interesting finding from our analyses is that the magnitudes of the partial atomic charges for silicon and hydrogen – the main components of the normal mode vector – increase with the electronegativity of the ligands (Table 6.1). This provides an explanation for the greater solvatochromic effects in TriMOS than in TriPS: the electron withdrawing methoxy ligands lead to a greater charge separation and electrostatic coupling to the solvent reaction field.[153] Consequently, the average dipole moment for TriMOS is increased from 1.8 D in pentane to 2.5 D in isopropanol, whereas the corresponding values are 0.8 and 1.2 D, respectively, for TriPS.

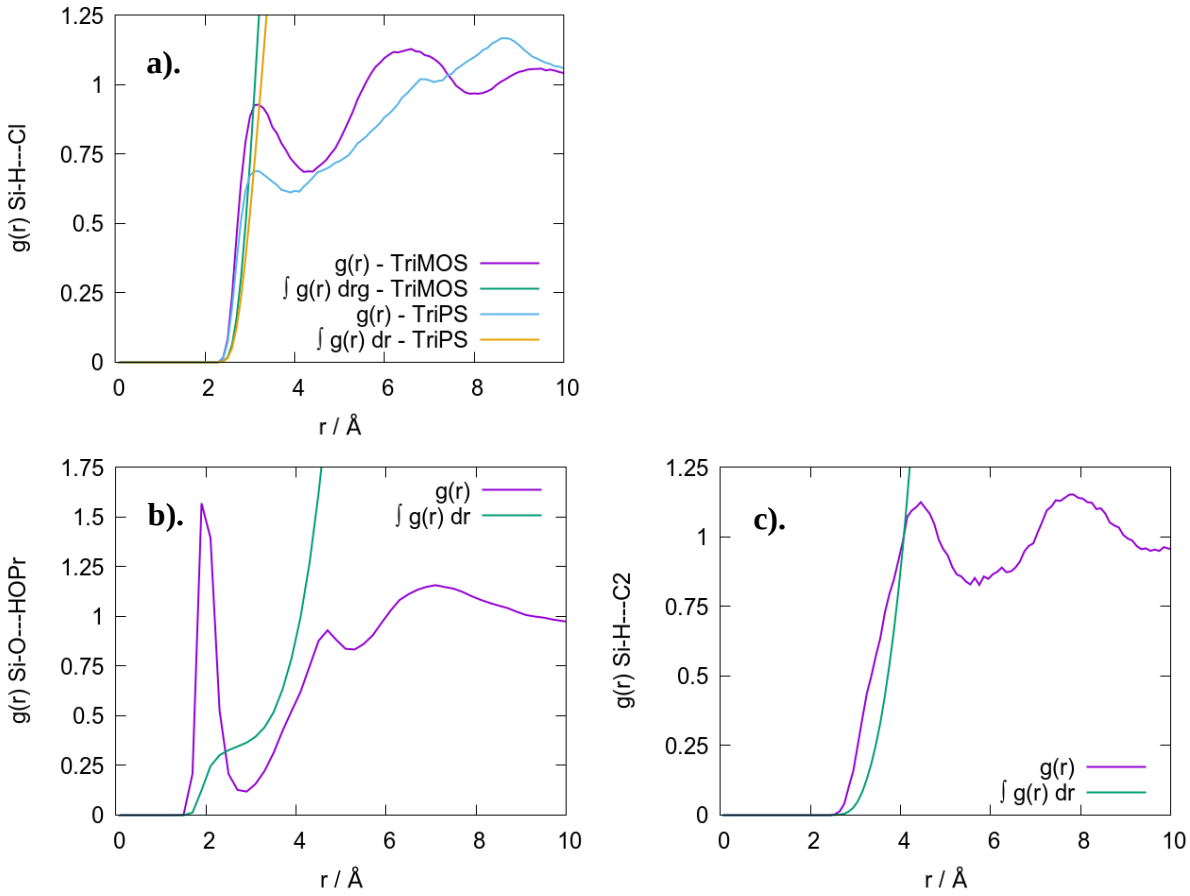

Figure 6.2. Radial distribution functions (TriMOS:purple, TriPS:blue) and integrated radial distribution function computed from the AM1/CHARMM MD simulations. (TriMOS:green, TriPS:yellow). **a).** Between silane hydrogen and chlorine atoms of chloroform. **b).** Between the hydrogen bond acceptor in TriMOS and the hydrogen donor in isopropanol. **c).** Between silane hydrogen and the central carbon of isopropanol.

One key question is whether a change in solvatochromism correlates with increased sensitivity to ultrafast structural dynamics leading to spectral diffusion. If so, this would provide a strategy to designing vibrational probes with enhanced sensitivity to solvent dynamics by tuning peripheral ligands. As a starting point, we note that the FTIR peak widths vary considerably among the three solvents for both compounds, increasing in

order of pentane (blue) < isopropanol (black) < chloroform (red). The TriPS peak widths are generally narrower than those of TriMOS, though the broadening trend with solvent remains the same. The FTIR peak widths are influenced by the range of chemical environments as well as the time dependent fluctuations of the vibrational frequencies that are driven by solvent dynamics (spectral diffusion and homogeneous broadening). Broader peaks in more polar solvents suggest that their solvation environments are more heterogeneous and/or dynamic than that of pentane. 2D-IR spectroscopy enables one to decompose the FTIR lineshapes into their homogeneous and inhomogeneous contributions, and MD simulations can be used to understand the molecular origins of the experimental data.[303, 349, 352] The full-widths-at-half-maximum (FWHM) determined from molecular dynamics simulations show similar trends both for the two solutes and in different solvents, although the linewidths are somewhat smaller than those from experiments (Table 6.2). Thus, the present QM/MM simulations can provide useful insights on properties of solvent dynamics.

Table 6.2. Computed Si-H stretch vibrational frequencies (cm-1) and full width at half max (FWHM) peak widths (cm^{-1}) of trimethoxysilane (TriMOS) and triphenylsilane (TriPS) in the gas phase and in pentane, chloroform and isopropanol solution using quantum vibrational perturbation theory in combined QM/MM molecular dynamics simulations. The solute is treated by the AM1 Hamiltonian and the solvents are represented by the CHARMM force field. The experimental data are also listed for convenience of comparison.

molecule	solvent	Experiment		Calculation		
		ν_{SiH} (cm^{-1})	FWHM (cm^{-1})	M06-2x/6-31+G(d,p)/SMD	AM1/CHARMM	
				ν_{SiH} (cm^{-1})	ν_{SiH} (cm^{-1})	FWHM (cm^{-1})
TriMOS	gas			2342.3	2206.2	9.1
	pentane	2203.2	41	2337.0	2222.4	19.3
	chloroform	2207.2	50	2334.8	2219.1	19.8
	isopropanol	2194.6	46	2342.1	2220.9	22.5
TriPS	gas			2260.8	2154.2	7.8
	pentane	2129.2	18	2258.7	2163.2	19.3
	chloroform	2131.1	35	2256.3	2165.2	19.8
	isopropanol	2125.7	27	2255.6	2165.6	22.5

Figure 6.3 shows the 2D-IR spectra at T_w = 0.3 ps (left column) and 3 ps (right column) for TriMOS in isopropanol (top row) and pentane (bottom row). An intuitive interpretation of these spectra is that the x-axis (ω_1) corresponds to the frequencies at which a subensemble of oscillators is excited by the first IR pulse and the y-axis (ω_3) is the range of frequencies that this subensemble exhibits after sampling its surroundings for a specific waiting time, T_w. Hence, the 2D-IR spectrum yields a frequency-frequency time correlation for the subensembles beneath the FTIR line shape.[298, 348-350, 352, 387] Each spectrum has a positive-going (red) v=0-1 peak that lies on or above the diagonal and a

negative-going (blue) v=1-2 peak that is shifted by the anharmonicity to lower frequencies along the ω_3 axis. A diagonal slice through the 0-1 peak reflects the range of frequencies captured by the linear FTIR lineshape (assuming sufficient separation between the 0-1 and 1-2 peaks); the antidiagonal width represents the portion of the available frequencies that have been sampled during a given T_w period. This antidiagonal width contains contributions from very fast pure dephasing (T_2*) and relaxation (T_1), as well as spectral diffusion caused by interconversion of molecular subensembles and driven by the reorganization of solvent molecules.[300, 303, 363]

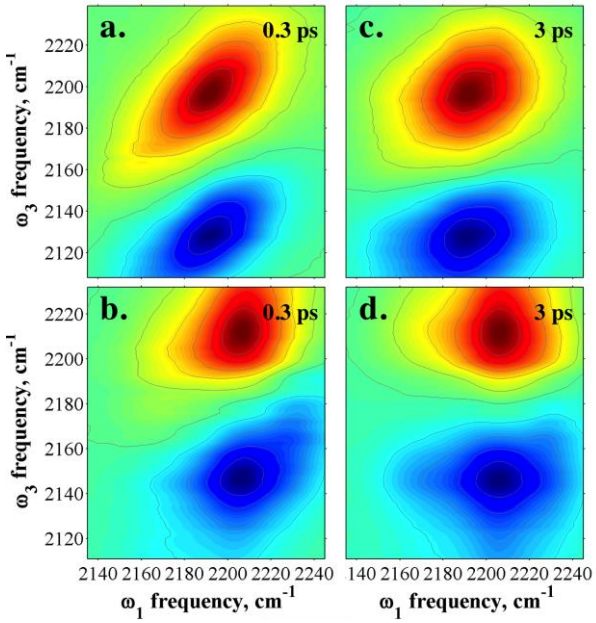

Figure 6.3. 2D-IR spectra collected at T_w = 0.3 (left column) and 3 ps (right column) for the $\nu_{Si\text{-}H}$ mode on TriMOS in isopropanol (a,c) and pentane (b,d).

For TriMOS, we observe in Figures 6.3.a and 6.3.b that at short T_ws the peak shape is diagonally elongated, indicating that the Si-H oscillators have not yet sampled the full range of solvation environments. Comparison of these two contour plots reveals that the

spectrum in isopropanol is more elongated along the diagonal direction than that in pentane; the Si-H mode of TriMOS has either sampled a greater range of the available solvent configurations in pentane than in isopropanol in the first 300 fs, or there are less structural dynamics in the non-polar solvent. As the waiting time increases, the 2D-IR contour shapes become more circular, reflecting the loss of correlation due to spectral diffusion of the $\nu_{Si\text{-}H}$ oscillators (Figures 6.3.c and 6.3.d). By 3 ps, the 2D-IR spectral shape in pentane is nearly circular while some diagonal elongation persists in isopropanol at this T_w, revealing that the time scale of solvent shell rearrangements is slower in isopropanol.

To quantify these dynamic differences, we analyzed the centerline slope (CLS) for the v=0-1 peaks at all T_ws for both molecules in all three solvents. Figure 6.4 shows the CLS values as a function of T_w along with multiexponential fits for TriMOS and TriPS in isopropanol, chloroform, and pentane. The CLS decays in isopropanol can be adequately represented by a double exponential fit for both TriMOS and TriPS, while a single exponential function is sufficient for the CLS decays in chloroform and pentane. This suggests that the solvent dynamics in chloroform and pentane enable all of the Si-H oscillators for both TriMOS and TriPS to experience all of the available frequencies under the linear lineshape by about 5 ps. In contrast, some $\nu_{Si\text{-}H}$ oscillators remain partially correlated with their starting frequencies in isopropanol for both molecules since the CLS decays have not yet reached the baseline.

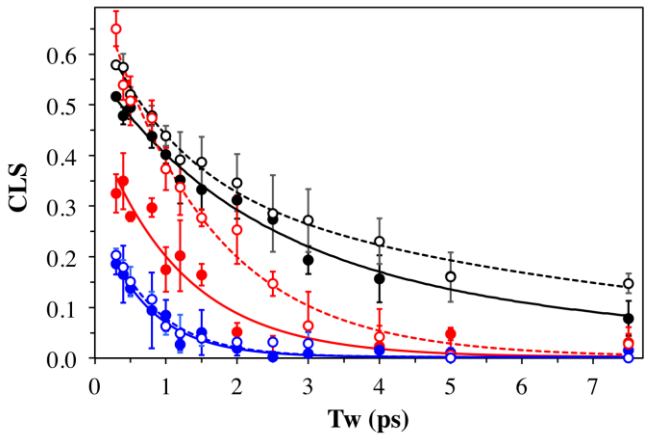

Figure 6.4. CLS decays as a function of T_w for TriMOS (solid markers) and TriPS (open markers) in isopropanol (black), chloroform (red), and pentane (blue). Overlaid are solid curves (TriMOS) and dotted curves (TriPS) to show multiexponential fits to the data described in the text. The markers are the average CLS values and the error bars are the standard deviations.

The CLS decays represent the normalized FFCFs, but they can be used to obtain the full FFCFs by iteratively fitting the CLS decays and the linear lineshapes,[300, 363] thereby separating the homogeneous and inhomogeneous contributions to the FTIR spectra. The resulting FFCF parameters are given in Table 6.3 and can be categorized as unresolvably fast (Γ), fast spectral diffusion (~1 ps), and slow spectral diffusion (~10 ps). Vibrational dynamics are the fastest and the lowest amplitude in pentane, characteristic of a solvent that interacts very weakly with itself and couples very weakly to the $\nu_{Si\text{-}H}$ mode. Polar and strongly interacting solvents such as chloroform (weak H-bond donor) and isopropanol (strong H-bond donor and acceptor) exhibit slower, larger amplitude frequency fluctuations in the FFCF. The homogeneous linewidths are similar for molecules in the same solvent and track inversely with the solvent polarity. Pentane exhibits the widest homogeneous linewidths for both solute molecules, despite having the

narrowest FTIR peak widths; the ν_{Si-H} mode in TriPS is more homogeneously broadened. The FTIR lineshapes in chloroform and isopropanol are dominated by inhomogeneous broadening.

Table 6.3. FFCF parameters for TriPS and TriMOS in isopropanol, chloroform, and pentane.

Solute	Solvent	Δ_1 (cm^{-1})[a]	τ_1 (ps)[b]	Δ_2 (cm^{-1})[a]	τ_2 (ps)[b]	Γ (cm^{-1})[a]
TriMOS	isopropanol	16 (±4)	2.0 (±0.5)	12 (±4)	7 (±2)	6 (±2)
	chloroform	23 (±5)	1.2 (±0.2)	-	-	7 (±3)
	pentane	10 (±4)	0.7 (±0.1)	-	-	13 (±2)
TriPS	isopropanol	8 (±3)	1.1 (±0.6)	8 (±2)	8 (±3)	5 (±1)
	chloroform	15 (±2)	1.5 (±0.09)	-	-	6.1 (±0.7)
	pentane	8 (±1)	0.72 (±0.07)	-	-	7.9 (±0.2)

[a] errors show the range of which that parameter could be increased while the other parameters floated to fit the FTIR line shape 98% as well as the best value
[b] standard error of the exponential fit.

Interestingly, the amplitudes are statistically greater for TriMOS than TriPS in isopropanol and chloroform. The time scales of the dynamics sensed by these two species are the same, but they apparently have a larger influence on the Si-H mode for TriMOS. We have hypothesized previously that specific solvent-solute interactions with the oxygen atoms bound to a silicon site might be responsible for the enhanced solvatochromism in molecules such as TriMOS.[384, 388] However, the FFCFs presented

here for TriMOS, which has oxygen-bearing ligands, and TriPS, which lacks oxygen atoms, disprove this hypothesis since the ν_{Si-H} on both molecules senses the same dynamics. Recall that DFT calculations above showed that enhanced solvatochromism arises from increased coupling of ν_{Si-H} to the reaction field due to mode polarization by the substituents. Here, we find that this polarization also enhances spectral diffusion.

The FFCFs for ν_{Si-H} on TriPS and TriMOS in isopropanol also exhibit a similar, slower dynamic contribution (Δ_2 and τ_2). Since the hydrogen atom of the Si-H group carries a negative partial charge (Table 6.1), it is not expected to donate a hydrogen bond to isopropanol, and such binding interactions have not been observed in silanes.[381] Similarly, hydrogen bonding interactions with the ligands are also ruled out by the lack of a hydrogen-bond acceptor in TriPS. Consequently, we attribute the slower component to the hydrogen bonding dynamics of isopropanol with itself since the time scale is similar to what has been reported.[389-392] To confirm this hypothesis, we computed the FFCFs from QM/MM simulations, which were fitted to a combination of three exponentials plus a constant offset. Overall, the parameters obtained from the computed FFCFs (Table 6.4) are in accord with those determined from experiment (Table 6.3). Similar to experiment, both probes in isopropanol required two additional inhomogeneous exponential terms to describe the FFCF, while all of the other FFCFs only required one. Additionally, the time constants for the second exponential are in reasonable accord with the lifetime of hydrogen bonds.[389-392] The third exponential contains dynamics that are motionally narrowed and would contribute to the homogeneous linewidth (Γ).

Table 6.4. Computed FFCF parameters for TriPS and TriMOS in the three solvents.

Solute	Solvent	Δ_1 (cm^{-1})	τ_1 (ps)	Δ_2 (cm^{-1})	τ_2 (ps)	Δ_3 (cm^{-1})	τ_3 (ps)
TriMOS	isopropanol	6.8	1.4	3.8	9.3	28.1	0.06
	chloroform	6.6	1.7	-	-	25.1	0.07
	pentane	3.3	1.9	-	-	27.1	0.06
TriPS	isopropanol	9.3	0.90	5.0	6.3	30.4	0.06
	chloroform	10.3	1.67	-	-	32.4	0.08
	pentane	8.9	0.84	-	-	29.56	0.06

The fast inhomogeneous spectral diffusion component (Δ_1 and τ_1) is ascribed to collective motions of bulk solvent molecules approximately resembling a dielectric continuum. Here, solvent molecules are indistinguishable, and coherent movement of the collection together leads to a variance in the electric field that is higher than the noise of the individual molecules. Spectral diffusion can be modeled here as a time-dependent Stark effect: the motions that lead to the largest variance in the electric field on the mode are those that contribute most strongly to the FFCF and are the basis for attribution of the signal lifetimes.

The FFCFs for the simulated solutes in isopropanol require a component (Δ_2 and τ_2) with a correlation time that is longer than the continuum motions. This is attributed to the reorganization of the isopropanol hydrogen bond network. It cannot be due to hydrogen bonding with the solute since it is present in the TriPS/isopropanol system as

well. The hydrogen bond lifetime (τ_{HB}) of isopropanol was calculated as described in the Experimental section. Table 6.5 presents the τ_{HB} values for the first solvation shell molecules (defined as having a distance less than 6.0 Å to the solute) around TriMOS and TriPS, as well as for the bulk solvent. Hydrogen bonds exchange faster in the bulk solvent, but the τ_{HB} of the first solvation shell species are more relevant to the FFCF of $\nu_{Si\text{-}H}$ on the solutes. The τ_{HB} in the solvation shell are in excellent agreement with τ_2 in the FFCFs obtained by MD simulations, strongly supporting the assignment that τ_2 dynamics in the experimental FFCFs originate from solvent shell hydrogen bond dynamics.

Table 6.5. Hydrogen bond lifetimes (τ_{HB}) in isopropanol simulations.

Solvent environment	$\tau_{HB/bulk}$ (ps)	$\tau_{HB/first\ shell}$ (ps)
TriMOS / isopropanol	4.15	9.3
TriPS / isopropanol	4.18	8.3
bulk isopropanol	4.88	-

The autocorrelation functions of solvent dipole moments (DAFs) were calculated for individual solvent molecules in the solvation shell around TriMOS and TriPS (Figure 6.4). Because the bond lengths of the solvent molecules are constrained using SHAKE,[393] the DAFs only contain angle bending, torsional modes, and rotational motions of each solvent molecule. Isopropanol and chloroform both display exponential decay behavior, characteristic of rotational motions. Pentane shows damped oscillatory behavior, suggesting that the DAF is dominated by torsional and bending modes rather than rotation. The DAFs of chloroform and isopropanol were fitted to a sum of three and four exponentials, respectively, to adequately quantify the dipole dynamics (Table 6.6).

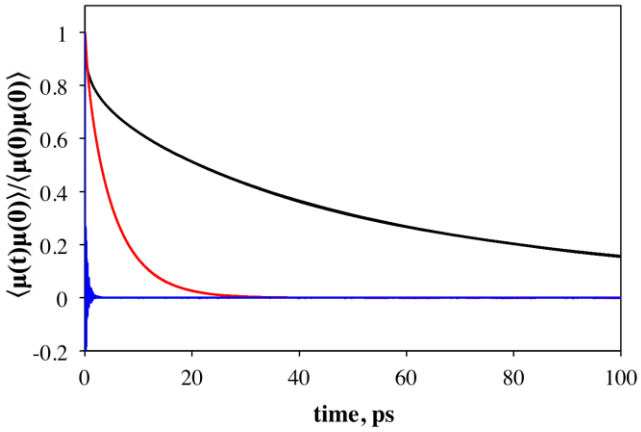

Figure 6.5. Normalized dipole autocorrelation function (DAF) for individual solvent molecules in isopropanol (black), chloroform (red), and pentane (blue).

The DAF parameters for chloroform and isopropanol show the largest contribution to decorrelation from the slowest process (Table 6.6), which we attribute to rotation of the whole molecule. Of the two solvents, molecular rotation in chloroform is significantly faster than that in isopropanol since chloroform is smaller, more spherical, and lacks restriction by hydrogen bonding interactions. Previous deuteron scattering studies reported that the rotational correlation times for deuterated isopropanol and $CDCl_3$ differed by a factor of 6,[394] which is relatively consistent with the slowest time coefficients obtained from the DAFs. Isopropanol displays two longer lifetimes of ~32 ps and ~92 ps that we tentatively attribute to rotational motions within a hydrogen bonded network. These assignments are consistent with experimental rotational correlation times of 22 ps and 91 ps that were measured by NMR[394, 395] and dielectric spectroscopies,[395, 396] respectively. Meanwhile, we conjecture that the shortest lifetime (~0.4 ps) is dominantly due to fast intramolecular motions such as angle bending or dihedral rotations.

Table 6.6. Fitted parameters to the computed molecular dipole autocorrelation functions for TriMOS and TriPS in chloroform and isopropanol solutions.

chloroform				isopropanol			
TriMOS		TriPS		TriMOS		TriPS	
A	τ (ps)	A	τ (ps)	A	τ (ps)	A	τ (ps)
0.80	5.85	0.78	5.89	0.36	99.41	0.48	86.26
0.12	1.76	0.13	2.18	0.38	35.70	0.28	27.42
0.09	0.46	0.24	0.51	0.11	4.09	0.11	3.04
-	-	-	-	0.12	0.34	0.12	0.27

Isopropanol also contains a time coefficient that is comparable to the hydrogen bond lifetime. A similar value has been reported in the rotational correlation times measured by dielectric spectroscopy.[397] The largest DAF lifetime in isopropanol is on the order of 100 ps, indicating that there is not a significant rotation of the dipole when isopropanol exchanges hydrogen bonds. This is most likely due to the size of isopropanol. The lifetime that is on the same order as the hydrogen bond lifetime only accounts for about 10 % of the change in dipole. Furthermore, the large amount of time it takes for isopropanol to rotate suggests that it is hindered by hydrogen bonding interactions. Isopropanol maintains its orientation for a long time by exchanging hydrogen bonds with a close neighbor.

6.4. Conclusions

Proper interpretation of static and time-resolved vibrational spectroscopic data requires an understanding of the ways in which homogeneous and inhomogeneous effects are manifested in spectral change. In this study, TriMOS and TriPS provided an opportunity to monitor the same probe, the Si-H vibrational mode, with two different ligand sets and

three solvent systems by steady-state FTIR and time-resolved 2D-IR spectroscopies. DFT calculations provided insight into the differences in silicon hydride sensitivity to solvent through increased mode polarization with more electron withdrawing ligands. Calculations and simulations revealed that the solvatochromic trends of the hydride mode arise from specific hydrogen and halogen bonding interactions with the solute. Spectral diffusion experienced by $\nu_{Si\text{-}H}$ was found to be characteristic of the solvent type rather than the solute structure, yet showed the same sensitivity observed in the FTIR solvatochromic shifts. Therefore, the solvent motions are dominated by their interactions with neighboring solvent molecules rather than with the solute. MD simulations confirmed that the dynamics experienced in isopropanol were due to hydrogen bonding fluctuations in the surrounding solvation shell. This was further corroborated by the calculation of the dipole autocorrelation function of individual solvent molecules throughout the bulk. These results showed the principle motions experienced by isopropanol molecules, which included a lifetime of similar magnitude to the hydrogen bonding lifetime. The remaining motions include rotational diffusion, and low frequency intramolecular motions.

Bibliography

1. Cohen, A. J.; Mori-Sanchez, P.; Yang, W. T., Challenges for Density Functional Theory. *Chem. Rev.* **2012,** *112* (1), 289-320.

2. Levine, B. G.; Ko, C.; Quenneville, J.; Martinez, T. J., Conical intersections and double excitations in time-dependent density functional theory. *Mol. Phys.* **2006,** *104* (5-7), 1039-1051.

3. Yang, Y.; Shen, L.; Zhang, D.; Yang, W. T., Conical Intersections from Particle-Particle Random Phase and Tamm-Dancoff Approximations. *J. Phys. Chem. Lett.* **2016,** *7* (13), 2407-2411.

4. Herbert, J. M.; Zhang, X.; Morrison, A. F.; Liu, J., Beyond Time-Dependent Density Functional Theory Using Only Single Excitations: Methods for Computational Studies of Excited States in Complex Systems. *Acc. Chem. Res.* **2016,** *49* (5), 931-941.

5. Huix-Rotllant, M.; Nikiforov, A.; Thiel, W.; Filatov, M., Description of Conical Intersections with Density Functional Methods. *Top Curr Chem* **2016,** *368*, 445-476.

6. Silva, M. R.; Schreiber, M.; Sauer, S. P. A.; Thiel, W., Benchmarks for electronically excited states: Time-dependent density functional theory and density functional theory based multireference configuration interaction. *J. Chem. Phys.* **2008,** *129* (10), 104103.

7. Domcke, W.; Yarkony, D. R., Role of Conical Intersections in Molecular Spectroscopy and Photoinduced Chemical Dynamics. *Annu. Rev. Phys. Chem.* **2012,** *63*, 325-352.

8. Robb, M. A., Conical intersections : theory, computation and experiment. In *Advanced series in physical chemistry*, Domcke, W.; Yarkony, D.; Köppel, H., Eds. World Scientific: Singapore ; Hackensack, NJ, 2011; pp 3-50.

9. Lischka, H.; Dallos, M.; Szalay, P. G.; Yarkony, D. R.; Shepard, R., Analytic evaluation of nonadiabatic coupling terms at the MR-CI level. I. Formalism. *J. Chem. Phys.* **2004,** *120* (16), 7322-7329.

10. Buenker, R. J.; Peyerimhoff, S. D.; Butscher, W., Applicability of Multi-Reference Double-Excitation Ci (Mrd-Ci) Method to Calculation of Electronic Wavefunctions and Comparison with Related Techniques. *Mol Phys* **1978,** *35* (3), 771-791.

11. Werner, H.-J.; Reinsch, E.-A., The self-consistent electron pairs method for multiconfiguration reference state functions. *J. Chem. Phys.* **1982,** *76*, 3144-3146.

12. Shao, Y. H.; Head-Gordon, M.; Krylov, A. I., The spin-flip approach within time-dependent density functional theory: Theory and applications to diradicals. *J. Chem. Phys.* **2003,** *118* (11), 4807-4818.

13. Minezawa, N.; Gordon, M. S., Optimizing Conical Intersections by Spin-Flip Density Functional Theory: Application to Ethylene. *J. Phys. Chem. A* **2009,** *113* (46), 12749-12753.

14. Li, S. H. L.; Marenich, A. V.; Xu, X. F.; Truhlar, D. G., Configuration Interaction-Corrected Tamm-Dancoff Approximation: A Time-Dependent Density Functional Method with the Correct Dimensionality of Conical Intersections. *J. Phys. Chem. Lett.* **2014,** *5* (2), 322-328.

15. Lieb, E. H., Density Functionals for Coulomb-Systems. *Int. J. Quantum Chem.* **1983,** *24* (3), 243-277.

16. Gross, E. K. U.; Oliveira, L. N.; Kohn, W., Rayleigh-Ritz Variational Principle for Ensembles of Fractionally Occupied States. *Phys. Rev. A* **1988,** *37* (8), 2805-2808.

17. Filatov, M., Assessment of Density Functional Methods for Obtaining Geometries at Conical Intersections in Organic Molecules. *J. Chem. Theory Comput.* **2013,** *9* (10), 4526-4541.

18. Kaduk, B.; Van Voorhis, T., Communication: Conical intersections using constrained density functional theory-configuration interaction. *J. Chem. Phys.* **2010,** *133* (6), 061102.

19. Cembran, A.; Song, L.; Mo, Y.; Gao, J., Block-localized density functional theory (BLDFT), diabatic coupling, and its use in valence bond theory for representing reactive potential energy surfaces. *J. Chem. Theory Comput.* **2009,** *5*, 2702-2716..

20. Liu, W. J.; Hoffmann, M. R., iCI: Iterative CI toward Full CI. *J. Chem. Theory Comput.* **2016,** *12* (6), 1169-1178.

21. Liu, W. J.; Hoffmann, M. R., SDS: the 'static-dynamic-static' framework for strongly correlated electrons. *Theor. Chem. Acc.* **2014,** *133* (5), 1481.

22. Liu, W. J., Ideas of relativistic quantum chemistry. *Mol. Phys.* **2010,** *108* (13), 1679-1706.

23. King, H. F.; Staton, R. E.; Kim, H.; Wyatt, R. E.; Parr, R. G., Corresponding orbitals and the nonorthogonality problems in molecular quantum mechanics. *J. Chem. Phys.* **1967,** *47*, 1936.

24. Mo, Y.; Gao, J., Ab initio QM/MM simulations with a molecular orbital-valence bond (MOVB) method: application to an SN2 reaction in water. *J. Comput. Chem.* **2000,** *21* (16), 1458-1469.

25. Mo, Y.; Gao, J., An Ab Initio Molecular Orbital-Valence Bond (MOVB) Method for Simulating Chemical Reactions in Solution. *J. Phys. Chem. A* **2000,** *104* (13), 3012-3020.

26. Ren, H. S.; Provorse, M. R.; Bao, P.; Qu, Z. X.; Gao, J. L., Multistate Density Functional Theory for Effective Diabatic Electronic Coupling. *J. Phys. Chem. Lett.* **2016,** *7* (12), 2286-2293.

27. Chirgwin, H. B.; Coulson, C. A., *Proc. R. Soc. London Ser. A* **1950,** *2*, 196.

28. Schipper, P. R. T.; Gritsenko, O. V.; Baerends, E. J., Benchmark calculations of chemical reactions in density functional theory: Comparison of the accurate Kohn-Sham solution with generalized gradient approximations for the H-2+H and H-2+H-2 reactions. *J. Chem. Phys.* **1999,** *111* (9), 4056-4067.

29. Mermin, N. D., Thermal Properties of the Inhomogeneous Electron Gas. *Phys. Rev.* **1965,** *137*, . A1441–A1443.

30. Schipper, P. R. T.; Gritsenko, O. V.; Baerends, E. J., One-determinantal pure state versus ensemble Kohn-Sham solutions in the case of strong electron correlation: CH2 and C-2. *Theor. Chem. Acc.* **1998,** *99* (5), 329-343.

31. Chai, J. D., Thermally-assisted-occupation density functional theory with generalized-gradient approximations. *J. Chem. Phys.* **2014,** *140* (18), 18a521.

32. Chai, J. D., Density functional theory with fractional orbital occupations. *J. Chem. Phys.* **2012,** *136* (15), 154104.

33. Miehlich, B.; Stoll, H.; Savin, A., A correlation-energy density functional for multideterminantal wavefunctions. *Mol. Phys.* **1997,** *91* (3), 527-536.

34. Cooper, D. L.; Gerratt, J.; Raimondi, M., Applications of spin-coupled valence bond theory. *Chem. Rev.* **1991,** *91* (5), 929-64.

35. Gerratt, J.; Cooper, D. L.; Karadakov, P. B.; Raimondi, M., Modern valence bond theory. *Chem. Soc. Rev.* **1997,** *26* (2), 87-100.

36. Song, L.; Gao, J., On the Construction of Diabatic and Adiabatic Potential Energy Surfaces Based on Ab Initio Valence Bond Theory. *J. Phys. Chem. A* **2008,** *112* (50), 12925-12935.

37. Ayers, P. W.; Yang, W. T., Legendre-transform functionals for spin-density-functional theory. *J. Chem. Phys.* **2006,** *124* (22), 224108.

38. Paterson, M. J.; Bearpark, M. J.; Robb, M. A.; Blancafort, L.; Worth, G. A., Conical intersections: A perspective on the computation of spectroscopic Jahn-Teller parameters and the degenerate 'intersection space'. *Phys Chem Chem Phys* **2005,** *7* (10), 2100-2115.

39. Meisner, J.; Vacher, M.; Bearpark, M. J.; Robb, M. A., Geometric Rotation of the Nuclear Gradient at a Conical Intersection: Extension to Complex Rotation of Diabatic States. *J. Chem. Theory Comput.* **2015,** *11* (7), 3115-3122.

40. Vacher, M.; Mendive-Tapia, D.; Bearpark, M. J.; Robb, M. A., Electron dynamics upon ionization: Control of the timescale through chemical substitution and effect of nuclear motion. *J. Chem. Phys.* **2015,** *142* (9), 094105.

41. Vacher, M.; Meisner, J.; Mendive-Tapia, D.; Bearpark, M. J.; Robb, M. A., Electronic Control of Initial Nuclear Dynamics Adjacent to a Conical Intersection. *J. Phys. Chem. A* **2015,** *119* (21), 5165-5172.

42. Li, Z. H.; Valero, R.; Truhlar, D. G., Improved direct diabatization and coupled potential energy surfaces for the photodissociation of ammonia. *Theor. Chem. Acc.* **2007,** *118* (1), 9-24.

43. Xie, C. J.; Ma, J. Y.; Zhu, X. L.; Zhang, D. H.; Yarkony, D. R.; Xie, D. Q.; Guo, H., Full-Dimensional Quantum State-to-State Nonadiabatic Dynamics for Photodissociation of Ammonia in its A-Band. *J. Phys. Chem. Lett.* **2014,** *5* (7), 1055-1060.

44. Numrich, R. W.; Truhlar, D. G., Mixing of ionic and covalent configurations for sodium hydride, potassium hydride, and hydromagnesium(1+). Potential energy curves and couplings between molecular states. *J. Phys. Chem.* **1975,** *79* (25), 2745-66.

45. Yarkony, D. R., Diabolical conical intersections. *Rev. Mod. Phys.* **1996,** *68* (4), 985-1013.

46. Nakamura, H.; Truhlar, D. G., The direct calculation of diabatic states based on configurational uniformity. *J. Chem. Phys.* **2001,** *115* (22), 10353-10372.

47. Japser, A. W.; Kendrick, C. A.; Mead, C. A.; Truhlar, D. G., In *Modern Trends in Chemical Reaction Dynamics: Eperiment and Theory (Part I)*, Yang, X.; Liu, K., Eds. World Scientific: Singapore, 2004; pp 329–391.

48. Koppel, H., Diabatic representation: methods for the constrution of diabatic electronic states. In *Conical Intersections: Electronic Structure, Dynamics and Spectroscopy*, Domcke, W.; Yarkony, D. R.; Koppel, H., Eds. World Scientific Publishing Co.: Hackensack, NJ, 2004; pp 175-204.

49. Zhu, X. L.; Yarkony, D. R., Toward eliminating the electronic structure bottleneck in nonadiabatic dynamics on the fly: An algorithm to fit nonlocal,

quasidiabatic, coupled electronic state Hamiltonians based on ab initio electronic structure data. *J. Chem. Phys.* **2010,** *132* (10), 104101.

50. Li, S. H. L.; Truhlar, D. G.; Schmidt, M. W.; Gordon, M. S., Model space diabatization for quantum photochemistry. *J. Chem. Phys.* **2015,** *142* (6), 064106.

51. Halvick, P.; Truhlar, D. G., A new diabatic representation of the coupled potential energy surfaces for sodium(3p 2P) + molecular hydrogen .fwdarw. sodium(3s 2S) + molecular hydrogen or sodium hydride + atomic hydrogen. *J. Chem. Phys.* **1992,** *96* (4), 2895-2909.

52. Jasper, A. W.; Zhu, C. Y.; Nangia, S.; Truhlar, D. G., Introductory lecture: Nonadiabatic effects in chemical dynamics. *Faraday Discussions* **2004,** *127*, 1-22.

53. Gao, J.; Grofe, A.; Ren, H.; Bao, P., Beyond Kohn-Sham approximation: Hybrid multistate wave function and density functional theory. *J. Phys. Chem. Lett.* **2016,** *7*, 5143−5149, DOI:10.1021/acs.jpclett.6b02455.

54. Nakamura, H.; Truhlar, D. G., Direct diabatization of electronic states by the fourfold way. II. Dynamical correlation and rearrangement processes. *J. Chem. Phys.* **2002,** *117* (12), 5576-5593.

55. Baer, M., *Beyond Born-Oppenheimer: Electronic Nonadiabatic Coupling Terms and Conical Intersections*. Wiley: New York, 2006.

56. Mead, C. A.; Truhlar, D. G., Conditions for the definition of a strictly diabatic electronic basis for molecular systems. *J. Chem. Phys.* **1982,** *77* (12), 6090-8.

57. Boutalib, A.; Gadea, F. X., Abinitio Adiabatic and Diabatic Potential-Energy Curves of the Lih Molecule. *J. Chem. Phys.* **1992,** *97* (2), 1144-1156.

58. Berriche, H.; Gadea, F. X., Ab-Initio Adiabatic and Diabatic Permanent Dipoles for the Low-Lying States of the Lih Molecule - a Direct Illustration of the Ionic Character. *Chem. Phys. Lett.* **1995,** *247* (1-2), 85-88.

59. Zhang, P.; Morokuma, K.; Wodtke, A. M., High-level ab initio studies of unimolecular dissociation of the ground-state N-3 radical. *J. Chem. Phys.* **2005,** *122* (1), 014106.

60. Viel, A.; Eisfeld, W.; Evenhuis, C. R.; Manthe, U., Photoionization-induced dynamics of the ammonia cation studied by wave packet calculations using curvilinear coordinates. *Chem. Phys.* **2008,** *347* (1-3), 331-339.

61. Mota, V. C.; Varandas, A. J. C., HN2((2)A ') electronic manifold. II. Ab initio based double-sheeted DMBE potential energy surface via a global diabatization angle. *J. Phys. Chem. A* **2008,** *112* (16), 3768-3786.

62. Subotnik, J. E.; Yeganeh, S.; Cave, R. J.; Ratner, M. A., Constructing diabatic states from adiabatic states: Extending generalized Mulliken-Hush to multiple charge centers with Boys localization. *J. Chem. Phys.* **2008,** *129* (24), 244101.

63. Zhang, A. J.; Zhang, P. Y.; Chu, T. S.; Han, K. L.; He, G. Z., Quantum dynamical study of the electronic nonadiabaticity in the D+DBr ✹ Br(Br*)+D2 reaction on new diabatic potential energy surfaces. *J. Chem. Phys.* **2012,** *137* (19), 194305.

64. Domcke, W.; Woywod, C., Direct Construction of Diabatic States in the Casscf Approach - Application to the Conical Intersection of the (1)a(2) and B-1(1) Excited-States of Ozone. *Chem. Phys. Lett.* **1993,** *216* (3-6), 362-368.

65. Godsi, O.; Evenhuis, C. R.; Collins, M. A., Interpolation of multidimensional diabatic potential energy matrices. *J. Chem. Phys.* **2006,** *125* (10), 104105.

66. Ou, Q.; Bellchambers, G. D.; Furche, F.; Subotnik, J. E., First-order derivative couplings between excited states from adiabatic TDDFT response theory. *J. Chem. Phys.* **2015,** *142* (6).

67. Zhu, X. L.; Malbon, C. L.; Yarkony, D. R., An improved quasi-diabatic representation of the 1, 2, 3(1)A coupled adiabatic potential energy surfaces of phenol in the full 33 internal coordinates. *J. Chem. Phys.* **2016,** *144* (12), 124312.

68. Zhu, X. L.; Yarkony, D. R., Constructing diabatic representations using adiabatic and approximate diabatic data - Coping with diabolical singularities. *J. Chem. Phys.* **2016,** *144* (4), 044104.

69. Atchity, G. J.; Ruedenberg, K., Determination of diabatic states through enforcement of configurational uniformity. *Theor. Chem. Acc.* **1997,** *97* (1-4), 47-58.

70. Nakamura, H.; Truhlar, D. G., Extension of the fourfold way for calculation of global diabatic potential energy surfaces of complex, multiarrangement, non-Born-Oppenheimer systems: Application to HNCO(S-0,S-1). *J. Chem. Phys.* **2003,** *118* (15), 6816-6829.

71. Subotnik, J. E.; Vura-Weis, J.; Sodt, A. J.; Ratner, M. A., Predicting Accurate Electronic Excitation Transfer Rates via Marcus Theory with Boys or Edmiston-Ruedenberg Localized Diabatization. *J. Phys. Chem. A* **2010,** *114* (33), 8665-8675.

72. Alguire, E.; Subotnik, J. E., Diabatic couplings for charge recombination via Boys localization and spin-flip configuration interaction singles. *J. Chem. Phys.* **2011,** *135* (4), 044114.

73. Simah, D.; Hartke, B.; Werner, H. J., Photodissociation dynamics of H2S on new coupled ab initio potential energy surfaces. *J. Chem. Phys.* **1999,** *111* (10), 4523-4534.

74. Fulscher, M. P.; Serrano-Andres, L., Quasi diabatic CASSCF state functions. *Mol. Phys.* **2002,** *100* (6), 903-909.

75. Hoyer, C. E.; Parker, K.; Gagliardi, L.; Truhlar, D. G., The DQ and DQ Phi electronic structure diabatization methods: Validation for general applications. *J. Chem. Phys.* **2016,** *144* (19), 194101.

76. Hoyer, C. E.; Xu, X. F.; Ma, D. X.; Gagliardi, L.; Truhlar, D. G., Diabatization based on the dipole and quadrupole: The DQ method. *J. Chem. Phys.* **2014,** *141* (11), 114104.

77. Siegbahn, P.; Heiberg, A.; Roos, B.; Levy, B., Comparison of the Super-Cl and the Newton-Raphson Scheme in the Complete Active Space Scf Method. *Phys. Scr.* **1980,** *21* (3-4), 323-327.

78. Finley, J.; Malmqvist, P. A.; Roos, B. O.; Serrano-Andres, L., The multi-state CASPT2 method. *Chem. Phys. Lett.* **1998,** *288* (2-4), 299-306.

79. Werner, H. J.; Knowles, P. J., A 2nd Order Multiconfiguration SCF Procedure with Optimum Convergence. *J. Chem. Phys.* **1985,** *82* (11), 5053-5063.

80. Nakano, H.; Hirao, K.; Gordon, M. S., Analytic energy gradients for multiconfigurational self-consistent field second-order quasidegenerate perturbation theory (MC-QDPT). *J. Chem. Phys.* **1998,** *108*, 5660.

81. Venghaus, F.; Eisfeld, W., Block-diagonalization as a tool for the robust diabatization of high-dimensional potential energy surfaces. *J. Chem. Phys.* **2016,** *144*, 114110.

82. Wittenbrink, N.; Venghaus, F.; Williams, D.; Eisfeld, W., A new approach for the development of diabatic potential energy surfaces: Hybrid block-diagonalization and diabatization by ansatz. *J. Chem. Phys.* **2016,** *145*, 184108.

83. Tamura, H., Diabatization for Time-Dependent Density Functional Theory: Exciton Transfers and Related Conical Intersections. *J. Phys. Chem. A* **2016,** *ASAP*.

84. Mo, Y. R.; Wu, W.; Zhang, Q. N., Valence-Bond Description for the Ground-State and Several Low-Lying Excited-States of Lih. *Theochem-J. Mol. Struct.* **1993,** *102*, 237-249.

85. Cembran, A.; Payaka, A.; Lin, Y. L.; Xie, W. S.; Mo, Y. R.; Song, L. C.; Gao, J. L., A Non-Orthogonal Block-Localized Effective Hamiltonian Approach for Chemical and Enzymatic Reactions. *J. Chem. Theory Comput.* **2010,** *6* (7), 2242-2251.

86. Valero, R.; Song, L.; Gao, J.; Truhlar, D. G., Perspective on Diabatic Models of Chemical Reactivity as Illustrated by the Gas-Phase SN2 Reaction of Acetate Ion with 1,2-Dichloroethane. *J. Chem. Theory Comput.* **2009,** *5* (1), 1-22 [Erratum, June 10, 2009].

87. Van Voorhis, T.; Kowalczyk, T.; Kaduk, B.; Wang, L. P.; Cheng, C. L.; Wu, Q., The Diabatic Picture of Electron Transfer, Reaction Barriers, and Molecular Dynamics. *Annu. Rev. Phys. Chem.* **2010,** *61*, 149-170.

88. Mo, Y.; Peyerimhoff, S. D., Theoretical analysis of electronic delocalization. *J. Chem. Phys.* **1998,** *109* (5), 1687-1697.

89. Mo, Y.; Zhang, Y.; Gao, J., A Simple Electrostatic Model for Trisilylamine: Theoretical Examinations of the n.fwdarw..sigma. Negative Hyperconjugation, p.pi..fwdarw.d.pi. Bonding, and Stereoelectronic Interaction. *J. Am. Chem. Soc.* **1999,** *121*, 5737-42.

90. Mo, Y.; Gao, J.; Peyerimhoff, S. D., Energy decomposition analysis of intermolecular interactions using a block-localized wave function approach. *J. Chem. Phys.* **2000,** *112* (13), 5530-5538.

91. Cembran, A.; Provorse, M. R.; Wang, C. W.; Wu, W.; Gao, J. L., The Third Dimension of a More O'Ferrall-Jencks Diagram for Hydrogen Atom Transfer in the Isoelectronic Hydrogen Exchange Reactions of (PhX)(2)H-center dot with X = O, NH, and CH2. *J. Chem. Theory Comput.* **2012,** *8* (11), 4347-4358.

92. Mo, Y. R.; Bao, P.; Gao, J. L., Energy decomposition analysis based on a block-localized wavefunction and multistate density functional theory. *Phys Chem Chem Phys* **2011,** *13* (15), 6760-6775.

93. Mavros, M. G.; Voorhis, T. V., Communication: CDFT-CI couplings can be unreliable when there is fractional charge transfer. *J. Chem. Phys.* **2015,** *143* (23), 231102.

94. Gim, Y.; Lee, C. W., Studies of singlet Rydberg series of LiH derived from Li(nl) + H(1s), with n <= 6 and l <= 4. *J. Chem. Phys.* **2014,** *141* (14), 144313.

95. Gadea, F. X.; Boutalib, A., Computation and Assignment of Radial Couplings Using Accurate Diabatic Data for the Lih Molecule. *J. Phys. B-* **1993,** *26* (1), 61-74.

96. Gadea, F. X.; Leininger, T., Accurate ab initio calculations for LiH and its ions, LiH+ and LiH-. *Theor. Chem. Acc.* **2006,** *116* (4-5), 566-575.

97. Bande, A.; Nakashima, H.; Nakatsuji, H., LiH potential energy curves for ground and excited states with the free complement local Schrodinger equation method. *Chem. Phys. Lett.* **2010,** *496* (4-6), 347-350.

98. Lamoudi, N.; Bouledroua, M.; Alioua, K.; Allouche, A. R.; Aubert-Frecon, M., Theoretical investigation of the lithium 2p <- 2s photoabsorption spectra perturbed by atomic hydrogen. *Phys. Rev. A* **2013,** *87* (5), 052713.

99. Habli, H.; Mejrissi, L.; Ghalla, H.; Yaghmour, S. J.; Oujia, B.; Gadea, F. X., Ab initio investigation of the electronic and vibrational properties for the (CaLi)(+) ionic molecule. *Molecular Physics* **2016,** *114* (10), 1568-1582.

100. Stwalley, W. C.; Zemke, W. T., Spectroscopy and Structure of the Lithium Hydride Diatomic-Molecules and Ions. *J. Phys. Chem. Ref. Data* **1993,** *22* (1), 87-112.

101. Truhlar, D. G.; Mullaney, N. A., Semi-Classical Exchange Approximation for Inelastic Electron-Scattering. *J. Chem. Phys.* **1978,** *68* (4), 1574-1584.

102. Li, M. G.; Carlson, R. K.; Luo, S. J.; Ma, D. X.; Olsen, J.; Truhlar, D. G.; Gagliardi, L., Multiconfiguration Pair-Density Functional Theory. *J. Chem. Theory Comput.* **2014,** *10* (9), 3669-3680.

103. Dunning, T. H., Jr., Gaussian basis sets for use in correlated molecular calculations. I. The atoms boron through neon and hydrogen. *J. Chem. Phys.* **1989,** *90* (2), 1007-23.

104. Dunning, T. H.; Hay, P. J., In *Methods of Electronic Structure Theory*, Schaefer III, H. F., Ed. Plenum Press: 1977; Vol. 3, pp pp. 1-28.

105. Moore, C. E., *Atomic Energy Levels, Nat. Bur. Stand., Circ. No. 467*. U.S. GPO: Washington, D. C., 1971.

106. Perdew, J. P.; Burke, K.; Ernzerhof, M., Generalized gradient approximation made simple. *Phys. Rev. Lett.* **1996,** *77* (18), 3865-3868.

107. Adamo, C.; Barone, V., Toward reliable density functional methods without adjustable parameters: The PBE0 model. *J. Chem. Phys.* **1999,** *110* (13), 6158-6170.

108. Chan, W.-L.; Berkelbach, T. C.; Provorse, M. R.; Monahan, N. R.; Tritsch, J. R.; Hybertsen, M. S.; Reichman, D. R.; Gao, J.; Zhu, X.-Y., The quantum coherent mechanism for singlet fission: Experiment and theory. *Acc. Chem. Res.* **2012**, submitted (for a special issue on singlet fission).

109. Werner, H. J.; Knowles, J. R.; Knizia, G.; Manby, F. R.; Schutz, M.; al., e. *MOLPRO – version 2012.1*, http://www.molpro.net, 2012.

110. Schmidt, M. W.; Baldridge, K. K.; Boatz, J. A.; Elbert, S. T.; Gordon, M. S.; Jensen, J. H.; Koseki, S.; Matsunaga, N.; Nguyen, K. A.; Su, S. J.; Windus, T. L.; Dupuis, M.; Montgomery, J. S., General atomic and molecular electronic structure system. *J. Comput. Chem.* **1993,** *14* (11), 1347-63.

111. Huang, Y. L.; Luh, W. T.; Jeung, G. H.; Gadea, F. X., The D (1)Sigma(+) state of (LiH)-Li-7. *J. Chem. Phys.* **2000,** *113* (2), 683-689.

112. Numrich, R. W.; Truhlar, D. G., Mixing of Ionic and Covalent Configurations for Nah, Kh, and Mgh+ - Potential-Energy Curves and Couplings between Molecular States. *J. Phys. Chem.* **1975,** *79* (25), 2745-2766.

113. Habli, H.; Ghalla, H.; Oujia, B.; Gadea, F. X., Ab initio study of spectroscopic properties of the calcium hydride molecular ion. *Eur. Phys. J. D* **2011,** *64* (1), 5-19.

114. Becke, A. D., Perspective: Fifty years of density-functional theory in chemical physics. *Journal of Chemical Physics* **2014,** *140* (18), 18a301.

115. Hohenberg, P.; Kohn, W., Inhomogeneous electron gas. *Phys. Rev.* **1964,** *136*, B864.

116. Kohn, W.; Sham, L. J., Self-consistent equations including exchange and correlation effects. *Phys. Rev.* **1965,** *140*, A1133.

117. Cohen, A. J.; Mori-Sanchez, P.; Yang, W., Insights into Current Limitations of Density Functional Theory. *Science* **2008,** *321* (5890), 792-794.

118. Becke, A. D.; Savin, A.; Stoll, H., Extension of the Local-Spin-Density Exchange-Correlation Approximation to Multiplet States. *Theor. Chim. Acta* **1995,** *91* (3-4), 147-156.

119. von Barth, U.; Hedin, L., A local exchange-correlation potential or the spin polarized case: I. *J. Phys. C; Solid State Phys.* **1972,** *5*, 1629-1642.

120. Noodleman, L., Valence Bond Description of Anti-Ferromagnetic Coupling in Transition-Metal Dimers. *J. Chem. Phys.* **1981,** *74* (10), 5737-5743.

121. Luo, S. J.; Averkiev, B.; Yang, K. R.; Xu, X. F.; Truhlar, D. G., Density Functional Theory of Open-Shell Systems. The 3d-Series Transition-Metal Atoms and Their Cations. *J. Chem. Theory Comput.* **2014,** *10* (1), 102-121.

122. Li, Z. D.; Liu, W. J., Spin-adapted open-shell random phase approximation and time-dependent density functional theory. I. Theory. *J. Chem. Phys.* **2010,** *133* (6), 064106.

123. Li, Z. D.; Liu, W. J.; Zhang, Y.; Suo, B. B., Spin-adapted open-shell time-dependent density functional theory. II. Theory and pilot application. *Journal of Chemical Physics* **2011,** *134* (13), 134101.

124. Li, Z.; Liu, W., Spin-adapted open-shell time-dependent density functional theory: III. An even better and simpler formulation. *J. Chem. Phys.* **2011,** *135*, 194106.

125. Li, Z. D.; Liu, W. J., Critical Assessment of Time-Dependent Density Functional Theory for Excited States of Open-Shell Systems: II. Doublet-Quartet Transitions. *J. Chem. Theory Comput.* **2016,** *12* (6), 2517-2527.

126. Li, Z. D.; Liu, W. J., Critical Assessment of TD-DFT for Excited States of Open-Shell Systems: I. Doublet-Doublet Transitions. *J. Chem. Theory Comput.* **2016,** *12* (1), 238-260.

127. Gao, J.; Grofe, A.; Ren, H.; Bao, P., Beyond Kohn-Sham approximation: Hybrid multistate wave function and density functional theory. *J. Phys. Chem. Lett.* **2016,** *7*, 5143−5149.

128. Nagy, A., Exact Ensemble Exchange Potentials for Multiplets. *International Journal of Quantum Chemistry* **1995**, 297-301.

129. Filatov, M.; Shaik, S., Spin-restricted density functional approach to the open-shell problem. *Chem. Phys. Lett.* **1998,** *288* (5-6), 689-697.

130. Grimme, S.; Waletzke, M., A combination of Kohn-Sham density functional theory and multi-reference configuration interaction methods. *J. Chem. Phys.* **1999,** *111* (13), 5645-5655.

131. Huix-Rotllant, M.; Nikiforov, A.; Thiel, W.; Filatov, M., Description of Conical Intersections with Density Functional Methods. *Top Curr Chem: Density-Functional Methods for Excited States* **2016,** *368*, 445-476.

132. Grafenstein, J.; Cremer, D., Development of a CAS-DFT method covering non-dynamical and dynamical electron correlation in a balanced way. *Molecular Physics* **2005,** *103* (2-3), 279-308.

133. Kurzweil, Y.; Lawler, K. V.; Head-Gordon, M., Analysis of multi-configuration density functional theory methods: theory and model application to bond-breaking. *Mol. Phys.* **2009,** *107* (20), 2103-2110.

134. Bao, J. L.; Sand, A.; Gagliardi, L.; Truhlar, D. G., Correlated-Participating-Orbitals Pair-Density Functional Method and Application to Multiplet Energy Splittings of Main-Group Divalent Radicals. *J. Chem. Theory Comput.* **2016,** *12* (9), 4274-4283.

135. Krylov, A. I., Spin-flip configuration interaction: an electronic structure model that is both variational and size-consistent. *Chemical Physics Letters* **2001,** *350* (5-6), 522-530.

136. Li, Z. D.; Liu, W. J., Theoretical and numerical assessments of spin-flip time-dependent density functional theory. *Journal of Chemical Physics* **2012,** *136* (2), 024107.

137. Bernard, Y. A.; Shao, Y. H.; Krylov, A. I., General formulation of spin-flip time-dependent density functional theory using non-collinear kernels: Theory, implementation, and benchmarks. *J. Chem. Phys.* **2012,** *136* (20), 204103.

138. Staroverov, V. N.; Davidson, E. R., A density functional method for degenerate spin-multiplet components. *Chemical Physics Letters* **2001,** *340* (1-2), 142-150.

139. Filatov, M., Ensemble DFT Approach to Excited States of Strongly Correlated Molecular Systems. *Top Curr Chem* **2016,** *368*, 97-124.

140. Grofe, A.; Qu, Z.; Truhlar, D. G.; Li, H.; Gao, J., Diabatic-At-Construction Method for Diabatic and Adiabatic Ground and Excited States Based on Multistate Density Functional Theory. *J Chem Theory Comput* **2017,** *13* (3), 1176-1187.

141. Chan, W.-L.; Berkelbach, T. C.; Provorse, M. R.; Monahan, N. R.; Tritsch, J. R.; Hybertsen, M. S.; Reichman, D. R.; Gao, J.; Zhu, X.-Y., The quantum coherent mechanism for singlet fission: Experiment and theory. *Acc. Chem. Res.* **2013,** *46*, 1321–1329.

142. Ziegler, T.; Rauk, A.; Baerends, E. J., Calculation of Multiplet Energies by Hartree-Fock-Slater Method. *Theoretica Chimica Acta* **1977,** *43* (3), 261-271.

143. Mineva, T.; Goursot, A.; Daul, C., Atomic multiplet energies from density functional calculations. *Chemical Physics Letters* **2001,** *350* (1-2), 147-154.

144. Slater, J. C., *Quantum Theory of Atomic Structure*. McGraw-Hill Book Co., Inc., New York: 1960; Vol. I.

145. Slipchenko, L. V.; Krylov, A. I., Singlet-triplet gaps in diradicals by the spin-flip approach: A benchmark study. *Journal of Chemical Physics* **2002,** *117* (10), 4694-4708.

146. Casanova, D.; Slipchenko, L. V.; Krylov, A. I.; Head-Gordon, M., Double spin-flip approach within equation-of-motion coupled cluster and configuration interaction formalisms: Theory, implementation, and examples. *Journal of Chemical Physics* **2009,** *130* (4), 044103.

147. Schmidt, M. W.; Baldridge, K. K.; Boatz, J. A.; Elbert, S. T.; Gordon, M. S.; Jensen, J. H.; Koseki, S.; Matsunaga, N.; Nguyen, K. A.; Su, S. J.; Windus, T. L.; Dupuis, M.; Montgomery, J. S. *GAMESS*, 11; 1993.

148. Sherrill, C. D.; Leininger, M. L.; van Huis, T. J.; Schaefer III, H. F., Structures and vibrational frequencies in the full configuration interaction limit: Predictions for four electronic states of methylene using a triple-zeta plus double polarization (TZ2P) basis. *J. Chem. Phys.* **1998,** *108*, 1040.

149. Yamaguchi, Y.; Van Huis, T. J.; Sherrill, C. D.; Schaefer III, H. F., The X˜1A1, a˜3B1, a˜1B˜1, and B˜1A1 electronic states of SiH2. *Theoret. Chem. Acc.* **1998,** *97* (1-4), 341-349.

150. Stephens, J. C.; Yamaguchi, Y.; Sherrill, C. D.; Schaefer III, H. F., X̃ 3B1, ã 1A1, b̃ 1B1, and c̃ 1 Electronic States of NH2+. *J. Phys. Chem.* **1998,** *102* (22), 3999-4006.

151. Van Huis, T. J.; Yamaguchi, Y.; Sherrill, C. D.; Schaefer III, H. F., X̃ 1A1, ã 3B1, Ã 1B1, and B̃ 1A1 Electronic States of PH2+. *J. Phys. Chem. A,* **1997,** *101*, 6955–6963.

152. Skinner, J. L.; Pieniazek, P. A.; Gruenbaum, S. M., Vibrational Spectroscopy of Water at Interfaces. *Acc. Chem. Res.* **2012,** *45* (1), 93-100.

153. Fried, S. D.; Boxer, S. G., Measuring Electric Fields and Noncovalent Interactions Using the Vibrational Stark Effect. *Acc. Chem. Res.* **2015,** *48* (4), 998-1006.

154. Fried, S. D.; Bagchi, S.; Boxer, S. G., Extreme electric fields power catalysis in the active site of ketosteroid isomerase. *Science* **2014,** *346* (6216), 1510-1514.

155. Kim, H.; Cho, M., Infrared Probes for Studying the Structure and Dynamics of Biomolecules. *Chem. Rev.* **2013,** *113* (8), 5817-5847.

156. Reppert, M.; Tokmakoff, A., Electrostatic frequency shifts in amide I vibrational spectra: Direct parameterization against experiment. *J. Chem. Phys.* **2013,** *138* (13), 134116.

157. Jeon, J.; Yang, S.; Choi, J.-H.; Cho, M., Computational Vibrational Spectroscopy of Peptides and Proteins in One and Two Dimensions. *Acc. Chem. Res.* **2009,** *42* (9), 1280-1289.

158. Rosenfeld, D. E.; Gengeliczki, Z.; Smith, B. J.; Stack, T. D. P.; Fayer, M. D., Structural Dynamics of a Catalytic Monolayer Probed by Ultrafast 2D IR Vibrational Echoes. *Science* **2011,** *334* (6056), 634-639.

159. Culik, R. M.; Jo, H.; DeGrado, W. F.; Gai, F., Using Thioamides To Site-Specifically Interrogate the Dynamics of Hydrogen Bond Formation in β-Sheet Folding. *J. Am. Chem. Soc.* **2012,** *134* (19), 8026-8029.

160. Tabor, D. P.; Kusaka, R.; Walsh, P. S.; Zwier, T. S.; Sibert, E. L., Local Mode Approach to OH Stretch Spectra of Benzene–(H2O)n Clusters, n = 2–7. *J. Phys. Chem. A* **2015,** *119* (38), 9917-9930.

161. Choi, J.-H.; Kwak, K.-W.; Cho, M., Computational Infrared and Two-Dimensional Infrared Photon Echo Spectroscopy of Both Wild-Type and Double Mutant Myoglobin-CO Proteins. *J. Phys. Chem. B* **2013,** *117* (49), 15462-15478.

162. Cho, M., Coherent Two-Dimensional Optical Spectroscopy. *Chem. Rev.* **2008,** *108* (4), 1331-1418.

163. Skinner, J. L.; Auer, B. M.; Lin, Y.-S., Vibrational Line Shapes, Spectral Diffusion, and Hydrogen Bonding in Liquid Water. In *Adv. Chem. Phys.*, John Wiley & Sons, Inc.: 2008; pp 59-103.

164. Paesani, F.; Xantheas, S. S.; Voth, G. A., Infrared Spectroscopy and Hydrogen-Bond Dynamics of Liquid Water from Centroid Molecular Dynamics with an Ab Initio-Based Force Field. *J. Phys. Chem. B* **2009,** *113* (39), 13118-13130.

165. Lai, Z.; Preketes, N. K.; Mukamel, S.; Wang, J., Monitoring the Folding of Trp-Cage Peptide by Two-Dimensional Infrared (2DIR) Spectroscopy. *J. Phys. Chem. B* **2013,** *117* (16), 4661-4669.

166. Lai, Z.; Preketes, N. K.; Jiang, J.; Mukamel, S.; Wang, J., Two-Dimensional Infrared (2DIR) Spectroscopy of the Peptide Beta3s Folding. *J. Phys. Chem. Lett.* **2013,** *4* (11), 1913-1917.

167. Weimann, M.; Farnik, M.; Suhm, M. A., A first glimpse at the acidic proton vibrations in HCl-water clusters via supersonic jet FTIR spectroscopy. *Phys. Chem. Chem. Phys.* **2002,** *4* (16), 3933-3937.

168. Fárník, M.; Weimann, M.; Suhm, M. A., Acidic protons before take-off: A comparative jet Fourier transform infrared study of small HCl– and HBr–solvent complexes. *J. Chem. Phys.* **2003,** *118* (22), 10120-10136.

169. Huneycutt, A. J.; Stickland, R. J.; Hellberg, F.; Saykally, R. J., Infrared cavity ringdown spectroscopy of acid–water clusters: HCl–H2O,DCl–D2O, and DCl–(D2O)2. *J. Chem. Phys.* **2003,** *118* (3), 1221-1229.

170. Ortlieb, M.; Birer, Ö.; Letzner, M.; Schwaab, G. W.; Havenith, M., Observation of Rovibrational Transitions of HCl, (HCl)2, and H2O−HCl in Liquid Helium Nanodroplets†. *J. Phys. Chem. A* **2007,** *111* (49), 12192-12199.

171. Skvortsov, D.; Lee, S. J.; Choi, M. Y.; Vilesov, A. F., Hydrated HCl Clusters, HCl(H2O)1−3, in Helium Nanodroplets: Studies of Free OH Vibrational Stretching Modes†. *J. Phys. Chem. A* **2009,** *113* (26), 7360-7365.

172. Zwier, T. S., Squeezing the Water Out of HCl(aq). *Science* **2009,** *324* (5934), 1522-1523.

173. Flynn, S. D.; Skvortsov, D.; Morrison, A. M.; Liang, T.; Choi, M. Y.; Douberly, G. E.; Vilesov, A. F., Infrared Spectra of HCl−H2O Clusters in Helium Nanodroplets. *J. Phys. Chem. Lett.* **2010,** *1* (15), 2233-2238.

174. Morrison, A. M.; Flynn, S. D.; Liang, T.; Douberly, G. E., Infrared Spectroscopy of (HCl)m(H2O)n Clusters in Helium Nanodroplets: Definitive Assignments in the HCl Stretch Region. *J. Phys. Chem. A* **2010,** *114* (31), 8090-8098.

175. Talukdar, R. K.; Burkholder, J. B.; Roberts, J. M.; Portmann, R. W.; Ravishankara, A. R., Heterogeneous Interaction of N2O5 with HCl Doped H2SO4 under Stratospheric Conditions: ClNO2 and Cl2 Yields. *J. Phys. Chem. A* **2012,** *116* (24), 6003-6014.

176. Guggemos, N.; Slavíček, P.; Kresin, V. V., Electric Dipole Moments of Nanosolvated Acid Molecules in Water Clusters. *Phys. Rev. Lett.* **2015,** *114* (4), 043401.

177. Lin, W.; Paesani, F., Infrared Spectra of HCl(H2O)n Clusters from Semiempirical Born–Oppenheimer Molecular Dynamics Simulations. *J. Phys. Chem. A* **2015,** *119* (19), 4450-4456.

178. Samanta, A. K.; Wang, Y.; Mancini, J. S.; Bowman, J. M.; Reisler, H., Energetics and Predissociation Dynamics of Small Water, HCl, and Mixed HCl–Water Clusters. *Chem. Rev.* **2016,** *116*, 4913.

179. Packer, M. J.; Clary, D. C., Interaction of HCl with water clusters: (H2O)nHCl, n = 1-3. *J. Phys. Chem.* **1995,** *99* (39), 14323-14333.

180. Lee, C.; Sosa, C.; Planas, M.; Novoa, J. J., A theoretical study of the ionic dissociation of HF, HCl, and H2S in water clusters. *J. Chem. Phys.* **1996,** *104* (18), 7081-7085.

181. Planas, M.; Lee, C.; Novoa, J. J., Kinetics of the Proton Transfer in X···(H2O)4 Clusters (X = H2O, NH3, H2S, and HCl): Evidence of a Concerted Mechanism. *J. Phys. Chem.* **1996,** *100* (41), 16495-16501.

182. Estrin, D. o. A.; Kohanoff, J.; Laria, D. H.; Weht, R. O., Hybrid quantum and classical mechanical Monte Carlo simulations of the interaction of hydrogen chloride with solid water clusters. *Chem. Phys. Lett.* **1997,** *280* (3–4), 280-286.

183. Re, S.; Osamura, Y.; Suzuki, Y.; Schaefer, H. F., Structures and stability of hydrated clusters of hydrogen chloride, HCl(H2O)n,n=1–5. *J. Chem. Phys.* **1998,** *109* (3), 973-977.

184. Bacelo, D. E.; Binning, R. C.; Ishikawa, Y., Ab Initio Monte Carlo Simulated Annealing Study of HCl(H2O)n (n = 3, 4) Clusters. *J. Phys. Chem. A* **1999,** *103* (24), 4631-4640.

185. Chaban, G. M.; Gerber, R. B.; Janda, K. C., Transition from Hydrogen Bonding to Ionization in (HCl)n(NH3)n and (HCl)n(H2O)n Clusters: Consequences for Anharmonic Vibrational Spectroscopy. *J. Phys. Chem. A* **2001,** *105* (36), 8323-8332.

186. Milet, A.; Struniewicz, C.; Moszynski, R.; Wormer, P. E. S., Theoretical study of the protolytic dissociation of HCl in water clusters. *J. Chem. Phys.* **2001,** *115* (1), 349-356.

187. Devlin, J. P.; Uras, N.; Sadlej, J.; Buch, V., Discrete stages in the solvation and ionization of hydrogen chloride adsorbed on ice particles. *Nature* **2002,** *417* (6886), 269-271.

188. Odde, S.; Mhin, B. J.; Lee, S.; Lee, H. M.; Kim, K. S., Dissociation chemistry of hydrogen halides in water. *J. Chem. Phys.* **2004,** *120* (20), 9524-9535.

189. Sillanpää, A.; Laasonen, K., Car–Parrinello Molecular Dynamics Study of DCl Hydrate Crystals. *ChemPhysChem* **2005,** *6* (9), 1879-1883.

190. la Cour Jansen, T.; Knoester, J., A transferable electrostatic map for solvation effects on amide I vibrations and its application to linear and two-dimensional spectroscopy. *J. Chem. Phys.* **2006,** *124* (4), 044502.

191. Gutberlet, A.; Schwaab, G.; Birer, Ö.; Masia, M.; Kaczmarek, A.; Forbert, H.; Havenith, M.; Marx, D., Aggregation-Induced Dissociation of HCl(H2O)4 Below 1 K: The Smallest Droplet of Acid. *Science* **2009,** *324* (5934), 1545-1548.

192. Takayanagi, T.; Takahashi, K.; Kakizaki, A.; Shiga, M.; Tachikawa, M., Path-integral molecular dynamics simulations of hydrated hydrogen chloride cluster HCl(H2O)4 on a semiempirical potential energy surface. *Chem. Phys.* **2009,** *358* (3), 196-202.

193. Sugawara, S.; Yoshikawa, T.; Takayanagi, T.; Tachikawa, M., Theoretical study on mechanisms of structural rearrangement and ionic dissociation in the HCl(H2O)4 cluster with path-integral molecular dynamics simulations. *Chem. Phys. Lett.* **2011,** *501* (4–6), 238-244.

194. Walewski, Ł.; Forbert, H.; Marx, D., Quantum Induced Bond Centering in Microsolvated HCl: Solvent Separated versus Contact Ion Pairs. *J. Phys. Chem. Lett.* **2011,** *2* (24), 3069-3074.

195. Walewski, Ł.; Forbert, H.; Marx, D., Revealing the Subtle Interplay of Thermal and Quantum Fluctuation Effects on Contact Ion Pairing in Microsolvated HCl. *ChemPhysChem* **2013,** *14* (4), 817-826.

196. Masia, M.; Forbert, H.; Marx, D., Connecting Structure to Infrared Spectra of Molecular and Autodissociated HCl−Water Aggregates†. *J. Phys. Chem. A* **2007,** *111* (49), 12181-12191.

197. Ndongmouo, U. F. T.; Lee, M. S.; Rousseau, R.; Baletto, F.; Scandolo, S., Finite-Temperature Effects on the Stability and Infrared Spectra of HCl(H2O)6 Clusters†. *J. Phys. Chem. A* **2007,** *111* (49), 12810-12815.

198. Daniel Boese, A.; Forbert, H.; Masia, M.; Tekin, A.; Marx, D.; Jansen, G., Constructing simple yet accurate potentials for describing the solvation of HCl/water clusters in bulk helium and nanodroplets. *Phys. Chem. Chem. Phys.* **2011,** *13* (32), 14550-14564.

199. Hassanali, A. A.; Cuny, J.; Ceriotti, M.; Pickard, C. J.; Parrinello, M., The Fuzzy Quantum Proton in the Hydrogen Chloride Hydrates. *J. Am. Chem. Soc.* **2012,** *134* (20), 8557-8569.

200. Lin, W.; Paesani, F., Systematic Study of Structural and Thermodynamic Properties of HCl(H₂O)[sub:n] Clusters from Semiempirical Replica Exchange Simulations. *J. Phys. Chem. A* **2013,** *117* (32), 7131-7141.

201. Mancini, J. S.; Bowman, J. M., Communication: A new ab initio potential energy surface for HCl–H2O, diffusion Monte Carlo calculations of D0 and a delocalized zero-point wavefunction. *J. Chem. Phys.* **2013,** *138* (12), 121102.

202. Mancini, J. S.; Bowman, J. M., Effects of Zero-Point Delocalization on the Vibrational Frequencies of Mixed HCl and Water Clusters. *J. Phys. Chem. Lett.* **2014,** *5* (13), 2247-2253.

203. Mancini, J. S.; Bowman, J. M., A New Many-Body Potential Energy Surface for HCl Clusters and Its Application to Anharmonic Spectroscopy and Vibration–Vibration Energy Transfer in the HCl Trimer. *J. Phys. Chem. A* **2014,** *118* (35), 7367-7374.

204. Mancini, J. S.; Samanta, A. K.; Bowman, J. M.; Reisler, H., Experiment and Theory Elucidate the Multichannel Predissociation Dynamics of the HCl Trimer: Breaking Up Is Hard To Do. *J. Phys. Chem. A* **2014,** *118* (37), 8402-8410.

205. Gao, J., Methods and Applications of Combined Quantum Mechanical and Molecular Mechanical Potentials. In *Reviews in Computational Chemistry1*, Lipkowitz, K. B.; Boyd, D. B., Eds. VCH: New York, 1995; Vol. 7, pp 119-185.

206. Dong, A.; Huang, P.; Caughey, W. S., Protein secondary structures in water from second-derivative amide I infrared spectra. *Biochemistry* **1990,** *29* (13), 3303-3308.

207. Krimm, S.; Bandekar, J., Vibrational Spectroscopy and Conformation of Peptides, Polypeptides, and Proteins. In *Adv. Protein Chem.*, C.B. Anfinsen, J. T. E.; Frederic, M. R., Eds. Academic Press: 1986; Vol. Volume 38, pp 181-364.

208. Letzner, M.; Gruen, S.; Habig, D.; Hanke, K.; Endres, T.; Nieto, P.; Schwaab, G.; Walewski, Ł.; Wollenhaupt, M.; Forbert, H.; Marx, D.; Havenith, M., High resolution spectroscopy of HCl–water clusters: IR bands of undissociated and dissociated clusters revisited. *J. Chem. Phys.* **2013,** *139* (15), 154304.

209. McNeill, V. F.; Loerting, T.; Geiger, F. M.; Trout, B. L.; Molina, M. J., Hydrogen chloride-induced surface disordering on ice. *PNAS* **2006,** *103* (25), 9422-9427.

210. Babin, V.; Leforestier, C.; Paesani, F., Development of a "First Principles" Water Potential with Flexible Monomers: Dimer Potential Energy Surface, VRT Spectrum, and Second Virial Coefficient. *J. Chem. Theory Comput.* **2013,** *9* (12), 5395-5403.

211. Babin, V.; Medders, G. R.; Paesani, F., Development of a "First Principles" Water Potential with Flexible Monomers. II: Trimer Potential Energy Surface, Third Virial Coefficient, and Small Clusters. *J. Chem. Theory Comput.* **2014,** *10* (4), 1599-1607.

212. Medders, G. R.; Babin, V.; Paesani, F., Development of a "First-Principles" Water Potential with Flexible Monomers. III. Liquid Phase Properties. *J. Chem. Theory Comput.* **2014,** *10* (8), 2906-2910.

213. Sun, X.; Wang, H.; Miller, W. H., Semiclassical theory of electronically nonadiabatic dynamics: Results of a linearized approximation to the initial value representation. *J. Chem. Phys.* **1998,** *109* (17), 7064-7074.

214. Wang, H.; Sun, X.; Miller, W. H., Semiclassical approximations for the calculation of thermal rate constants for chemical reactions in complex molecular systems. *J. Chem. Phys.* **1998,** *108* (23), 9726-9736.

215. Liu, J.; Miller, W. H., Linearized semiclassical initial value time correlation functions using the thermal Gaussian approximation: Applications to condensed phase systems. *J. Chem. Phys.* **2007,** *127* (11), 114506.

216. Cao, J.; Voth, G. A., The formulation of quantum statistical mechanics based on the Feynman path centroid density. II. Dynamical properties. *J. Chem. Phys.* **1994,** *100* (7), 5106-5117.

217. Cao, J.; Voth, G. A., The formulation of quantum statistical mechanics based on the Feynman path centroid density. III. Phase space formalism and analysis of centroid molecular dynamics. *J. Chem. Phys.* **1994,** *101* (7), 6157-6167.

218. Cao, J.; Voth, G. A., The formulation of quantum statistical mechanics based on the Feynman path centroid density. IV. Algorithms for centroid molecular dynamics. *J. Chem. Phys.* **1994,** *101* (7), 6168-6183.

219. Cao, J.; Voth, G. A., The formulation of quantum statistical mechanics based on the Feynman path centroid density. I. Equilibrium properties. *J. Chem. Phys.* **1994,** *100* (7), 5093-5105.

220. Cao, J.; Voth, G. A., The formulation of quantum statistical mechanics based on the Feynman path centroid density. V. Quantum instantaneous normal mode theory of liquids. *J. Chem. Phys.* **1994,** *101* (7), 6184-6192.

221. Rossi, M.; Liu, H.; Paesani, F.; Bowman, J.; Ceriotti, M., Communication: On the consistency of approximate quantum dynamics simulation methods for vibrational spectra in the condensed phase. *J. Chem. Phys.* **2014,** *141* (18), 181101.

222. Medders, G. R.; Paesani, F., Infrared and Raman Spectroscopy of Liquid Water through "First-Principles" Many-Body Molecular Dynamics. *J. Chem. Theory Comput.* **2015,** *11* (3), 1145-1154.

223. Craig, I. R.; Manolopoulos, D. E., Quantum statistics and classical mechanics: Real time correlation functions from ring polymer molecular dynamics. *J. Chem. Phys.* **2004,** *121* (8), 3368-3373.

224. Craig, I. R.; Manolopoulos, D. E., Chemical reaction rates from ring polymer molecular dynamics. *J. Chem. Phys.* **2005,** *122* (8), 084106.

225. Craig, I. R.; Manolopoulos, D. E., A refined ring polymer molecular dynamics theory of chemical reaction rates. *J. Chem. Phys.* **2005,** *123* (3), 034102.

226. Braams, B. J.; Manolopoulos, D. E., On the short-time limit of ring polymer molecular dynamics. *J. Chem. Phys.* **2006,** *125* (12), 124105.

227. Rossi, M.; Ceriotti, M.; Manolopoulos, D. E., How to remove the spurious resonances from ring polymer molecular dynamics. *J. Chem. Phys.* **2014,** *140* (23), 234116.

228. Mancini, J. S.; Bowman, J. M., Isolating the spectral signature of H3O+ in the smallest droplet of dissociated HCl acid. *Phys. Chem. Chem. Phys.* **2015,** *17* (9), 6222-6226.

229. Ham, S.; Kim, J.-H.; Lee, H.; Cho, M., Correlation between electronic and molecular structure distortions and vibrational properties. II. Amide I modes of NMA–nD2O complexes. *J. Chem. Phys.* **2003,** *118* (8), 3491-3498.

230. Hayashi, T.; Zhuang, W.; Mukamel, S., Electrostatic DFT Map for the Complete Vibrational Amide Band of NMA. *J. Phys. Chem. A* **2005,** *109* (43), 9747-9759.

231. Garcia-Viloca, M.; Nam, K.; Alhambra, C.; Gao, J., Solvent and Protein Effects on the Vibrational Frequency Shift and Energy Relaxation of the Azide Ligand in Carbonic Anhydrase. *J. Phys. Chem. B* **2004,** *108* (35), 13501-13512.

232. Błasiak, B.; Cho, M., Vibrational solvatochromism. II. A first-principle theory of solvation-induced vibrational frequency shift based on effective fragment potential method. *J. Chem. Phys.* **2014,** *140* (16), 164107.

233. Light, J. C.; Hamilton, I. P.; Lill, J. V., Generalized discrete variable approximation in quantum mechanics. *J. Chem. Phys.* **1985,** *82* (3), 1400-1409.

234. Colbert, D. T.; Miller, W. H., A novel discrete variable representation for quantum mechanical reactive scattering via the S-matrix Kohn method. *J. Chem. Phys.* **1992,** *96* (3), 1982.

235. Li, H.; Blinov, N.; Roy, P.-N.; Le Roy, R. J., Path-integral Monte Carlo simulation of ν3 vibrational shifts for CO2 in (He)n clusters critically tests the He–CO2 potential energy surface. *J. Chem. Phys.* **2009,** *130* (14), 144305.

236. Li, H.; Ma, Y.-T., An intramolecular vibrationally excited intermolecular potential for He–OCS: Globally tested by simulation of vibrational shifts for OCS in HeN N = 1 − 100 Clusters. *J. Chem. Phys.* **2012,** *137* (23), 234310.

237. Coxon, J. A.; Hajigeorgiou, P. G., The Radial Hamiltonians for the X1Σ+ and B1Σ+ States of HCl. *J. Mol. Spectrosc.* **2000,** *203* (1), 49-64.

238. Wang, Y.; Sosa, C. P.; Cembran, A.; Truhlar, D. G.; Gao, J., Multilevel X-Pol: A Fragment-Based Method with Mixed Quantum Mechanical Representations of Different Fragments. *J. Phys. Chem. B* **2012,** *116* (23), 6781-6788.

239. Zhao, Y.; Truhlar, D., The M06 suite of density functionals for main group thermochemistry, thermochemical kinetics, noncovalent interactions, excited states, and transition elements: two new functionals and systematic testing of four M06-class functionals and 12 other functionals. *Theor. Chem. Acc.* **2008,** *120* (1-3), 215-241.

240. Raghavachari, K.; Trucks, G. W.; Pople, J. A.; Head-Gordon, M., A fifth-order perturbation comparison of electron correlation theories. *Chem. Phys. Lett.* **1989,** *157* (6), 479-483.

241. Hättig, C.; Klopper, W.; Köhn, A.; Tew, D. P., Explicitly Correlated Electrons in Molecules. *Chem. Rev.* **2012,** *112* (1), 4-74.

242. Kong, L.; Bischoff, F. A.; Valeev, E. F., Explicitly Correlated R12/F12 Methods for Electronic Structure. *Chem. Rev.* **2012,** *112* (1), 75-107.

243. Grimme, S., Semiempirical GGA-type density functional constructed with a long-range dispersion correction. *J. Comput. Chem.* **2006,** *27* (15), 1787-1799.

244. Valiev, M.; Bylaska, E. J.; Govind, N.; Kowalski, K.; Straatsma, T. P.; Van Dam, H. J. J.; Wang, D.; Nieplocha, J.; Apra, E.; Windus, T. L.; de Jong, W. A., NWChem: A comprehensive and scalable open-source solution for large scale molecular simulations. *Comput. Phys. Commun.* **2010,** *181* (9), 1477-1489.

245. Boys, S. F.; Bernardi, F., The calculation of small molecular interactions by the differences of separate total energies. Some procedures with reduced errors. *Mol. Phys.* **1970,** *19* (4), 553-566.

246. Forbert, H.; Masia, M.; Kaczmarek-Kedziera, A.; Nair, N. N.; Marx, D., Aggregation-Induced Chemical Reactions: Acid Dissociation in Growing Water Clusters. *J. Am. Chem. Soc.* **2011,** *133* (11), 4062-4072.

247. Bader, J. S.; Berne, B. J., Quantum and classical relaxation rates from classical simulations. *J. Chem. Phys.* **1994,** *100* (11), 8359-8366.

248. Skinner, J. L.; Park, K., Calculating Vibrational Energy Relaxation Rates from Classical Molecular Dynamics Simulations: Quantum Correction Factors for Processes Involving Vibration−Vibration Energy Transfer†. *J. Phys. Chem. B* **2001,** *105* (28), 6716-6721.

249. Sagnella, D. E.; Straub, J. E.; Jackson, T. A.; Lim, M.; Anfinrud, P. A., Vibrational population relaxation of carbon monoxide in the heme pocket of photolyzed carbonmonoxy myoglobin: Comparison of time-resolved mid-IR absorbance experiments and molecular dynamics simulations. *PNAS* **1999,** *96* (25), 14324-14329.

250. Sagnella, D. E.; Straub, J. E., A Study of Vibrational Relaxation of B-State Carbon Monoxide in the Heme Pocket of Photolyzed Carboxymyoglobin. *Biophys. J.* **1999,** *77* (1), 70-84.

251. Bu, L.; Straub, J. E., Simulating Vibrational Energy Flow in Proteins: Relaxation Rate and Mechanism for Heme Cooling in Cytochrome c. *J. Phys. Chem. B* **2003,** *107* (44), 12339-12345.

252. Bu, L.; Straub, J. E., Vibrational Frequency Shifts and Relaxation Rates for a Selected Vibrational Mode in Cytochrome c. *Biophys. J.* **2003,** *85* (3), 1429-1439.

253. Gao, J.; Thompson, M. A., *Combined Quantum Mechanical and Molecular Mechanical Methods*. American Chemical Society: 1998; Vol. 712, p 324.

254. Dewar, M. J. S.; Zoebisch, E. G.; Healy, E. F.; Stewart, J. J. P., Development and use of quantum mechanical molecular models. 76. AM1: a new general purpose quantum mechanical molecular model. *J. Am. Chem. Soc.* **1985,** *107* (13), 3902-3909.

255. Haldar, T.; Bagchi, S., Electrostatic Interactions Are Key to C═O n-π* Shifts: An Experimental Proof. *J. Phys. Chem. Lett.* **2016,** *7* (12), 2270-2275.

256. Groenewold, G. S.; Gianotto, A. K.; Cossel, K. C.; Van Stipdonk, M. J.; Oomens, J.; Polfer, N.; Moore, D. T.; de Jong, W. A.; McIlwain, M. E., Mid-infrared vibrational spectra of discrete acetone-ligated cerium hydroxide cations. *Phys. Chem. Chem. Phys.* **2007,** *9* (5), 596-606.

257. Fried, S. D.; Wang, L. P.; Boxer, S. G.; Ren, P.; Pande, V. S., Calculations of the electric fields in liquid solutions. *J. Phys. Chem. B* **2013,** *117* (50), 16236-16248.

258. Fried, S. D.; Bagchi, S.; Boxer, S. G., Measuring electrostatic fields in both hydrogen-bonding and non-hydrogen-bonding environments using carbonyl vibrational probes. *J. Am. Chem. Soc.* **2013,** *135* (30), 11181-11192.

259. Fried, S. D.; Boxer, S. G., Measuring electric fields and noncovalent interactions using the vibrational stark effect. *Acc. Chem. Res.* **2015,** *48* (4), 998-1006.

260. Schneider, S. H.; Kratochvil, H. T.; Zanni, M. T.; Boxer, S. G., Solvent Independent Anharmonicity for Carbonyl Oscillators. *J. Phys. Chem. B* **2017,** *121*, 2331-2338.

261. Cho, M.; Fleming, G. R.; Saito, S.; Ohmine, I.; Stratt, R. M., Instantaneous normal mode analysis of liquid water. *The Journal of Chemical Physics* **1994,** *100* (9), 6672-6683.

262. Bowman, J. M.; Carrington, T.; Meyer, H. D., Variational quantum approaches for computing vibrational energies of polyatomic molecules. *Molecular Physics* **2008,** *106* (16-18), 2145-2182.

263. Hamilton, I. P.; Light, J. C., On distributed Gaussian bases for simple model multidimensional vibrational problems. *The Journal of Chemical Physics* **1986,** *84* (1), 306-317.

264. Garcia-Viloca, M.; Nam, K.; Alhambra, C.; Gao, J., Solvent and Protein Effects on the Vibrational Frequency Shift and Energy Relaxation of the Azide Ligand in Carbonic Anhydrase. *The Journal of Physical Chemistry B* **2004,** *108* (35), 13501-13512.

265. Colbert, D. T.; Miller, W. H., A novel discrete variable representation for quantum mechanical reactive scattering via the S-matrix Kohn method. *J. Chem. Phys.* **1992,** *96* (3), 1982-1991.

266. Echave, J. n.; Clary, D. C., Potential optimized discrete variable representation. *Chem. Phys. Lett.* **1992,** *190* (3-4), 225-230.

267. Light, J. C.; Hamilton, I. P.; Lill, J. V., Generalized discrete variable approximation in quantum mechanics. *J. Chem. Phys.* **1985,** *82* (3), 1400-1400.

268. Littlejohn, R. G.; Cargo, M.; Carrington, T.; Mitchell, K. A.; Poirier, B., A general framework for discrete variable representation basis sets. *J. Chem. Phys.* **2002,** *116* (20), 8691-8703.

269. Littlejohn, R. G.; Cargo, M., Multidimensional discrete variable representation bases: Sinc functions and group theory. *J. Chem. Phys.* **2002,** *116* (17), 7350-7361.

270. Wei, H.; Carrington, T., The discrete variable representation of a triatomic Hamiltonian in bond length–bond angle coordinates. *J. Chem. Phys.* **1992,** *97* (5), 3029-3037.

271. Xue, R.-J.; Grofe, A.; Yin, H.; Qu, Z.; Gao, J.; Li, H., Perturbation Approach for Computing Infrared Spectra of the Local Mode of Probe Molecules. *Journal of Chemical Theory and Computation* **2016,** *13* (1), 191-201.

272. Brooks, B. R.; Iii, C. L. B.; A. D. Mackerell, Jr.; Nilsson, L.; Petrella, R. J.; Roux, B.; Won, Y.; Archontis, G.; Bartels, C.; Boresch, S.; Caflisch, A.; Caves, L.; Cui, Q.; Dinner, A. R.; Feig, M.; Fischer, S.; Gao, J.; Hodoscek, M. W. I.; Karplus, M., CHARMM: The Biomolecular Simulation Program B. *Journal of computational chemistry* **2009,** *30* (10), 1545-1614.

273. Colbert, D. T.; Miller, W. H., A novel discrete variable representation for quantum mechanical reactive scattering via the S-matrix Kohn method. *Journal of Chemical Physics* **1992,** *96* (3), 1982-1991.

274. Light, J. C.; Carrington, T., Discrete-Variable Representations and their Utilization. *Advances in Chemical Physics* **2000,** *114*, 263-310.

275. Littlejohn, R. G.; Cargo, M.; Carrington, T.; Mitchell, K. A.; Poirier, B., A general framework for discrete variable representation basis sets. *Journal of Chemical Physics* **2002,** *116* (20), 8691-8703.

276. Light, J. C.; Hamilton, I. P.; Lill, J. V., Generalized discrete variable approximation in quantum mechanics. *The Journal of Chemical Physics* **1985,** *82* (3), 1400-1400.

277. Echave, J. n.; Clary, D. C., Potential optimized discrete variable representation. *Chemical Physics Letters* **1992,** *190* (3-4), 225-230.

278. Wei, H.; Carrington, T., The discrete variable representation of a triatomic Hamiltonian in bond length–bond angle coordinates. *The Journal of Chemical Physics* **1992,** *97* (5), 3029-3037.

279. Mayer, I., *Simple Theorems, Proofs, and Derivations in Quantum Chemistry*. Springer Science+Business Media, LLC: 2003.

280. Arun, K. S.; Huang, T. S.; Blostein, S. D., Least-Squares Fitting of Two 3-D Point Sets. *IEEE Trans. Pattern Anal. Mach. Intell.* **1987,** *9* (5), 698-700.

281. Stewart, J. J. P., Optimization of Parameters for Semiempirical Methods .1. Method. *J. Comput. Chem.* **1989,** *10* (2), 209-220.

282. Stewart, J. J. P., Optimization of parameters for semiempirical methods II. Applications. *J. Comput. Chem.* **1989,** *10* (2), 221-264.

283. Stewart, J. J. P., Optimization of parameters for semiempirical methods. III Extension of PM3 to Be, Mg, Zn, Ga, Ge, As, Se, Cd, In, Sn, Sb, Te, Hg, Tl, Pb, and Bi. *J. Comput. Chem.* **1991,** *12* (3), 320-341.

284. Jorgensen, W. L.; Maxwell, D. S.; Tirado-Rives, J., Development and Testing of the OLPS All-Atom Force Field on Conformational Energetics and Properties of Organic Liquids. *J. Am. Chem. Soc.* **1996,** *118* (15), 11225-11236.

285. McDonald, N. A.; Jorgensen, W. L., Development of an All-Atom Force Field for Heterocycles. Properties of Liquid Pyrrole, Furan, Diazoles, and Oxazoles. *J. Phys. Chem. B* **1998,** *102* (1-2), 8049-8059.

286. Walker, R. C.; Crowley, M. F.; Case, D. A., The implementation of a fast and accurate QM/MM potential method in Amber. *Journal of Computational Chemistry* **2008,** *29* (7), 1019-1031.

287. Olson, C. M.; Grofe, A.; Huber, C. J.; Spector, I. C.; Gao, J.; Massari, A. M., Enhanced vibrational solvatochromism and spectral diffusion by electron rich substituents on small molecule silanes. *J. Chem. Phys.* **2017,** *147* (12), 124302-124302.

288. Cho, M., *Two-Dimensional Optical Spectroscopy*. 2009; p 385-385.

289. Mukamel, S., *Principles of nonlinear optical spectroscopy*. Oxford University Press: New York; Oxford, 1999.

290. Skinner, J. L., Vibrational line shapes and spectral diffusion in fluids. *Mol. Phys.* **2007,** *106* (16-18), 2245-2253.

291. Choi, J. H.; Kwak, K. W.; Cho, M., Computational infrared and two-dimensional infrared photon echo spectroscopy of both wild-type and double mutant myoglobin-CO proteins. *J. Phys. Chem. B* **2013,** *117* (49), 15462-15478.

292. Kwac, K.; Lee, H.; Cho, M., Non-Gaussian statistics of amide I mode frequency fluctuation of N-methylacetamide in methanol solution: Linear and nonlinear vibrational spectra. *J. Chem. Phys.* **2004,** *120* (3), 1477-1490.

293. Kim, Y. S.; Hochstrasser, R. M., The 2D IR responses of amide and carbonyl modes in water cannot be described by gaussian frequency fluctuations. *J. Phys. Chem. B* **2007,** *111* (33), 9697-9701.

294. Jones, B. H.; Huber, C. J.; Massari, A. M., Solvation Dynamics of Vaska's Complex by 2D-IR Spectroscopy. *Journal of Physical Chemistry C* **2011,** *115* (50), 24813-24822.

295. Jones, B. H.; Huber, C. J.; Massari, A. M., Solvent-mediated vibrational energy relaxation from Vaska's complex adducts in binary solvent mixtures. *Journal of Physical Chemistry A* **2013,** *117* (29), 6150-6157.

296. Eckbreth, A. C., Boxcars - Crossed-Beam Phase-Matched Cars Generation in Gases. *Applied Physics Letters* **1978,** *32* (7), 421-423.

297. Spector, I. C.; Olson, C. M.; Huber, C. J.; Massari, A. M., Simple fully reflective method of scatter reduction in 2D-IR spectroscopy. *Opt. Lett.* **2015,** *40* (8), 1850-1852.

298. Khalil, M.; Demirdoven, N.; Tokmakoff, A., Coherent 2D IR spectroscopy: Molecular structure and dynamics in solution. *J. Phys. Chem. A* **2003,** *107* (27), 5258-5279.

299. Khalil, M.; Demirdoven, N.; Tokmakoff, A., Obtaining absorptive line shapes in two-dimensional infrared vibrational correlation spectra. *Physical Review Letters* **2003,** *90* (4), 047401.

300. Kwak, K.; Rosenfeld, D. E.; Fayer, M. D., Taking apart the two-dimensional infrared vibrational echo spectra: More information and elimination of distortions. *J. Chem. Phys.* **2008,** *128* (20), 204505.

301. Faeder, S. M. G.; Jonas, D. M., Two-dimensional electronic correlation and relaxation spectra: Theory and model calculations. *Journal of Physical Chemistry A* **1999,** *103* (49), 10489-10505.

302. Kwon, Y.; Lee, C.; Park, S., Effect of ion-molecule interaction on fermi-resonance in acetonitrile studied by ultrafast vibrational spectroscopy. *Chemical Physics* **2014,** *445*, 38-45.

303. Hamm, P.; Zanni, M. T., *Concepts and Methods of 2D Infrared Spectroscopy*. Cambridge University Press: Cambridge, 2011.

304. Zheng, J. R.; Kwak, K.; Asbury, J.; Chen, X.; Piletic, I. R.; Fayer, M. D., Ultrafast dynamics of solute-solvent complexation observed at thermal equilibrium in real time. *Science* **2005,** *309* (5739), 1338-1343.

305. Gaffney, K. J.; Davis, P. H.; Piletic, I. R.; Levinger, N. E.; Fayer, M. D., Hydrogen bond dissociation and reformation in methanol oligomers following hydroxyl stretch relaxation. *Journal of Physical Chemistry A* **2002,** *106* (50), 12012-12023.

306. Kwak, K. W.; Park, S.; Fayer, M. D., Dynamics around solutes and solute-solvent complexes in mixed solvents. *Proceedings of the National Academy of Sciences of the United States of America* **2007,** *104* (36), 14221-14226.

307. Reichardt, C., Solvatochromic Dyes as Solvent Polarity Indicators. *Chemical Reviews* **1994,** *94* (8), 2319-2358.

308. Fried, S. D.; Wang, L. P.; Boxer, S. G.; Ren, P.; Pande, V. S., Calculations of the electric fields in liquid solutions. *Journal of Physical Chemistry B* **2013,** *117* (50), 16236-16248.

309. Fried, S. D.; Bagchi, S.; Boxer, S. G., Measuring electrostatic fields in both hydrogen-bonding and non-hydrogen-bonding environments using carbonyl vibrational probes. *Journal of the American Chemical Society* **2013,** *135* (30), 11181-11192.

310. Schneider, S. H.; Kratochvil, H. T.; Zanni, M. T.; Boxer, S. G., Solvent-Independent Anharmonicity for Carbonyl Oscillators. *Journal of Physical Chemistry B* **2017,** *121* (10), 2331-2338.

311. Garcia, M. V.; Redondo, M. I., Influence of solvent polarity and acidity properties on the frequency of the carbonyl band of dimethylformamide, acetophenone and benzophenone. *Spectrochim. Acta Part A* **1987,** *43A* (7), 879-885.

312. Barton, A. F. M., Solubility parameters. *Chem. Rev.* **1975,** *75*, 731-753.

313. *CRC Handbook of Chemistry and Physics*. 98th Edition (Internet Version 2018) ed.; CRC Press/Taylor & Francis: Boca Raton, FL.

314. Edington, S. C.; Flanagan, J. C.; Baiz, C. R., An empirical IR frequency map for ester C=O stretching vibrations. *J. Phys. Chem. A* **2016,** *120* (22), 3888-3896.

315. Chuntonov, L.; Pazos, I. M.; Ma, J.; Gai, F., Kinetics of exchange between Zero-, One-, and two-hydrogen-bonded states of methyl and ethyl acetate in methanol. *J. Phys. Chem. B* **2015,** *119* (12), 4512-4520.

316. Pazos, I. M.; Ghosh, A.; Tucker, M. J.; Gai, F., Ester carbonyl vibration as a sensitive probe of protein local electric field. *Angew. Chem. Int. Ed.* **2014,** *53* (24), 6080-6084.

317. Arun, K. S.; Huang, T. S.; Blostein, S. D., Least-Squares Fitting of Two 3-D Point Sets. *IEEE Trans. Pattern Anal. Mach. Intell. ()* **1987,** *9* (5), 698-700.

318. Castner, E. W.; Maroncelli, M., Solvent dynamics derived from optical Kerr effect, dielectric dispersion, and time-resolved Stokes shift measurements: An empirical comparison. *J. Mol. Liq.* **1998,** *77* (1-3), 1-36.

319. Joo, T. H.; Jia, Y. W.; Yu, J. Y.; Lang, M. J.; Fleming, G. R., Third-order nonlinear time domain probes of solvation dynamics. *J. Chem. Phys.* **1996,** *104* (16), 6089-6108.

320. Kwon, O. H.; Yoo, T. H.; Othona, C. M.; Van Deventer, J. A.; Tirrell, D. A.; Zewail, A. H., Hydration dynamics at fluorinated protein surfaces. *Proc. Nat. Acad. Soc. USA* **2010,** *107* (40), 17101-17106.

321. Stratt, R. M.; Maroncelli, M., Nonreactive dynamics in solution: The emerging molecular view of solvation dynamics and vibrational relaxation. *J. Phys. Chem.* **1996,** *100* (31), 12981-12996.

322. Marcus, R. A., Electron-Transfer Reactions in Chemistry - Theory and Experiment. *Rev. Mod. Phys.* **1993,** *65* (3), 599-610.

323. Barbara, P. F.; Meyer, T. J.; Ratner, M. A., Contemporary issues in electron transfer research. *J. Phys. Chem.* **1996,** *100* (31), 13148-13168.

324. Casey, C. P.; Beetner, S. E.; Johnson, J. B., Spectroscopic determination of hydrogenation rates and intermediates during carbonyl hydrogenation catalyzed by Shvo's hydroxycyclopentadienyl diruthenium hydride agrees with kinetic modeling based on independently measured rates of elementary reactions. *J. Am. Chem. Soc.* **2008,** *130* (7), 2285-2295.

325. Chock, P. B.; Halpern, J., Kinetics of the Addition of Hydrogen, Oxygen, and Methyl Iodide to Some Square-Planar Iridium (I) Complexes1. *J. Am. Chem. Soc.* **1966,** *88* (15), 3511-3514.

326. Ugo, R.; Pasini, A.; Fusi, A.; Cenini, S., Kinetic investigation of some electronic and steric factors in oxidative addition reactions to Vaska's compound. *J. Am. Chem. Soc.* **1972,** *94* (21), 7364-7370.

327. Cainelli, G.; Galletti, P.; Giacomini, D., Solvent effects on stereoselectivity: more than just an environment. *Chem. Soc. Rev.* **2009,** *38* (4), 990-1001.

328. Gao, J. L., Hybrid quantum and molecular mechanical simulations: An alternative avenue to solvent effects in organic chemistry. *Acc. Chem. Res.* **1996,** *29* (6), 298-305.

329. Brunori, M.; Cutruzzola, F.; Savino, C.; Travaglini-Allocatelli, C.; Vallone, B.; Gibson, Q. H., Does picosecond protein dynamics have survival value? *Trends Biochem. Sci* **1999,** *24* (7), 253-255.

330. Jackson, T. A.; Lim, M.; Anfinrud, P. A., COMPLEX NONEXPONENTIAL RELAXATION IN MYOGLOBIN AFTER PHOTODISSOCIATION OF MBCO - MEASUREMENT AND ANALYSIS FROM 2-PS TO 56-MU-S. *Chem. Phys.* **1994,** *180* (2-3), 131-140.

331. Merchant, K. A.; Noid, W. G.; Akiyama, R.; Finkelstein, I. J.; Goun, A.; McClain, B. L.; Loring, R. F.; Fayer, M. D., Myoglobin-CO substate structures and dynamics: Multidimensional vibrational echoes and molecular dynamics simulations. *J. Am. Chem. Soc.* **2003,** *125* (45), 13804-13818.

332. Ostermann, A.; Waschipky, R.; Parak, F. G.; Nienhaus, G. U., Ligand binding and conformational motions in myoglobin. *Nature* **2000,** *404* (6774), 205-208.

333. Pu, J. Z.; Gao, J. L.; Truhlar, D. G., Multidimensional tunneling, recrossing, and the transmission coefficient for enzymatic reactions. *Chem. Rev.* **2006,** *106* (8), 3140-3169.

334. Karplus, M., Aspects of protein reaction dynamics: Deviations from simple behavior. *J. Phys. Chem. B* **2000,** *104* (1), 11-27.

335. Farina, V.; Krishnan, B.; Marshall, D. R.; Roth, G. P., PALLADIUM-CATALYZED COUPLING OF ARYLSTANNANES WITH ORGANIC SULFONATES - A COMPREHENSIVE STUDY. *J. Org. Chem.* **1993,** *58* (20), 5434-5444.

336. Fitzpatrick, P. A.; Klibanov, A. M., HOW CAN THE SOLVENT AFFECT ENZYME ENANTIOSELECTIVITY. *J. Am. Chem. Soc.* **1991,** *113* (8), 3166-3171.

337. Riva, R.; Schmeits, S.; Jerome, C.; Jerome, R.; Lecomte, P., Combination of ring-opening polymerization and "click chemistry": Toward functionalization and grafting of poly(epsilon-caprolactone). *Macromolecules* **2007,** *40* (4), 796-803.

338. Schutt, T. C.; Bharadwaj, V. S.; Hegde, G. A.; Johns, A. J.; Maupin, C. M., In silico insights into the solvation characteristics of the ionic liquid 1-methyltriethoxy-3-ethylimidazolium acetate for cellulosic biomass. *Phys. Chem. Chem. Phys.* **2016,** *18* (34), 23715-23726.

339. Jones, B. H.; Huber, C. J.; Spector, I. C.; Tabet, A. M.; Butler, R. L.; Hang, Y.; Massari, A. M., Correlating solvent dynamics and chemical reaction rates using binary solvent mixtures and two-dimensional infrared spectroscopy. *J. Chem. Phys.* **2015,** *142* (21), 212441.

340. Kiefer, L. M.; Kubarych, K. J., Solvent-Dependent Dynamics of a Series of Rhenium Photoactivated Catalysts Measured with Ultrafast 2DIR. *J. Phys. Chem. A* **2015,** *119* (6), 959-965.

341. Farrer, R. A.; Fourkas, J. T., Orientational dynamics of liquids confined in nanoporous sol-gel glasses studied by optical Kerr effect spectroscopy. *Acc. Chem. Res.* **2003,** *36* (8), 605-612.

342. Jaye, A. A.; Hunt, N. T.; Meech, S. R., Temperature- and solvation-dependent dynamics of liquid sulfur dioxide studied through the ultrafast optical Kerr effect. *J. Chem. Phys.* **2006,** *124* (2), 024506.

343. Shirota, H.; Fujisawa, T.; Fukazawa, H.; Nishikawa, K., Ultrafast Dynamics in Aprotic Molecular Liquids: A Femtosecond Raman-Induced Kerr Effect Spectroscopic Study. *Bull. Chem. Soc. Jpn.* **2009,** *82* (000273024400003), 1347-1366.

344. Cho, M. H.; Rosenthal, S. J.; Scherer, N. F.; Ziegler, L. D.; Fleming, G. R., ULTRAFAST SOLVENT DYNAMICS - CONNECTION BETWEEN TIME RESOLVED FLUORESCENCE AND OPTICAL KERR MEASUREMENTS. *J. Chem. Phys.* **1992,** *96* (7), 5033-5038.

345. Cichos, F.; Willert, A.; Rempel, U.; Von Borczyskowski, C., Solvation dynamics in mixtures of polar and nonpolar solvents. *J. Phys. Chem. A* **1997,** *101* (44), 8179-8185.

346. Luther, B.; Kimmel, J.; Levinger, N., Dynamics of polar solvation in acetonitrile–benzene binary mixtures: Role of dipolar and quadrupolar contributions to solvation. *J. Chem. Phys.* **2002,** *116* (8), 3370-3377.

347. Maroncelli, M., THE DYNAMICS OF SOLVATION IN POLAR LIQUIDS. *J. Mol. Liq.* **1993,** *57*, 1-37.

348. Baiz, C. R.; McRobbie, P. L.; Anna, J. M.; Geva, E.; Kubarych, K. J., Two-Dimensional Infrared Spectroscopy of Metal Carbonyls. *Acc. Chem. Res.* **2009,** *42* (9), 1395-1404.

349. Fayer, M. D., Dynamics of Liquids, Molecules, and Proteins Measured with Ultrafast 2D IR Vibrational Echo Chemical Exchange Spectroscopy. *Annu. Rev. Phys. Chem.* **2009,** *60*, 21-38.

350. Jones, B. H.; Massari, A. M., Origins of Spectral Broadening in Iodated Vaska's Complex in Binary Solvent Mixtures. *J. Phys. Chem. B* **2013,** *117* (49), 15741-15749.

351. Underwood, D. F.; Blank, D. A., Ultrafast solvation dynamics: A view from the solvent's perspective using a novel resonant-pump, nonresonant-probe technique. *J. Phys. Chem. A* **2003,** *107* (7), 956-961.

352. Hamm, P.; Lim, M. H.; Hochstrasser, R. M., Structure of the amide I band of peptides measured by femtosecond nonlinear-infrared spectroscopy. *J. Phys. Chem. B* **1998,** *102* (31), 6123-6138.

353. Finkelstein, I. J.; Goj, A.; McClain, B. L.; Massari, A. M.; Merchant, K. A.; Loring, R. F.; Fayer, M. D., Ultrafast dynamics of myoglobin without the distal histidine: Stimulated vibrational echo experiments and molecular dynamics simulations. *J. Phys. Chem. B* **2005,** *109* (35), 16959-16966.

354. Medders, G. R.; Paesani, F., Water Dynamics in Metal-Organic Frameworks: Effects of Heterogeneous Confinement Predicted by Computational Spectroscopy. *J. Phys. Chem. Lett.* **2014,** *5* (16), 2897-2902.

355. Pieniazek, P. A.; Lin, Y. S.; Chowdhary, J.; Ladanyi, B. M.; Skinner, J. L., Vibrational Spectroscopy and Dynamics of Water Confined inside Reverse Micelles. *J. Phys. Chem. B* **2009,** *113* (45), 15017-15028.

356. Rothschild, W. G., Solvation by benzene: molecular dynamics simulation of orientational motion, translational diffusion, and site-site radial distributions of the solutes di- and trichloromethane (chloroform). *Mol. Phys.* **2007,** *105* (8), 1003-1011.

357. Asbury, J. B.; Steinel, T.; Stromberg, C.; Corcelli, S. A.; Lawrence, C. P.; Skinner, J. L.; Fayer, M. D., Water dynamics: Vibrational echo correlation spectroscopy

and comparison to molecular dynamics simulations. *J. Phys. Chem. A* **2004,** *108* (7), 1107-1119.

358. Bakulin, A. A.; Liang, C.; Jansen, T. L.; Wiersma, D. A.; Bakker, H. J.; Pshenichnikov, M. S., Hydrophobic Solvation: A 2D IR Spectroscopic Inquest. *Acc. Chem. Res.* **2009,** *42* (9), 1229-1238.

359. Eaves, J. D.; Loparo, J. J.; Fecko, C. J.; Roberts, S. T.; Tokmakoff, A.; Geissler, P. L., Hydrogen bonds in liquid water are broken only fleetingly. *Proc. Nat. Acad. Soc. USA* **2005,** *102* (37), 13019-13022.

360. Ganim, Z.; Chung, H. S.; Smith, A. W.; Deflores, L. P.; Jones, K. C.; Tokmakoff, A., Amide I two-dimensional infrared Spectroscopy of proteins. *Acc. Chem. Res.* **2008,** *41* (3), 432-441.

361. Ji, M. B.; Odelius, M.; Gaffney, K. J., Large Angular Jump Mechanism Observed for Hydrogen Bond Exchange in Aqueous Perchlorate Solution. *Science* **2010,** *328* (5981), 1003-1005.

362. Woutersen, S.; Mu, Y.; Stock, G.; Hamm, P., Hydrogen-bond lifetime measured by time-resolved 2D-IR spectroscopy: N-methylacetamide in methanol. *Chem. Phys.* **2001,** *266* (2-3), 137-147.

363. Kwak, K.; Park, S.; Finkelstein, I. J.; Fayer, M. D., Frequency-frequency correlation functions and apodization in two-dimensional infrared vibrational echo spectroscopy: A new approach. *J. Chem. Phys.* **2007,** *127* (12), 124503.

364. Tan, H. S.; Piletic, I. R.; Fayer, M. D., Polarization selective spectroscopy experiments: methodology and pitfalls. *J. Opt. Soc. Am. B* **2005,** *22* (9), 2009-2017.

365. Frisch, M. J.; Trucks, G. W.; Schlegel, H. B.; Scuseria, G. E.; Robb, M. A.; Cheeseman, J. R.; Scalmani, G.; Barone, V.; Mennucci, B.; Petersson, G. A.; Nakatsuji, H.; Caricato, M.; Li, X.; Hratchian, H. P.; Izmaylov, A. F.; Bloino, J.; Zheng, G.; Sonnenberg, J. L.; Hada, M.; Ehara, M.; Toyota, K.; Fukuda, R.; Hasegawa, J.; Ishida, M.; Nakajima, T.; Honda, Y.; Kitao, O.; Nakai, H.; Vreven, T.; Montgomery Jr., J. A.; Peralta, J. E.; Ogliaro, F.; Bearpark, M. J.; Heyd, J.; Brothers, E. N.; Kudin, K. N.; Staroverov, V. N.; Kobayashi, R.; Normand, J.; Raghavachari, K.; Rendell, A. P.; Burant, J. C.; Iyengar, S. S.; Tomasi, J.; Cossi, M.; Rega, N.; Millam, N. J.; Klene, M.; Knox, J. E.; Cross, J. B.; Bakken, V.; Adamo, C.; Jaramillo, J.; Gomperts, R.; Stratmann, R. E.;

Yazyev, O.; Austin, A. J.; Cammi, R.; Pomelli, C.; Ochterski, J. W.; Martin, R. L.; Morokuma, K.; Zakrzewski, V. G.; Voth, G. A.; Salvador, P.; Dannenberg, J. J.; Dapprich, S.; Daniels, A. D.; Farkas, Ö.; Foresman, J. B.; Ortiz, J. V.; Cioslowski, J.; Fox, D. J. *Gaussian 09 Revision D.01*, Gaussian, Inc.: Wallingford, CT, USA, 2009.

366. Brooks, B. R.; Brooks, C. L.; Mackerell, A. D.; Nilsson, L.; Petrella, R. J.; Roux, B.; Won, Y.; Archontis, G.; Bartels, C.; Boresch, S.; Caflisch, A.; Caves, L.; Cui, Q.; Dinner, A. R.; Feig, M.; Fischer, S.; Gao, J.; Hodoscek, M.; Im, W.; Kuczera, K.; Lazaridis, T.; Ma, J.; Ovchinnikov, V.; Paci, E.; Pastor, R. W.; Post, C. B.; Pu, J. Z.; Schaefer, M.; Tidor, B.; Venable, R. M.; Woodcock, H. L.; Wu, X.; Yang, W.; York, D. M.; Karplus, M., CHARMM: The Biomolecular Simulation Program. *J. Comput. Chem.* **2009,** *30* (10), 1545-1614.

367. Brooks, B. R.; Bruccoleri, R. E.; Olafson, B. D.; States, D. J.; Swaminathan, S.; Karplus, M., CHARMM - A PROGRAM FOR MACROMOLECULAR ENERGY, MINIMIZATION, AND DYNAMICS CALCULATIONS. *J. Comput. Chem.* **1983,** *4* (2), 187-217.

368. Xue, R. J.; Grofe, A.; Yin, H.; Qu, Z. X.; Gao, J. L.; Li, H., Perturbation Approach for Computing Infrared Spectra of the Local Mode of Probe Molecules. *J. Chem. Theory Comput.* **2017,** *13* (1), 191-201.

369. Colbert, D. T.; Miller, W. H., A NOVEL DISCRETE VARIABLE REPRESENTATION FOR QUANTUM-MECHANICAL REACTIVE SCATTERING VIA THE S-MATRIX KOHN METHOD. *J. Chem. Phys.* **1992,** *96* (3), 1982-1991.

370. Echave, J.; Clary, D. C., POTENTIAL OPTIMIZED DISCRETE VARIABLE REPRESENTATION. *Chem. Phys. Lett.* **1992,** *190* (3-4), 225-230.

371. Light, J. C.; Hamilton, I. P.; Lill, J. V., GENERALIZED DISCRETE VARIABLE APPROXIMATION IN QUANTUM-MECHANICS. *J. Chem. Phys.* **1985,** *82* (3), 1400-1409.

372. Kwac, K.; Lee, H.; Cho, M. H., Non-Gaussian statistics of amide I mode frequency fluctuation of N-methylacetamide in methanol solution: Linear and nonlinear vibrational spectra. *J. Chem. Phys.* **2004,** *120* (3), 1477-1490.

373. Gowers, R. J.; Carbone, P., A multiscale approach to model hydrogen bonding: The case of polyamide. *J. Chem. Phys.* **2015,** *142* (22), 224907.

374. Rapaport, D. C., HYDROGEN-BONDS IN WATER NETWORK ORGANIZATION AND LIFETIMES. *Mol. Phys.* **1983,** *50* (5), 1151-1162.

375. Michaud-Agrawal, N.; Denning, E. J.; Woolf, T. B.; Beckstein, O., Software News and Updates MDAnalysis: A Toolkit for the Analysis of Molecular Dynamics Simulations. *J. Comput. Chem.* **2011,** *32* (10), 2319-2327.

376. Marenich, A. V.; Cramer, C. J.; Truhlar, D. G., Universal Solvation Model Based on Solute Electron Density and on a Continuum Model of the Solvent Defined by the Bulk Dielectric Constant and Atomic Surface Tensions. *J. Phys. Chem. B* **2009,** *113* (18), 6378-6396.

377. Mennucci, B., Polarizable continuum model. *Wiley Interdisciplinary Reviews: Computational Molecular Science* **2012,** *2* (3), 386-404.

378. Batuev, M. I.; Petrov, A. D.; Ponomarenko, V. A.; Matveeva, A. D., Optical investigation of the Si-H bond and peculiarities in its chemical behavior in various compounds. *Bull. Acad. Sci. USSR* **1956,** *5* (10), 1269-1274.

379. Lucovsky, G., Chemical effects on the frequencies of Si-H vibrations in amorphous solids. *Solid State Commun.* **1979,** *29* (8), 571-576.

380. Lucovsky, G.; Nemanich, R. J.; Knights, J. C., Structural interpretation of the vibrational spectra of a-Si: H alloys. *Phys. Rev. B* **1979,** *19* (4), 2064-2073.

381. Smith, A. L.; Angelotti, N. C., Correlation of the SiH stretching frequency with molecular structure. *Spectrochim. Acta* **1959,** *15*, 412-420.

382. Thompson, H. W., Si-H vibration frequency and inductive effects. *Spectrochim. Acta* **1960,** *16* (1-2), 238-241.

383. Huber, C. J.; Massari, A. M., Characterizing Solvent Dynamics in Nanoscopic Silica Sol-Gel Glass Pores by 2D-IR Spectroscopy of an Intrinsic Vibrational Probe. *J. Phys. Chem. C* **2014,** *118* (44), 25567-25578.

384. Huber, C. J.; Anglin, T. C.; Jones, B. H.; Muthu, N.; Cramer, C. J.; Massari, A. M., Vibrational Solvatochromism in Vaska's Complex Adducts. *J. Phys. Chem. A* **2012,** *116* (37), 9279-9286.

385. Beale, T. M.; Chudzinski, M. G.; Sarwar, M. G.; Taylor, M. S., Halogen bonding in solution: thermodynamics and applications. *Chem. Soc. Rev.* **2013,** *42* (4), 1667-1680.

386. Politzer, P.; Murray, J. S.; Clark, T., Halogen bonding and other sigma-hole interactions: a perspective. *Phys. Chem. Chem. Phys.* **2013,** *15* (27), 11178-11189.

387. Kolano, C.; Helbing, J.; Kozinski, M.; Sander, W.; Hamm, P., Watching hydrogen-bond dynamics in a beta-turn by transient two-dimensional infrared spectroscopy. *Nature* **2006,** *444* (7118), 469-472.

388. Huber, C. J.; Egger, S. M.; Spector, I. C.; Juelfs, A. R.; Haynes, C. L.; Massari, A. M., 2D-IR Spectroscopy of Porous Silica Nanoparticles: Measuring the Distance Sensitivity of Spectral Diffusion. *J. Phys. Chem. C* **2015,** *119* (45), 25135-25144.

389. Chuntonov, L.; Pazos, I. M.; Ma, J. Q.; Gai, F., Kinetics of Exchange between Zero-, One-, and Two-Hydrogen-Bonded States of Methyl and Ethyl Acetate in Methanol. *J. Phys. Chem. B* **2015,** *119* (12), 4512-4520.

390. Laenen, R.; Gale, G. M.; Lascoux, N., IR spectroscopy of hydrogen-bonded methanol: Vibrational and structural relaxation on the femtosecond time scale. *J. Phys. Chem. A* **1999,** *103* (50), 10708-10712.

391. Moilanen, D. E.; Wong, D.; Rosenfeld, D. E.; Fenn, E. E.; Fayer, M. D., Ion-water hydrogen-bond switching observed with 2D IR vibrational echo chemical exchange spectroscopy. *Proc. Nat. Acad. Soc. USA* **2009,** *106* (2), 375-380.

392. Park, S.; Odelius, M.; Gaffney, K. J., Ultrafast Dynamics of Hydrogen Bond Exchange in Aqueous Ionic Solutions. *J. Phys. Chem. B* **2009,** *113* (22), 7825-7835.

393. Ryckaert, J.-P.; Ciccotti, G.; Berendsen, H. J. C., Numerical integration of the cartesian equations of motion of a system with constraints: molecular dynamics of n-alkanes. *Journal of Computational Physics* **1977,** *23* (3), 327-341.

394. Fung, B. M.; McGaughy, T. W., MOLECULAR MOTIONS IN LIQUID .1. ROTATION OF WATER AND SMALL ALCOHOLS STUDIED BY DEUTERON RELAXATION. *J. Chem. Phys.* **1976,** *65* (8), 2970-2976.

395. Lin, K.; Hu, N. Y.; Zhou, X. G.; Liu, S. L.; Luo, Y., Reorientation dynamics in liquid alcohols from Raman spectroscopy. *Journal of Raman Spectroscopy* **2012,** *43* (1), 82-88.

396. Mashimo, S.; Kuwabara, S.; Higasi, K., THE DIELECTRIC-RELAXATION OF MIXTURES OF WATER AND PRIMARY ALCOHOL. *J. Chem. Phys.* **1989,** *90* (6), 3292-3294.

397. Barthel, J.; Bachhuber, K.; Buchner, R.; Hetzenauer, H., Dielectric Spectra Of Some Common Solvents In The Microwave Region - Water And Lower Alcohols. *Chem. Phys. Lett.* **1990,** *165* (4), 369-373.